Synthesis of Ce(III) and Eu(III) Doped YAG ($Y_3Al_5O_{12}$) and ZnO Ceramics

by

Refik Ergün

A Thesis Submitted to the Graduate School of Science and Engineering
in Partial Fulfillment of the Requirements for the Degree of

Master of Science
in
Material Science and Engineering

KOC UNIVERSITY
January 2014

Koc University

Graduate School of Sciences and Engineering

This is to certify that I have examined this copy of a master's thesis by

Refik Ergün

and have found that it is complete and satisfactory in all respects,

and that any and all revisions required by the final

examining committee have been made.

Committee Members:

Uğur Ünal, Ph. D. (Advisor)

Funda Yağcı Acar, Ph. D.

Kaan Güven, Ph. D.

Date:

Abstract

This thesis consists of two parts. The first part of the thesis is dedicated to synthesis of Yttrium aluminum garnet (YAG) transparent ceramics and the second part is dedicated to the Cerium doped ZnO and $Zn(OH)_2$ layered nanocomposites.

Yttrium aluminum garnet ($Y_3Al_5O_{12}$) has very good optical properties and chemical stability. When doped with rare earth ions, YAG is an excellent material for solid-state laser and phosphorus applications. In conventional solid-state laser applications glass or Czochralski grown single crystals are used as the gain medium. Though Czochralski grown single crystals are better than the glasses in terms of optical properties, the process of single crystal growth is time consuming and expensive. Polycrystalline YAG ceramics are alternatives to the single crystal grown materials and promising candidates for solid-state laser hosts. However, even twenty years after they were first reported as an efficient laser host, polycrystalline YAG ceramics are limited in laser applications.

In recent years, ZnO materials have been in the center of interest because of their large band gap and large value of exciton binding energy. More importantly optical and electronic properties of ZnO materials can be changed by changing the morphology. Many different morphologies are well known for ZnO including, wires, tubes, rods, flowers, sheets, stars, belts. One such morphology is layered structure which forms with the aid of anionic surfactants. Layered metal hydroxides have structure based on naturally occurring material brucite ($Mg(OH)_2$).

In the first part of the thesis (Chapter I and II), various synthesis methods were used to produce Ce^{3+} and Eu^{3+} doped polycrystalline YAG samples to investigate their effect on powder characteristics. 1, 5 and 10% doped samples were prepared by hydrothermal, citrate, solid-state and co-precipitation methods. Both normal-strike and reverse-strike routes of co-precipitation method were conducted. TGA/DTA analysis showed that the samples were crystallized after 900˚C. Therefore, produced samples were calcined at different temperatures ranging from 900˚C to 1300˚C. XRD patterns of the samples showed that pure YAG phase was able to be achieved via reverse-strike route and citrate method at 900˚C while it was not possible with other methods at 900˚C. Intermediate phases YAM and YAP were not observed in reverse-strike or citrate methods. Also the effects of single and multiple step calcinations were investigated. YAG precursors were calcined at 900˚C and 1200˚C for several times. FESEM images showed that calcination temperature had little effect on grain growth on amorphous samples as long as the temperature is higher than the crystallization threshold. However, temperature increase enhanced the grain growth when samples were crystallized by a pre-calcination step. Pure YAG powders were doped with 0.28 wt% SiO_2 and slip casted for shaping. After 8h of sintering at 1750˚C under 10^{-5} Torr vacuum, 50% transparency in the visible region was achieved.

In the second part of the thesis (CHAPTER III), SDS intercalated $Zn(OH)_2$ layered materials synthesized by hydrothermal method using HMT at 90˚C. Different HMT amounts were tried ranging between 0.002 mol and 0.012 mol per 0.002 mol starting salt, $Zn(NO_3)_3$. Samples without SDS were also produced to investigate the effects of the surfactant. The samples contained 1, 5 and 10% Ce^{3+} ion. FESEM results showed that samples were formed into nanosheet morphology with the addition of SDS. With the increasing reaction time sheets rolled up into a conic morphology. Samples contained no SDS yielded hexagonal rod-like morphology which is well documented in the literature. XRD results showed that samples can be crystallized into ZnO at 90˚C without the addition of SDS. However, this was not possible with the samples with SDS as all intercalated samples were in hydroxide form. With the increasing HMT amount the samples showed a significant particle growth.

Özet

Bu tez iki kısımdan oluşmaktadır. İlk kısımda Yttrium aluminyum garnet (YAG) saydam seramikleri ikinci kısamda ise seryum katkılı ZnO ve $Zn(OH)_2$ katmanlı malzemeler incelenmiştir.

Yttrium aluminum garnet ($Y_3Al_5O_{12}$) üstün optik özelliklere yüksek kimyasal dayanıma sahiptir. Lantanit serisi iyonlarıyla katkılandığında YAG, katı hal lazerleri ve fosfor uygulamaları için üstün bir malzemedir. Günümüzde katı hal lazerlerinde, lazer kaynağı olarak cam ya da Czochralski yöntemiyle tek kristalden büyütülmüş kaynaklar kullanılmaktadır. Tek kristalden büyütme yöntemi cam lazer kaynaklarına göre bir takım avantajlar içerse de, bu yöntem pahalı ve uzun zaman gerektirmektedir. Çok kristalli YAG seramikleri tek kristalden büyütülmüş lazer kaynaklarına birer alternatiftirler ve katı hal lazer kaynakları için önemli birer adaydırlar. Ancak literatürde ilk defa lazer kaynağı olarak kullanımlarının bildirilmesinin üzerinden yirmi yıl geçmesine rağmen, günümüzde çok kristalli seramik lazer uygulamaları sınırlı kalmaktadır.

Yakın geçmişte ZnO malzemeler geniş bant aralıkları ve yüksek uyarım binding enerjileri nedeniyle büyük ilgi görmüştür. Ayrıca bu malzemelerin elektronik ve optik özellikleri morfolojiyi değiştirmek suretiyle değiştirilebilmektedir. Literatürde bahsedilen birçok morfoloji vardır. Bunlardan bazıları nano teller, tüpler, çubuklar, tabakalar, yıldızlar ve kemerlerdir. Bir diğer morfoloji olan katmanlı yapı anyonik surfactant kullanılarak oluşturulmaktadır. Katmanlı ZnO malzemeler doğal olarak da bulunan brucite ($Mg(OH)_2$) yapısındadır.

Bu çalışmanın ilk kısmında (Chapter I ve II), Ce^{3+} ve Eu^{3+} katkılı çok kristalli YAG örnekleri farklı toz sentezleme yöntemleri kullanılarak hazırlanmış ve bu yöntemlerin toz karakteristikleri üzerine olan etkileri araştırılmıştır. 1, 5 ve 10% katkılı örnekler hidrotermal, sitrat, katı hal ve çöktürme yöntemleriyle sentezlenmiştir. Çöktürme yöntemi hem normal-strike hem de reverse-strike yolları izlenilerek denenmiştir. TGA/DTA analizleri sitrat ve çöktürme yöntemleriyle hazırlanan örneklerin 900˚C'de kristallenmeye başladıklarını göstermiştir. Bu sebeple örnekler 900˚C ila 1300˚C arasında kalsine edildiler. XRD sonuçlarından, reverse-strike ve sitrat yöntemleriyle 900˚C'de saf YAG fazı elde edilebildiği görülmüş ancak aynı sonuçlar diğer yöntemlerle 900˚C'de tekrarlanamamıştır. YAM ve YAP ara fazları sitrat ve reverse-strike yöntemlerinde gözlemlenmemiştir. Ayrıca birden çok adımda kalsinasyon işleminin etkileri araştırılmıştır. YAG prekürsörleri 900˚C ve 1200˚C de bir, iki ve üç kere kalsine edilmiştir. Örneklerin FESEM fotoğrafları alınmış ve sıcaklık kristallenme eşik değerinin üzerinde olmak şartıyla, kalsinasyon sıcaklığının amorf örneklerin tane büyümeleri üzerine çok fazla etki etmediği görülmüştür. Ancak ön kalsinasyon işlemiyle kristallenmiş örneklerin taneleri ikinci bir kalsinasyonla kayda değer bir büyüme göstermiştir. 0.28% SiO_2 katkılı saf YAG tozları alçı kalıba döküm yöntemiyle şekillendirilmiştir. 1750˚C'de ve 10^{-5} Torr vakum altunda 8 saat sinterlenme işleminin ardından görünür bölgede 50% saydamlığa ulaşılmıştır.

İkinci kısımda (Chapter III), arasına SDS sokulmuş $Zn(OH)_2$ katmanlı malzemeler hidrotermal yöntem kullanılarak 90˚C'de sentezlenmiştir. 0.002 mol $Zn(NO_3)_3$ başlangıç malzemesi için 0.002 mol ile 0.012 mol arasında farklı HMT oranları denenmiştir. SDS'siz örnekler ayrıca hazırlanarak surfactantın etkisi incelenmiştir. Örneklere 1, 5 ve 10% oranlarında Ce^{3+} iyonu eklenmiştir. FESEM sonuçları örneklerin SDS'le birlikte sentezlendiklerinde nano tabaka yapısında olduklarını göstermiştir. Reaksiyon süresi arttığı durumlarda tabakalar kıvrılarak koni yapısına geçmiş ve morfoloji değişmiştir. SDS içermeyen örnekler ise literatürde de bahsedilen hegzagonal çubuk yapısı oluşturmuşlardır. XRD sonuçları, örnekler SDS kullanılmadan 90˚C'de sentezlendiğinde ZnO ürünü elde edildiğini ancak SDS kullanılmadığında bu sonucun mümkün olmadığını göstermiştir. SDS kullanılan örnekler ise bu sıcaklıkta $Zn(OH)_2$ katmanlı yapıda bulunmaktadırlar. Ayrıca HMT miktarının partikül büyümesini arttırdığı görülmüştür.

Acknowledgements

First and foremost, I am extremely grateful to my thesis advisor, Dr. Uğur Ünal for his continuous support and help since the very beginning of my work at Koç University. I have learned so many valuable things from him. He has taught me not only how to do research but also how to give your best effort in everything you do. I will be always indebted to him for his time and patience.

This study was a collaborative effort of Advance Ceramics Research Group and Laser Research Group. I cannot thank enough to Dr. Alphan Sennaroğlu, the head of the Laser Research Group, for providing us the insight of this research topic and contributing with his extensive knowledge about solid-state lasers.

I would like to thank my thesis committee members, Dr. Funda Yağcı Acar for her support during my M.Sc. interview and Dr. Kaan Güven for accepting to be in my thesis committee. I deeply appreciate their useful comments and contributions to my thesis.

I owe my gratitude to my research group member, Ceren Yılmaz. Ceren contributed my work in so many ways, she thought me and helped me in both experimental and theory. I also thank my group member, Feriha Eylül Saraç for her assistance, friendship, encouragement and her help in FTIR measurements.

I would like to thank to KUYTAM (Koc University Surface Science and Technology Center) for providing the instrumental support and infrastructure for this study and I am grateful its staff, Barış Yağcı and Cansu Yıldırım since they helped me to perform many analyses including XRD, SEM, XRF, UV-vis spectrometer and contributed to my work with their technical expertise.

This study was funded by TUBİTAK, project No. 110T810. I would like to thank them for their financial aid which provided many of our vital technical equipments.

I would like to thank my family for their support during my whole life. None of this would have been possible if it hadn’t been for them. Lastly I won’t forget Özlem Çevik’s help and morale support throughout my thesis. Thank you.

Table of Contents

TABLE of FIGURES

TABLES

CHAPTER 1 Introduction

1.1 Single Crystal and Ceramic Lasers

Solid-state lasers have a wide variety of use in many fields such as metal processing, medical applications, red-green-blue (RGB) light sources in laser printers and projectors, environmental instrumentation measurements, and optical transmission systems [1]. The first solid-state lasers had gain mediums in single crystalline or amorphous forms. In 1960 Maiman operated a solid-state flash lamp-pumped synthetic ruby crystal to produce a red laser light [2]. With the creation of a successful continuous wave laser oscillation via Nd:YAG single crystal in 1964 [3] single crystal solid state lasers became popular.

Single crystals grown from melt with the Czochralski method offer high optical quality (< 0.01 mm^{-1} optical loss) but require long processing times and high temperatures [4]. In the Czorchralski method, grown crystals have structural defects such as dislocations, striations, internal facets, and stress induced birefringence due to the thermally induced stresses during growth and cool down. Those defects will harm the optical properties [5]. The Czorchalski method can allow 40 % of its product to be used as laser source [4]. Therefore, a new approach to eliminate the difficulties of the conventional single crystal laser was required.

In 1964, the first ceramic laser gain medium experiment was performed with Dy:CaF_2 in cryogenic conditions [6]. So far, poly-crystalline ceramic lasers have not been as efficient as that of commercially produced high quality single-crystal lasers due to higher scattering losses [7]. Recently however, ceramic laser technology has proven to be a promising candidate to replace conventional single-crystal lasers with their various advantages.

Ceramics can be produced in more complex shapes and in larger volumes. Therefore ceramics make suitable laser materials to be used for a high power laser generation and for composite or fibre laser media where single-crystals would hard to fabricate. In addition, ceramics provide more homogeneous matrix for laser active ions to be doped. Besides, ceramic-derived single crystal laser can be directly synthesized through sintering. This type of single crystal lasers is promising for high power density lasers [1].

Both in transparent Ceramics and single crystals, structural defects are the main factors which limit transparency. Czorchralski grown crystals may develop thermally induced stress related defects [5]. However, ceramic laser materials tend to develop different defects. The most common defects are grain boundaries, residual pores, secondary phases, grain to grain birefringence and surface scattering [1]. Figure 1.1 shows the six most common light scattering centers in a ceramic microstructure. Despite the presence of various different defects in the ceramic body, porosity is the most harmful to transparency. Compared to that effect, scattering from grain boundaries are negligible [8-11]. An Al_2O_3 model shows that even 0.1% residual porosity can completely deteriorate the transparency [8]. Akio Ikesue and Kunio Yoshida revealed that when the pore volume becomes lower than 150 vol ppm, the optical scattering loss and the laser performance of Nd:YAG ceramics are nearly equivalent to those of Nd:YAG by the Czorchralski method. They also stated that the optical scattering in Nd:YAG ceramics is caused almost solely by pores [12, 13].

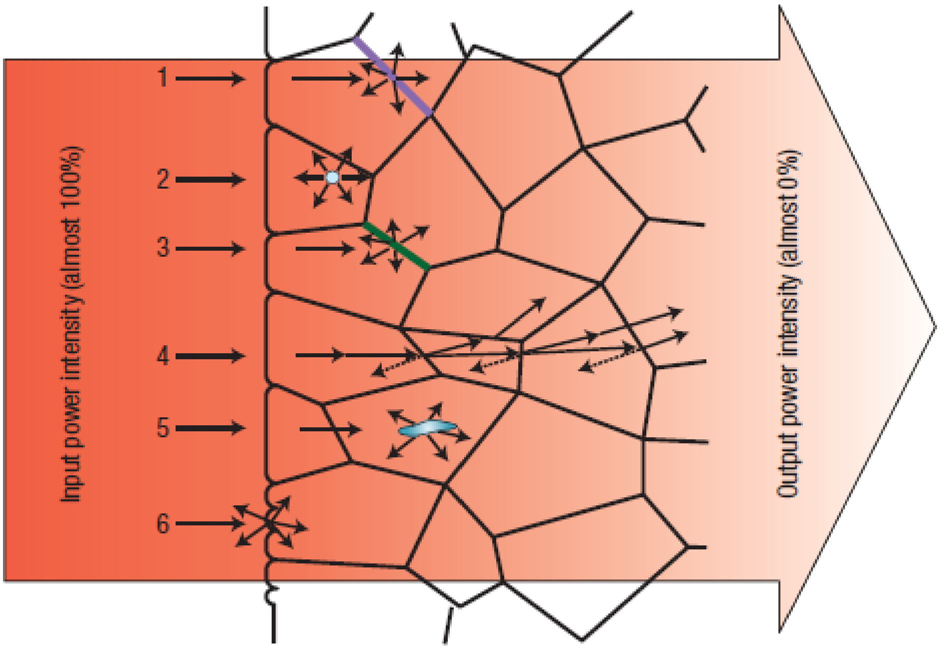

Figure 1.1 Representation of a ceramic microstructure [14]. Figure shows the six different light scattering points in an conventional transparent ceramic body due to (1) grain boundary, (2) residual porosity, (3) secondary phase, (4) double refraction, (5) inclusion and (6) surface roughness.

Optically anisotropic materials cause optical birefringence as light crosses through the grain boundary into another grain. This phenomenon results in refraction and scattering from grain boundaries. Having the average grain size less than 10%-50% of the operation wavelength, birefringence can be inhibited [8]. However, as the most of the optically transparent ceramics, YAG ceramics are also optically isotropic; therefore grain boundaries have little effect on scattering [15].

Grain boundaries may also affect transparency depending on their thickness. Clean grain boundaries have no effect on transparency in YAG ceramics [1, 16]. However impurities tend to segregate on grain boundaries and scatter the light. Ikesue and Aung reported that transparent ceramics cooled lower than 10˚C/min have secondary phases at grain boundaries [4]. Al_2O_3 and Y_2O_3 phases slightly affect the transmittance of YAG transparent ceramics, and the lower the difference between the refractive indexes of host and the grain-boundary phase is, the higher the transmittance becomes [16].

1.2 YAG Ceramics and Ce:YAG, Eu:YAG

Yttrium aluminium garnet (YAG, $Y_3Al_5O_{12}$) is a synthetic crystalline garnet material. It is also one of the three phases of the Y_2O_3-Al_2O_3 system. Phase diagram of Y_2O_3-Al_2O_3 system is shown in figure 1.2. Garnet phase has a line region however small amounths of excess Y^{3+} and Al^{3+} do not cause a secondary phase. Therefore, it is possible to have pure YAG phase in non-stoichiometric compositions. Patel *et al.* showed that non-stoichiometry is balanced by anti-site defects (Y_{Al} or Al_Y) [17]. Although this anti-site defects yields pure YAG phase, they may have additional effects on optical properties. It is important to eliminate all secondary phases in order to achieve optical transparency. Considering the narrow garnet region, stoichiometry is an important factor in transparency. Other ternary phases are YAP (Yttrium aluminum perovskite) and YAM (Yttrium aluminum monoclinic). YAG is mostly used as a host material in various solid state lasers. Common doping agents are rare earths as active laser ions. The crystal structure of YAG is given in Figure 1.3 and is cubic structure with 160 atoms per unit cell. As a general garnet structure ($A_3B'_2B''_3O_{12}$), YAG contains eight formula units. Interconnected octahedrons, tetrahedrons and dodecahedrons with shared O atoms at the corners, form the garnet structure. A, B' and B" are metal ions occupying different symmetry sites. YAG has a bcc structure with Ia3*d* or O_h^{10} space groups. Yttrium atoms (A) occupy the 24(*c*) sites and each are dodecahedral coordinated to eight oxygen atoms. Oxygen atoms occupy the 96 (*h*) sites. Al atoms (*B'*), occupy both the 16 (*a*) site with an octahedral point symmetry (C_{3i}) and (*B''* atoms) the 24(*d)* sites with tetrahedral point symmetry (S_4). Lattice constant of YAG unit cell is 1.2001 nm [18].

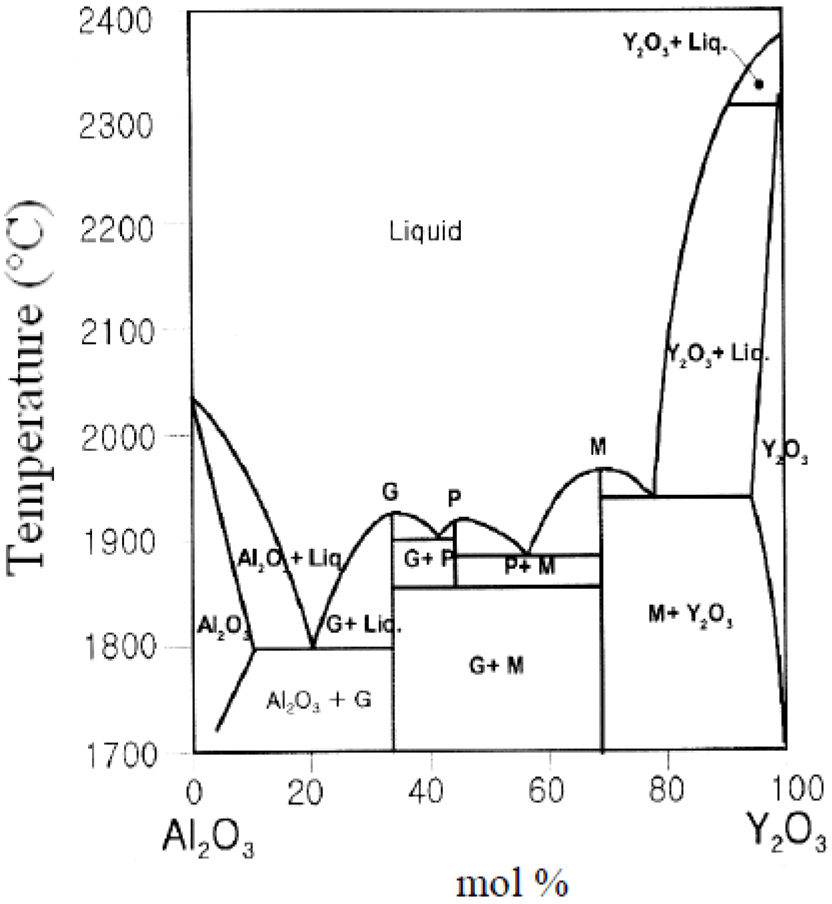

Figure 1.2 Y_2O_3-Al_2O_3 System Phase Diagram [19]. (G=YAG, P=YAP, M=YAM)

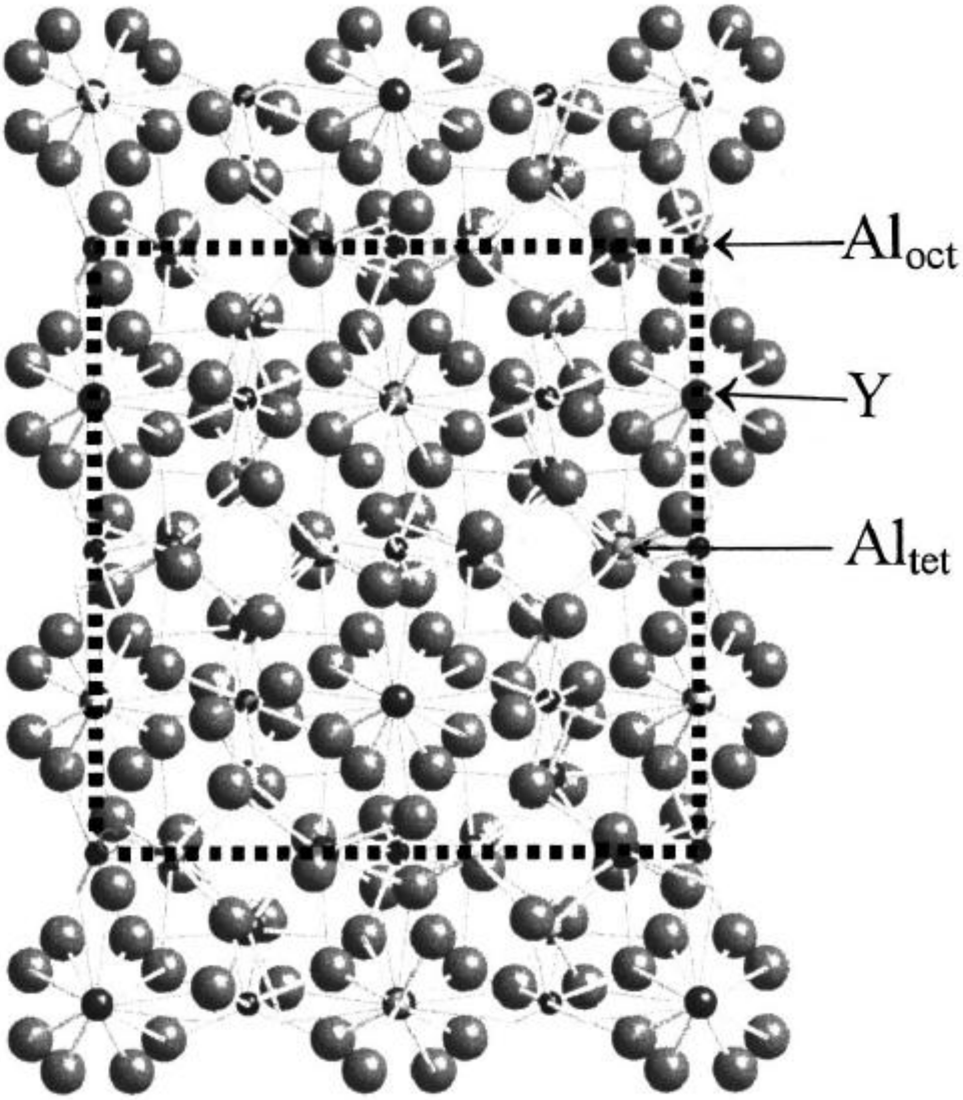

Figure 1.3 Crystal structure of YAG along the [001] direction. The dotted lines represents cubic cell boundaries [18].

In figure 1.4 physical properties of YAG is given [20-22]. YAG have many desirable properties for being a laser host; therefore, it is one of the most useful laser hosts. YAG crystals are stable, optically isotropic, and have good mechanic properties and good thermal conductivities, which permits laser operation at high average power levels. The cubic structure of YAG favors a narrow fluorescent linewidth, which offers low threshold and high gain. In addition the host YAG crystal has a wide range of suitable dopant atoms. The dodecahedrally coordinated 24(*c*) site can hold the transition metals and/or the rare earth (lanthanide) and/or actinide ions (e.g. Nd^{3+}, Ho^{3+}, Tm^{3+}, Dy^{2+}, etc.). YAG usually doped by trivalent atoms. Most common dopant atom, Nd^{3+}, occupies the 24(*c*) sites where Y^{3+} atoms would occupy. Due to the same charge of the two atoms, there is no charge difference to compensate.

Because of its optical anisotropy the refractive index does not change with the orientation of the crystallographic structure. Therefore grain boundaries will not scatter the light transmitted through them as long as there is no secondary phases are in the ceramic body. Grain size is also independent from optical transmittance because of the anisotropy. Both nano-grained or coarse-grained YAG samples can achieve 100% theoretical transparency.

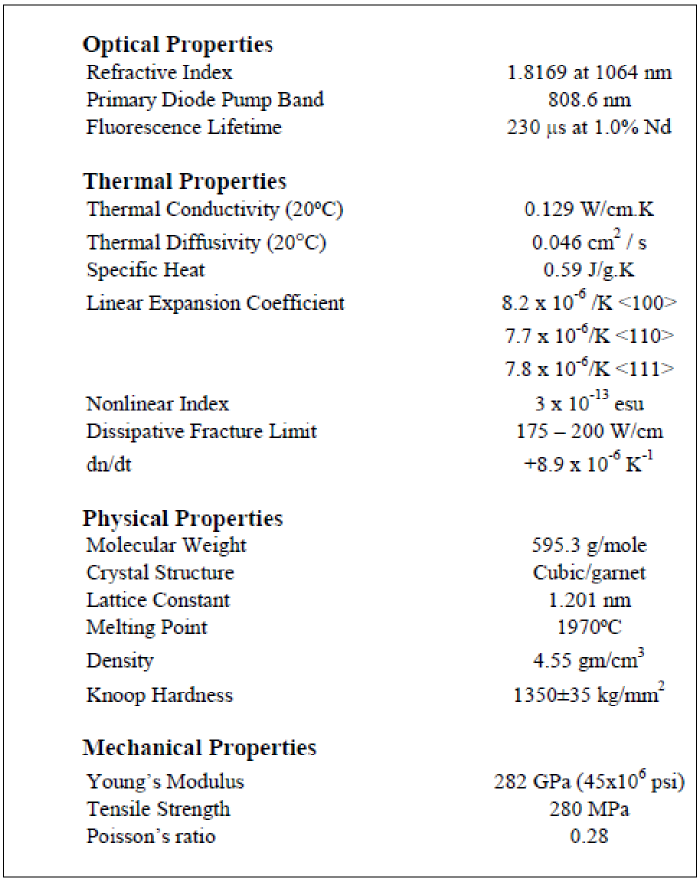

Optical Properties	
Refractive Index	1.8169 at 1064 nm
Primary Diode Pump Band	808.6 nm
Fluorescence Lifetime	230 μs at 1.0% Nd
Thermal Properties	
Thermal Conductivity (20°C)	0.129 W/cm.K
Thermal Diffusivity (20°C)	0.046 cm^2 / s
Specific Heat	0.59 J/g.K
Linear Expansion Coefficient	8.2 x 10^{-6} /K <100> 7.7 x 10^{-6}/K <110> 7.8 x 10^{-6}/K <111>
Nonlinear Index	3 x 10^{-13} esu
Dissipative Fracture Limit	175 – 200 W/cm
dn/dt	+8.9 x 10^{-6} K^{-1}
Physical Properties	
Molecular Weight	595.3 g/mole
Crystal Structure	Cubic/garnet
Lattice Constant	1.201 nm
Melting Point	1970°C
Density	4.55 gm/cm^3
Knoop Hardness	1350±35 kg/mm^2
Mechanical Properties	
Young's Modulus	282 GPa (45x10^6 psi)
Tensile Strength	280 MPa
Poisson's ratio	0.28

Figure 1.4 Selected physical properties of YAG [20-22].

1.3 Purpose of the Study

Main aim of this thesis is the synthesis of Ce(III) and Eu(III) doped polycrystalline YAG systems for optical operations, such as laser and LED applications. Many synthesis methods that are common in Nd:YAG production were applied to the Ce:YAG and Eu:YAG systems in order to validate their use in such systems. In this study we mainly investigated the formation of the crystalline structure and influence of the synthesis conditions.

1.4 Yag Powder Synthesis Mechanisms

1.4.1 Co-precipitation

Co-precipitation is a fine powder synthesis method for advanced ceramic production. Co-precipitation has two main steps: nucleation of fine particles and grain growth [23]. Basically powder characteristics can be controlled by controlling reaction conditions for these two mechanisms and their relations with each other.

Nucleation is a distinct thermodynamic phase formation and can be divided into two sub categories. *Homogeneous* nucleation takes place without any effect from external addition into the solution or from the interior walls of the reaction holder. When these effects are present in the nucleation reaction, the process is called *heterogeneous* nucleation.

Homogeneous nucleation of solid particles in a solution is analyzed by classical nucleation theory developed for vapor – liquid, vapor – solid nucleation [24]. According to this theory, in super saturated vapor phase consists of atoms or molecules, thermal fluctuations leads to density and free energy fluctuations. Density fluctuations make atoms to form clusters which are called *embryo*. Atoms from the vapor phase can join these embryos and by this addition embryos grow. Smaller embryos have higher vapor pressure than larger embryos therefore, smaller ones tends to evaporate back to the vapor phase. As a result, there is a critical radius for embryos to remain in liquid phase and grow larger. This critical radius represented by r_c and Gibbs free energy required to form an embryo with radius r_c is ΔG_c. Therefore, embryos with radius $r < r_c$ can grow. Related equations are:

$$\boldsymbol{r_c} = \frac{\boldsymbol{2\gamma v}}{\boldsymbol{k}\mathbf{Tln}(\boldsymbol{S})} \tag{1.1}$$

$$\boldsymbol{\Delta G_c} = \frac{\mathbf{4}}{\mathbf{3}}\boldsymbol{\pi r_c^2 \gamma} \tag{1.2}$$

$$S = p/p_0 \tag{1.3}$$

where γ is the specific surface energy of a cluster, v is the volume per molecule in a liquid molecule condensates in a vapor media, k is boltzman constant, T is absolute temperature, p is the pressure of supersaturated vapor pressure while p_0 is the vapor of saturated vapor pressure. With the increase in S, the super saturation ratio, atomic or molecular bombardment rate in vapor increases thus the ΔG_c and r_c decreases. As a result subcritical embryos can grow into supercritical size rapidly. Figure 1.5 shows the graphical representation Gibbs free energy vesus nucleus radius and the stability of a nucleated particle.

In Ceramic powder synthesis, nucleation usually occurs from liquid and solution [25]. In an aqueous solution, metal ions are hydrated [26]. Embryos are formed by addition of metal ions by a polymerization process. After the concentration of these polynuclear ions is reached to the critical supersaturation concentration nucleation takes place.

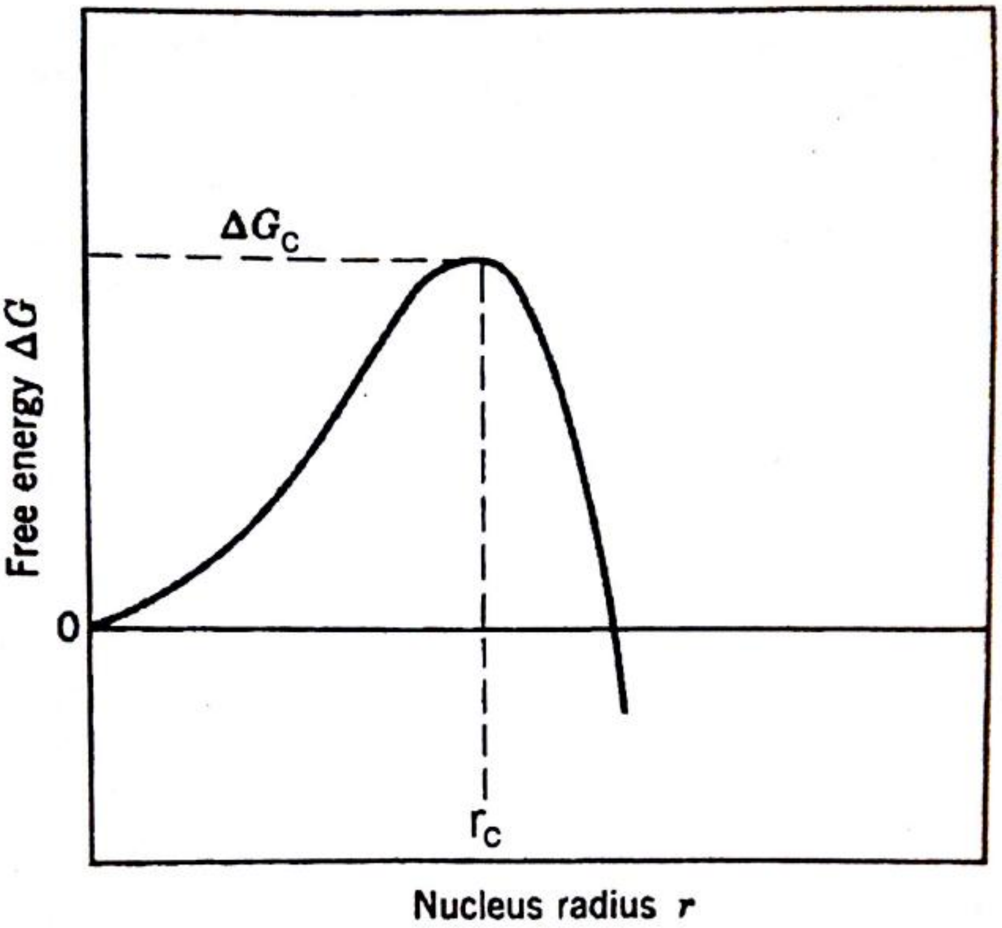

Figure 1.5 Graphic of Gibbs free energy versus radius of a spherical droplet. A stable nucleus must have the radius greater than the critical radius [27].

Nuclei in super saturated solution can grow in different sizes. Therefore, the particles that are in the particle growth phase are not same in size. Particles can grow by atom or ion movement from the solution to the particle surface, desolvation and alignment on the surface. Rate of this process decided by following factors:

1. Diffusion towards the particle
2. Surface reaction of the new material on the surface

For the diffusion-controlled growth Fick's first law describes the material flux towards the particle with radius *r*.

$$\boldsymbol{J = 4\pi r D(C_\infty - C_s)} \tag{1.4}$$

where *D* is diffusion coefficient of the solute. Surface of the particle hypothesized to have the saturation concentration, C_S and the solute has the concentration C_∞. Mononuclear growth and polynuclear growth are two types of mechanisms for surface reaction-controlled growth. In mononuclear growth nucleation occurs on the surface of a particle and forms a layer. Once a layer is formed another layer starts to emerge. Growth proceeds layer by layer. The growth mechanism has been expressed by [23]:

$$\boldsymbol{\frac{dr}{dt} = K_1 r^2} \tag{1.5}$$

where $K_1$is a constant. For the polynuclear growth, multiple layers are formed on the particle surface at the same time because new layers are nucleated on the surface very fast. Growth rate is not depended on the surface area and has been expressed by [23]:

$$\boldsymbol{\frac{dr}{dt} = K_2} \tag{1.6}$$

$K_2$is also a constant.

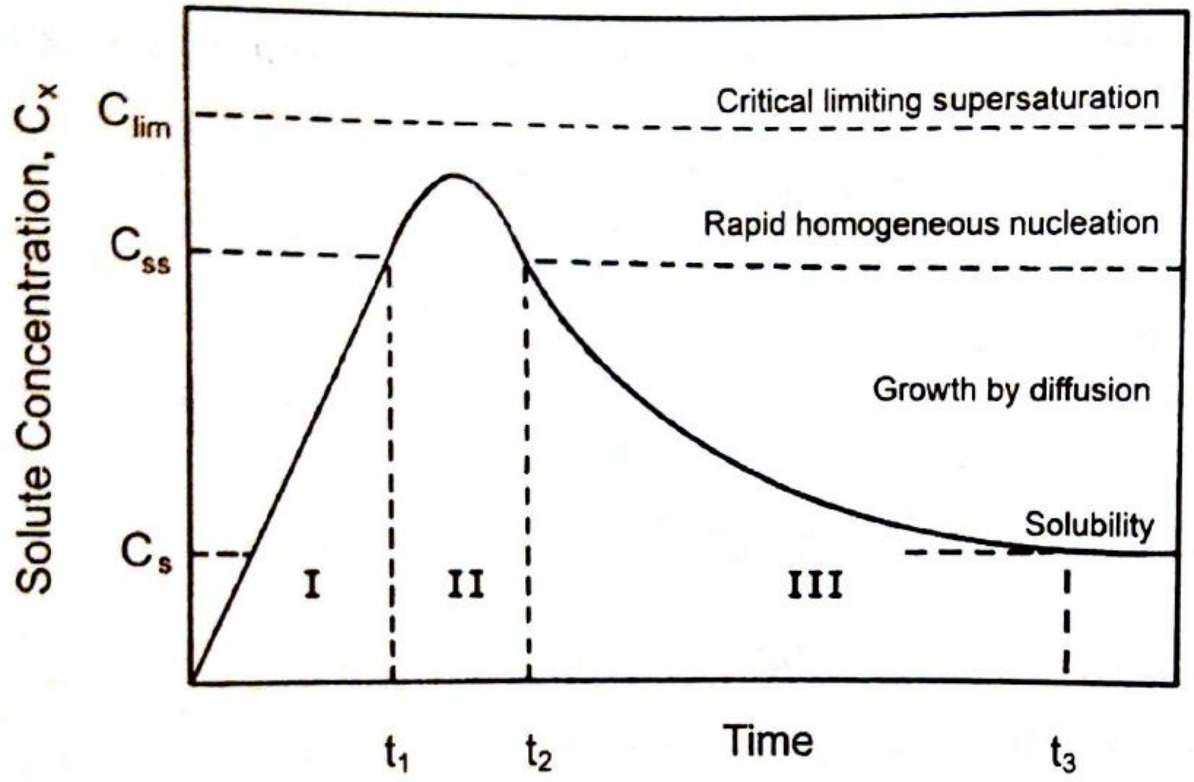

Figure 1.6 *LaMer diagram,* the graphic of the solution concentration versus time. The diagram indicates time of the nucleation and growth of the particles from a solution [28].

Figure 1.6 shows the relation between the solute concentration, C_x, and the stages of the precipitation process. If the solution is clean and free from unwanted inclusion particles C_x can exceed well above the C_{ss} and reach the supersaturation concentration at the time t_1. After the time t_1 homogeneous nucleation starts to occur and reduces the concentration, C_x, of the solute below the C_{ss} at the time t_2. Below the supersaturation concentration, $C_{ss,}$ newly formed nuclei grows by diffusion controlled mechanism until the concentration of the solute, C_x, drops below the saturation concentration, C_s, at the time, t_3. To have particles with uniform size and limit the aggregation, burst of nucleation should occur in a short t_2-t_1 time and Particle growth rate should be high enough to drop the C_x below the C_{ss} to limit the number of the nuclei as too many yields aggregation [28].

In ceramic production metal salts or metal alkoxides are usually used as precursors. Co-precipitation process is carried out by hydroxide formation of metal ions by altering the pH level.

$$\mathbf{M^{+n} + nOH^{-} \leftrightarrow M(OH)_n} \qquad \textbf{(1.7)}$$

In YAG production, pH altering solution is usually ammonia but one study suggests that ammonium hydrogen carbonate (AHG) gives better results in sinterability and phase separation [29]. Samples precipitated with AHG yields YAG phase at 900˚C while YAP phase is present at the same temperature in those precipitated with ammonia [30, 31]. Matsushita *et al* reported when urea used as pH altering agent, rate of [urea]:[metal ions] > 10.8 is important for precipitation of all the cations and for preventing phase separation [32]. Nitrates are reported to be used as starting salts effectively [30, 33-36]. Homogeneously dispersed YAG solutions can yield pure YAG with no intermediate phases after calcinations at around 800-900˚C in air.

YAG powders can be synthesized via both normal strike and reverse strike co-precipitation techniques. In normal strike(NS) the precipitant solution is added slowly into the cation solution while in reverse strike(RS) co-precipitation process, cation solution is added slowly into the precipitant solution. In normal strike, it is important to keep the pH level constant during the process in order to control the homogeneity and size characteristics of the precipitate [37]. In this method, solubility difference of aluminum and yttrium hydroxides leads to a multiphased product due to the ion exchange from the surrounding media. In reverse strike however, all of the cations are precipitated at the same time therefore, higher precipitate homogeneity can be achieved. Apte *et al.* synthesized powders from nitrate salts both via normal and reverse strike co-precipitations. Sample from normal strike had Y_2O_3 and YAM phase after calcined at 1000˚C while, pure YAG phase was achieved at 800˚C via reverse strike [37]. Li *et al.* also had similar results. YAG samples via normal strike contained YAM phase along the YAG phase even when calcined at 1500˚C. Pure YAG phase was achieved at 1000˚C via reverse strike [38]. Although reverse strike co-precipitation is a favorable method for synthesizing YAG crystals, Verma *et al.* showed that normal strike is a better option for yttrium gallium garnet (YGG) considering the optical properties of the end product [39].

Ageing also has a vital effect on the reaction and formation of the complex compound after the precipitation [40]. Ageing prevents the agglomeration during calcinations by allowing a desirable particle morphology and formation of floc structure. Li *et al.* proved that too long ageing can lead the formation of segregation in the precursor. Various samples via reverse strike co-precipitation of yttrium nitrate and aluminum sulfate left for different ageing times (30 min, 6h, 12h). 30 min and 6h aged samples were amorphous while in 12h aged sample ammonium Dawsonite ($NH_4Al(OH)_2CO_3$) crystals and an unidentified yttrium compound were present even after calcinations at 1300˚C The study concluded that secondary phases increase with the ageing time [38].

After ageing, amorphous precipitates calcined to form YAG phase. Purity and homogeneity of the precipitates allow this phase transition at lower temperatures. Crystalline or not homogeneous precipitates will harm the transparency during the sintering [30].

1.4.2 Synthesis of Complex Oxides by Co-Precipitation and Reverse-Strike Method

Complex oxides such as $\mathrm{Y_3Al_5O_{12}}$ that are consist of more than one type of metallic cation may be difficult to be synthesized via co-precipitation. The usual problem is when the different salts or different alkoxides combined in a solution, these precursors have different hydrolysis rates. In such condition segregation is likely to occur. Suitable conditions must be satisfied for all of the precursors in order to achieve homogeneous and segregation free precipitated product. Considering the co-precipitation of $\mathrm{MgAl_2O_4}$, Mg and Al have different solubility conditions. While Al tends to precipitate in mild basic solutions with $\mathrm{pH} = 6.5 - 7.5$, Mg only precipitates in strong basic solutions. However, precipitate contains a mixture of $\mathrm{2Mg(OH)_2 \bullet Al(OH)_3}$ and $\mathrm{Al(OH)_3}$ when $\mathrm{MgCl_2}$ and $\mathrm{AlCl_2}$ precursor salts is added upon a solution with constant $\mathrm{pH} = 9.5 - 10$ where neither of the metal cations are soluble. Calcination of this sample yields high purity, stoichiometric $\mathrm{MgAl_2O_4}$ powder [41].

Gluskova *et a.l* synthesized yttrium and aluminum hydroxide precursors from nitrate solution via normal-strike co-precipitation route. The results show that the calcined hydroxide powder contains YAP and YAG phase. Above the calcination temperature 950˚C several unknown phases were present in the sample [42]. Chiang *et al.* synthesized Ce:YAG via both reverse-strike and normal-strike routes from different aluminum sources at low calcination temperatures [43].

1.4.3 Co-Precipitation under Hydrothermal Conditions

Hydrothermal route is a proven method to synthesize fine sized oxide particles [44]. Hydrothermal co-precipitation is performed by heating reactants such as metal salts as a solution or a suspension under the vapor pressure. Heating temperature is usually between the boiling point and critical point of the water and pressure can be rise up to 22.1 MPa (the vapor pressure at critical point). Reaction usually takes place in an autoclave that can withstand the vapor pressure. Main aspect of the hydrothermal co-precipitation method is the forced hydrolysis with the aid of the temperature and pressure. One advantage of this method is the powder is already crystalline therefore; the calcinations step is not required. Another advantage is synthesized particles have very fine size (10nm-100nm) with narrow size distribution and good chemical homogeneity. However very fine particles synthesized via hydrothermal method are hard to consolidate to high packing density and have tendency to agglomerate [45]. Hydrothermal method is an old method for production of $\mathrm{BaTiO_3}$ ceramic powders [46]. In that method, $\mathrm{TiO_2}$ anatase phase reacts with strong base solution of $\mathrm{Ba(OH)_2}$ (pH > 12-13) at 150-200˚C.

Takamori *et al.* reported that pure YAG phase can be obtained via hydrothermal route [47]. Chloride and nitrate salts of yttrium and aluminum were mixed in stoichometric ratios at pH 3 and $\mathrm{NH_4OH}$ was added to set pH to 9. Precipitated hydroxides of metal cations were collected via freeze drying. Calcination carried out in different temperatures between 400-700˚C to evaporate the ammonium impurities and obtain amorphous powder. Precursor powder suspension was sealed in a platinum capsule and kept at 100 MPa and 500-550˚C for 15-20 h. Obtained amorphous powders heat treated between 800 and 950˚C to obtain crystalline phase.

1.4.4 Solid-State Method

Solid state reaction method is most common ceramic production method. Solid state reaction method is simply the direct reaction of a mixture of starting solid phase chemicals (usually powders) at high temperatures, which is required to supply enough energy for the reaction to occur. Contact between the grains of the chemicals is very important because diffusion of chemicals in order to form the final product start at the interface. The main reaction mechanism and the rate controlling step in solid state reactions is the diffusion. Since the diffusion of the cations through the product layer at the interface is required, solid state reactions are usually very slow and long reaction times from a couple of hours to several days may be required. Reaction rate increases at higher reaction temperatures. One of the determining factors for the efficient solid state reaction is mixing through the reagents in stoichiometric amounts. Solid state reaction method has been commonly used for transparent YAG production. In solid state reaction Al_2O_3 and Y_2O_3 (and dopant powders) are mixed via ball milling which mixes all the reagents through and through. After milling the samples are green formed and sintered. Mixed powders go through phase formation during the sintering step. Al^{3+} ions diffuse into Y_2O_3 as Al^{3+} ions are faster than Y^{3+} ions, Al^{3+} ions diffuses into Y_2O_3. Three phase transformations have been reported in the literature [48]. Phase formations progress through $\mathrm{YAM} \rightarrow \mathrm{YAP} \rightarrow \mathrm{YAG}$ transformations. Kinetics of the system is the main factor during the transformations. Generally YAM phase starts to form at around 900 to 1100˚C, YAP phase at around 1100 to 1250˚C and YAG phase at around 1400 to 1600˚C. These formation temperatures depend of the kinetics between the Al^{3+} and Y^{3+} and lower particle size of the starting powders reduce the temperatures because of the enhanced diffusion.

One study showed that the particle size strongly affects the kinetics of the system [49]. Smaller particle sizes enhance the diffusion by reducing the diffusion distances. Smaller particles increase the diffusion as they maximize the surface area of the whole system. Ikesue *et. al.* reported that starting powders affect the volumetric expansion during the sintering [48]. Limited transparency in the samples with large volumetric expansion was also reported. High transparent samples were only be able to achieved with inhabitation of the expansion [50]. Although Ikesue *et. al.* suggested the particles with size below 60 nm to obtain transparency during sintering the exact mechanism of how particle size causes or inhibits volumetric expansion is unknown.

1.4.5 Sol-Gel and Citrate Methods

In sol-gel method, metal ion solution or suspension of fine particles called as sol, transformed into viscous gel. Starting with a suspension of fine particles, colloidal particles attached to each other by surface forces during the chelation. If metal ion solution used as a precursor, polymer network is formed by hydrolysis and condensation reactions. Metallic salts solutions are frequent precursors for sol-gel reactions. When the solution is heated around ~50-90˚C with the sufficient concentration of reactants and the pH of the solution, hydrolysis and condensation may occur which results in polymerization reaction. Hydrolysis reaction of the hydrated metallic cations can be expressed as:

$$\mathbf{[M(H_2O)_n]^{z+} + H_2O \leftrightarrow [M(H_2O)_{n-1}(OH)]^{(z-1)+} + H_3O^+} \tag{1.8}$$

Condensation reactions of the hydroxylated metallic cations takes place by olation or oxolation. Negatively charged $\mathrm{OH^-}$ group attaches to the hydrated metallic cation in olation while two OH groups forms a water molecule and an oxo bridge in oxolation. Olation and oxolation reactions can be represented respectively by [51]:

$$-\mathbf{M}-\mathbf{OH}+\mathbf{H_2O}-\mathbf{M}\rightarrow\mathbf{M}-\mathbf{OH}-\mathbf{M}+\mathbf{H_2O} \tag{1.9}$$

$$-\mathbf{M}-\mathbf{O}-\mathbf{H}+\mathbf{H}-\mathbf{O}-\mathbf{M}-\rightarrow-\mathbf{M}-\mathbf{O}-\mathbf{M}-+\mathbf{HOH} \tag{1.10}$$

Polymerization of the products formed by hydrolysis and condensations reactions increase the viscosity of the system and creates a gel. Due to the excess liquid content is used in the formation of the gel, solid loading of the gel is usually as low as 5-10 vol%. Before the calcinations process this excess part of the gel must be removed. During the drying process evaporation must occur slowly or the gel may be exposed to a high value of stress. Ageing prior to the drying strengthen the gel and reduces the probability of a possible crack [52]. Along with water gel also contains organic groups. These groups need to be removed below ~500˚C before the sintering process. Usually ceramic powders synthesized via sol-gel, require less temperature for densification because of higher surface activity of sol-gel derived nano-powders [53]. Other advantages of sol-gel method are high purity end product, exceptionally good homogeneity. Because of the mixing of the materials is in molecular level, complex oxide compounds can be synthesized via sol-gel.

The citrate gel method is a modified sol-gel method and invented to produce ceramic superconductors [54]. Nitrate solutions of metallic cations are added to the citric acid solution. pH is kept constant to prevent the precipitation. Heating the solution ~10˚C below to the boiling point of the water produces viscous polymeric chelates. Chelates immobilize the metal ions and distribute them in the polymeric network homogeneously [55]. Sample is heated until the polymeric resin is burned out and amorphous solid is obtained. Burning the chelated sample at high temperatures breaks the polymer network. Ashes of the burned sample contain the atomistically distributed metal ions. Low mobility of the cations in highly viscous polymer resin prevents segregation during pyrolysis [56]. Calcination at an elevated temperature yields crystalline powder. Another advantage of the citrate method is its applicability for a wide range of metal cations thanks to the excellent ability of citric acid to solve metal cations.

For YAG production there are several powder synthesizing methods [57] [58, 59] [60] [61] [62]. However, Sol-gel methods have better than the other wet chemical synthesis methods because of the chemical interaction of cations, results in atomic level distributions of cations. As stated before, less energy during calcinations is required to have a pure YAG end product with no secondary phases. Several studies show that via sol-gel pure YAG phase can be achieved as low as 800˚C [63] [64].

1.5 GREEN FORMING

Slip-casting and die-pressing are conventional methods that are used in traditional ceramics for powder consolidation and forming of ceramics for many years. They offer good control over the consolidation and also flexibility of complex shaping. Packing of the particles can be characterized by packing density and coordination numberwhich is the number of neighboring particles around any given particle.

Packing density is the fraction of the solid content in the green body::

$$\mathbf{Packing\ denstiy} = \frac{\mathbf{volume\ of\ solids}}{\mathbf{total\ volume\ of\ the\ green\ body\ \ (solid+vacancy)}} \qquad (1.11)$$

1.5.1 Slip Casting

Slip casting is one of the several casting methods in ceramic production. All of the casting methods use colloidal systems and are relying on the evaporation of the liquid in such systems to consolidate the particles. Slip casting is a very old technique for clay shaping and pottery. Slip is slurry of ceramic powder and liquid suspension. In slip casting colloidal suspension (slip) is poured into a porous mold (plaster of Paris) and the mold creates a liquid flow. Withdrawal of the water carried out by capillary pressure due to the porosity of the mold. During the water withdrawal solid content accumulates at the mold surfaces. When the desired thickness is achieved the slip can be poured out of the mold. During the drying cast usually shrinks and can be removed easily. Before the sintering step, cast should be heated to burn out the organic content such as binder and dispersant agents [65].

During slip casting a liquid flows through a porous medium. Darcy's law expresses this phenomenon by:

$$\boldsymbol{J} = \frac{\boldsymbol{K}(\frac{\boldsymbol{dp}}{\boldsymbol{dx}})}{\boldsymbol{\eta_L}} \qquad (1.12)$$

where the J is the flux of the liquid, K is the permeability of the plaster mold, $\frac{dp}{dx}$is the pressure gradient of the liquid and η_L is the viscosity of the liquid. During the process, the liquid passes through two porous media: the mold and consolidated powder. If the resistances of cast and mold taken into account the capillary pressure can be expressed by:

$$\boldsymbol{p} = \Delta \boldsymbol{p_c} + \Delta \boldsymbol{p_m} \qquad \textbf{(1.13)}$$

where Δp_c is hydrolic pressure drop in the cast and Δp_m is the hydrolic pressure drop in the mold. As the pressure drops are linear the flux must be the same in both media.

$$\boldsymbol{J = \frac{K_c}{\eta_L L_c}\Delta p_c = \frac{K_m}{\eta_L L_m}\Delta p_m} \qquad \textbf{(1.14)}$$

where the $K_c$and K_m are the permeability of the cast and the mold respectively, $L_c$is the thickness of the cast, $L_m$is the thickness of the mold and $\eta_L$is the viscosity of the liquid [66].

In order to achieve good packing, quality of the slip is very important. Flocculation in the slurry results in porosity in the cast. Cast with porosity and agglomerates have poor microstructural control during sintering step. A good and homogeneous microstructure after sintering depends on how well dispersed and agglomerate free the slurry is. Moreover, size distribution and shape of the particles also affect the packing density of the cast. Segregation occurs because larger particles accumulate on the mold surface faster than the smaller particles. Figure 1.7 shows the effects of the particle size, flocculations and shape of the particles on the packing density. From the figure, spherical and bigger particles are less likely to flocculate therefore yield less porosity in the microstructure. Steps of slip casting is represented at figure 1.8. After the slurry is prepared by mixing of the ceramic powder, water and chemical agents, slip is casted into the plaster of paris mold. The mold withdraws the ware and the green body is ready for sintering.

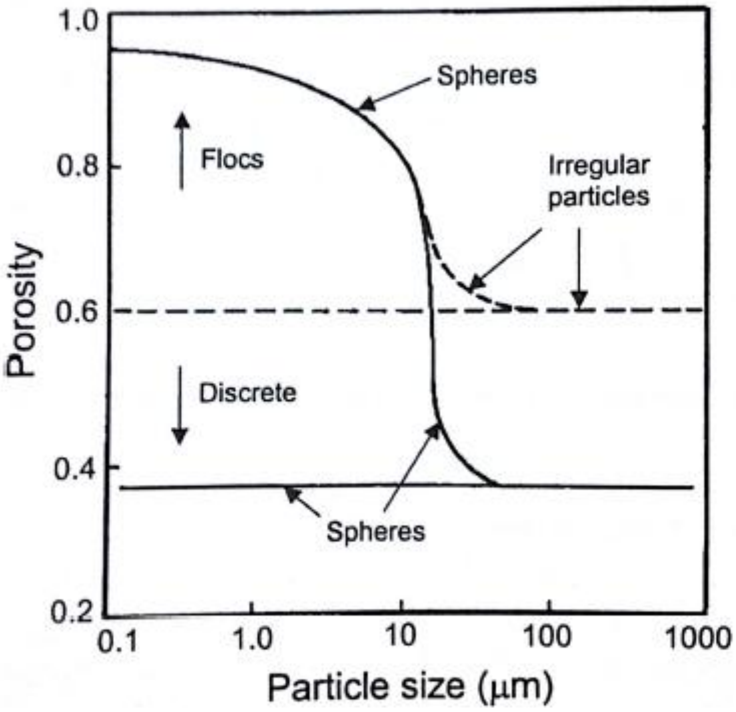

Figure 1.7 Graphical representation of the relation between the packing density and particle characteristics [66].

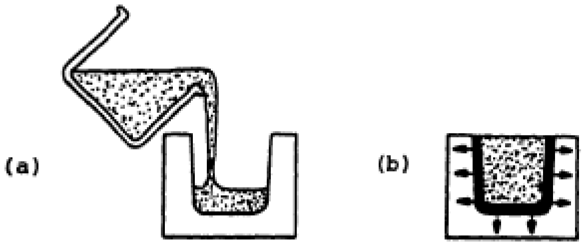

Figure 1.8 Schematically representation of the slip casting process. (a) Mold is filled with slip, (b) mold sucking pressure of the mold withdraws the water and the solid content accumulates along the wall of the mold [67].

Along with water slip also contains dispersant, and binder agents that change viscosity and flow properties. Dispersants inhibit flocculation by creating or increasing a repulsive force between particles either by electrostatically, sterically or both. In electrostatic repulsion, electrical double layer is formed on each particle surface and when the two of these layers collapse they repulse each other. If the repulsion is strong enough it can overcome the attractive van der Waals force and the slurry become stable. Figure 1.9 shows the charge density around the particle and formation of double layer.

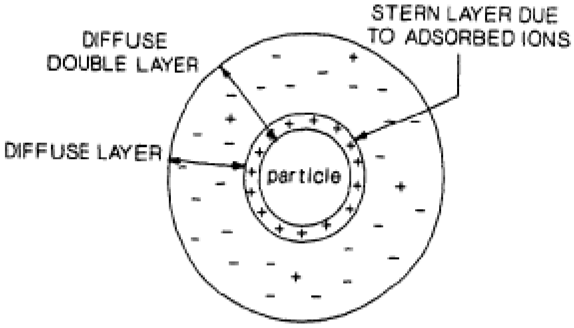

Figure 1.9 Charged particle surrounded by diffuse double layer [67].

Figure 1.10 shows the attractive and repulsive forces between two particles. Resultant curve shows a two minimums at M_1 and M_2 and a maximum in between M_1 and M_2. For two particles with the M_2 distance between each other, if the thermal energy is lower than the depth of M_2 flocculation occurs. Attractive forces are constant depending on the given system. Therefore increasing repulsive forces can eliminate the minimum points of the resultant curve and the gain stability to the system.

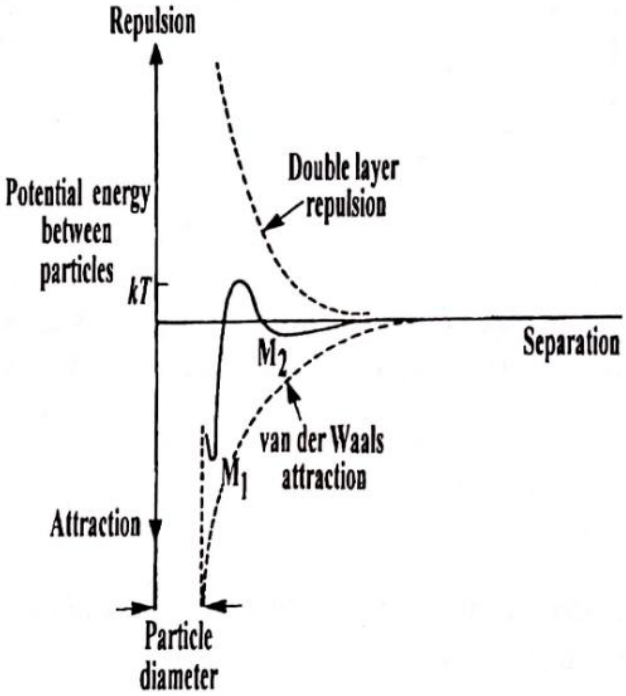

Figure 1.10 Van der Waals attraction and the double layer repulsion forces of two particles in a slurry [27].

Steric force is another repulsive force that affects the stability of the suspension. When polymer coated particles in contact with each other they repulse each other (steric effect).

Ion exchange occurs between colloidal particles, media and dispersant. Ion exchange leads into the electrostatic forces. Another effect of the dispersants is steric effect due to the accumulated polymers on the particle surface repels each other. Both electrostatic forces and steric effects changes the rheology of the slip. One or both of these two effects can occur in slurry depending on the type of the dispersant [68, 69].

Slip casting is favored by ceramic industry over the dry pressing because the slip casted parts have higher and more uniform density than pressed ones.

Slip for good end product should have following qualities [65]:

- Low viscosity to be poured in to the mold
- No settling or agglomerations
- Fast but not too rapid casting rate
- Low shrinkage during drying
- High green strength after casting
- Can be drained clean enough

Colloidal size of the particles affects some characteristics of the particles change such as total surface area, diffusion rates, sedimentation rates and coagulation rates. Small particles within the colloidal range (10nm-100nm) have good sinterability and densification properties. Two mechanisms can be observed due to the small size of the particles:

- *Brownian Motion* is random motions of a small particle in a liquid to the constant bombardment of atoms of the liquid. This motion changes the velocity and direction of particles.
- *Vander Waals Forces* are week short range attractive forces between atoms or molecules. Depending on the dispersant in the ceramic slip these forces can be either repulsive or attractive.
- *Charge Effects* may be present at base pH even without any dispersant depending on the type of the particles and the media. Addition of the polymer ions in form of dispersants can greatly reduce the chance of coagulation and settling. Dispersant molecules attach themselves onto the surface of the particles or induce a charge by closest particles. Therefore each particle coated with an electrostatic thin layer.

By controlling these three factors slip can have desirable characteristics.

1.5.2 Densification and Sintering

In ceramics rigid body with desired micro structure can only be achieved through sintering. The green body, whether produced by slip casting or dry pressed, is a very porous. This porosity must be eliminated in the end product in order to achieve transparent ceramic sample. Porosity elimination occurs by two elements: material transport mechanism and source of energy to activate this mechanism. Material transport can take place by different mechanisms of diffusion. Some of these mechanism s results in shrinkage and decrease the distance between particles by eliminating porosity.

During the sintering, free energy of the system decreases. Driving force of the process comes from the curvature of the free surfaces. For smaller particles curvature is high as well as the free surface energy. The effects of sintering are enhanced when the curvature is high. This phenomenon explains why ceramic processing is based on synthesizing fine particles. Pressure is also is a driving force if applied. Matter transportation during sintering is carried out by diffusion. Diffusion in sintering can occur in different mechanisms in different sintering types. In polycrystalline ceramics there are six different diffusion mechanisms during sintering. All of the methods leads into bonding and neck growth between particles. Therefore the consolidated powders gain strength during sintering. However not all mechanisms provide shrinkage and densification. Figure 1.11 shows the diffusion mechanisms occur during sintering. Surface diffusion, lattice diffusion from the surface and vapor transport mechanisms do not cause densification. Grain boundary diffusion and lattice diffusion from grain boundaries cause densification. Plastic flow also cause densification but it is not common in ceramic samples usually occurs in metal powders. One important aspect of sintering is, both densifying and nondensifying mechanisms will decrease the curvature during the process. Therefore, occurrence of nondensifying mechanisms reduces the rate of the densifying mechanisms.

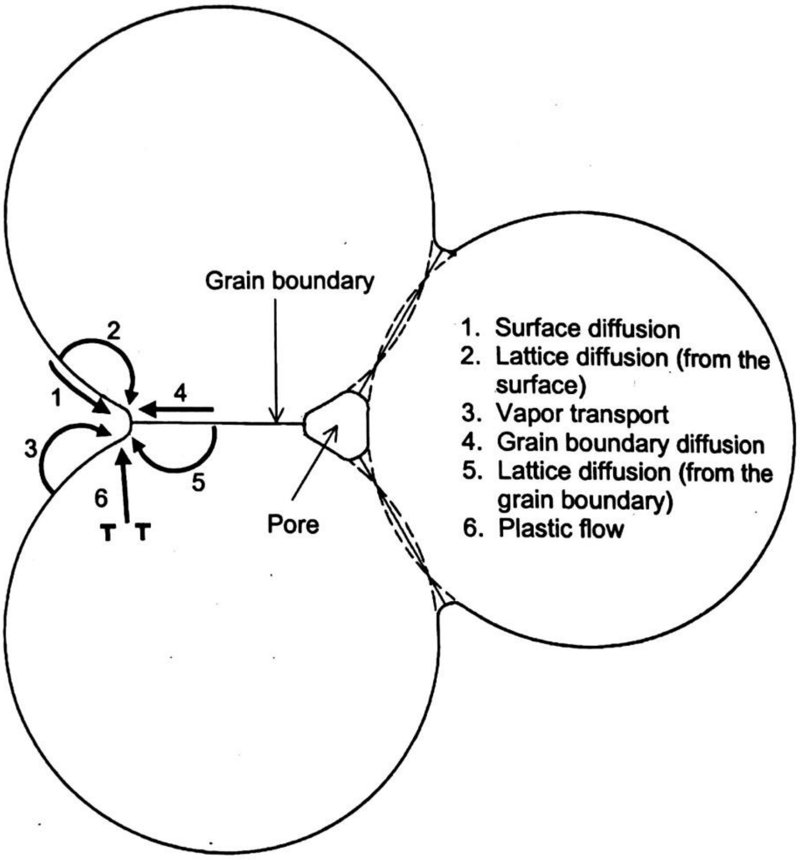

Figure 1.11 Diffusion mechanisms between crystalline particles during sintering: (1) Surface diffusion, (2) lattice diffusion from the surface, (3) vapor diffusion, (4) grain boundary diffusion, (5) lattice diffusion from the grain boundary, (6) plastic flow [27].

During the sintering of polycrystalline particles pores tends to form grain boundaries as a response to decrease in free surface energy. While grain boundaries migrate grains tends to grow to reduce the free energy. Figure 1.12 shows a representation of a pore surrounded by three crystalline grains. γ_{gb} is grain boundary energy, $\gamma_{\mathrm{sv}}$is surface energy and Ψ is angle between two particles. Balance of the energies is represented in equation (1.15):

$$\boldsymbol{cos}\left(\frac{\boldsymbol{\Psi}}{\mathbf{2}}\right)=\frac{\boldsymbol{\gamma_{gb}}}{\mathbf{2}\boldsymbol{\gamma_{sv}}} \tag{1.15}$$

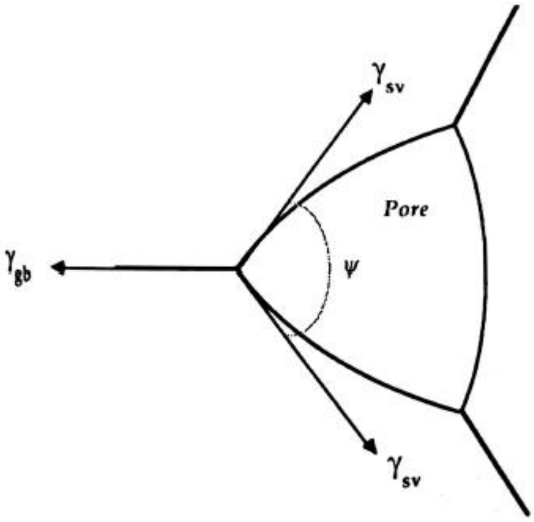

Figure 1.12 Shape of a pore when balanced by internal and external forces during sintering. $\boldsymbol{\gamma_{\mathrm{gb}}}$ is grain boundary energy while $\boldsymbol{\gamma_{\mathrm{sv}}}$ is surface energy. Ψ is angle between two particles [27].

Pores, surrounded by few grains, have concave shape and shrink during the sintering as the surfaces progress towards the center of the pore during the grain growth. Therefore, the pores shrinkage and densification of the whole sample occurs. However, when too many grains surround a pore, the pore has convex shape due to balance of forces. In this case, the pore growth occurs rather than pore shrinkage and phase coarsening of the sample.

The first transparent YAG ceramics sintering in literature was in 1984 by De With and Van Dijk [70]. They used Y_2O_3 and $Al_2(SO_4)_3$ as starting powders and spray drying method. After the calcinations at 1300˚C for 6h, they obtained the garnet phase. Powders were sintered with the aid of 0.15 wt% SiO_2 or 0.05 wt% MgO sintering agents. For shaping and consolidating garnet powders they used dry press. Samples' density was 100% after they were sintered at 1450˚C for 8h and 1850˚C for 4h in vacuum respectively. Transmission of the MgO doped samples were less than 50% while transmission of the SiO_2doped samples were up to 80% in the wavelength of 5 µm. However the first laser efficiency in polycrystalline YAG comparable to the efficiency of the single growth crystals were first reported in 1995 by Ikesue *et al* [48]. The 1% Nd doped YAG samples were prepared by solid state reaction method using 0.14 wt% SiO_2 as sintering agent. Samples were sintered at 1750˚C for 50 h in vacuum. TEM images of the samples proved that the grain boundaries were free from any other distinctive phase. Later in 2002 Lu *et al.* reported laser efficiency in co-precipitated 1% doped Nd:YAG samples [71]. Garnet phase was obtained after calcinations at 1200˚C. In the original article no sintering agent was reported however, one later article stated that SiO_2 was used as sintering agent in the original article [7]. Slip casted samples were sintered at 1750˚C for 5 to 20 h to achieve transparency.

1.6 Effects of SiO_2 in Transparency

SiO_2 is vital to obtain transparency in polycrystalline ceramics [72]. Main light scattering points in translucent or transparent polycrystalline ceramics are residual pores. In order to produce highly transparent ceramics residual pores must be eliminated [73]. Usually pressure assisted densification techniques such as hot pressing can eliminate the pores. However, these methods are not preferable due to high cost and contamination problems.

SiO_2 forms a liquid phase at 1400˚C and eliminates the residual porosity in the ceramic microstructure. Stevenson *et al* showed that both densification and grain growth in Nd:YAG are proportional with the SiO_2 content [74]. Higher SiO_2 content reduce the sintering temperature and time that required for densification. Samples with low SiO_2 content can be fully dense if they are sintered at relatively high temperatures but they still have lower grain size compared to those with higher silica content [74]. Ikesue *et al.* showed that in solid state reaction of YAG polycrystalline ceramics doping 0.14 wt% SiO_2 is vital for transparency. 0.14 wt% SiO_2 doped samples had similar laser slope efficiency as in Czochralski grown crystals [48]. Samples contained YAP phase when sintered without the SiO_2 sintering agent [75]. Grains size was reported to increase with the increasing SiO_2 content. Ikesue *et al.* concluded that SiO_2 was a phase formation agent as well as sintering agent. Maitre *et al.* reported an endothermic reaction in SiO_2 doped 1% Nd:YAG samples [76]. This reaction was attributed the liquid SiO_2 phase formation during the sintering. Kochawattana *et al.* hypothesized that SiO_2 liquid phase increases both densification and grain growth [77].

1.7 Energy Structure of Ce^{+3} and Eu^{3+}

Ce^{3+} has electronic configuration of $|\mathrm{Xe}|4f^1$ and has five transitions from the 4f-5d levels [78]. The energy gap between the lowest 5*d* orbital and the ground state is 20,000-35,000 cm^{-1} and 4*f* ground state splits into $^2\mathrm{F}_{5/2}$ and $^2\mathrm{F}_{7/2}$ by the spin-orbit interaction. However, only the $^2\mathrm{F}_{5/2}$ energy level has an electron at the room temperature. Crystal field splits 5d orbital into five energy levels. Splitting energy gap is 2,200 cm^{-1} [79]. Emission spectrum of Ce^{3+} consists of two peaks and a broad band near UV region. When Ce^{3+} ions doped into a YAG crystal Ce^{3+} ions distort the cubic structure of the YAG due to the size difference of Ce^{3+} and Y^{3+} ions and 5*d* orbital of Ce^{3+} ion splits into a high energy triplet (t_{2g})

and a low energy doublet (*e_g*) by the crystal field. Figure 1.12 shows the band structure and energy levels of Ce^{3+} ion when doped into the YAG host [80]. Optical radiation with wavelengths longer than the band gap of the YAG (the 56,012 cm^{-1}) will excite the Ce^{3+} ions. Therefore the optical properties of Ce:YAG depends on the 4*f* and 5*d* energy levels of Ce^{3+} ion.

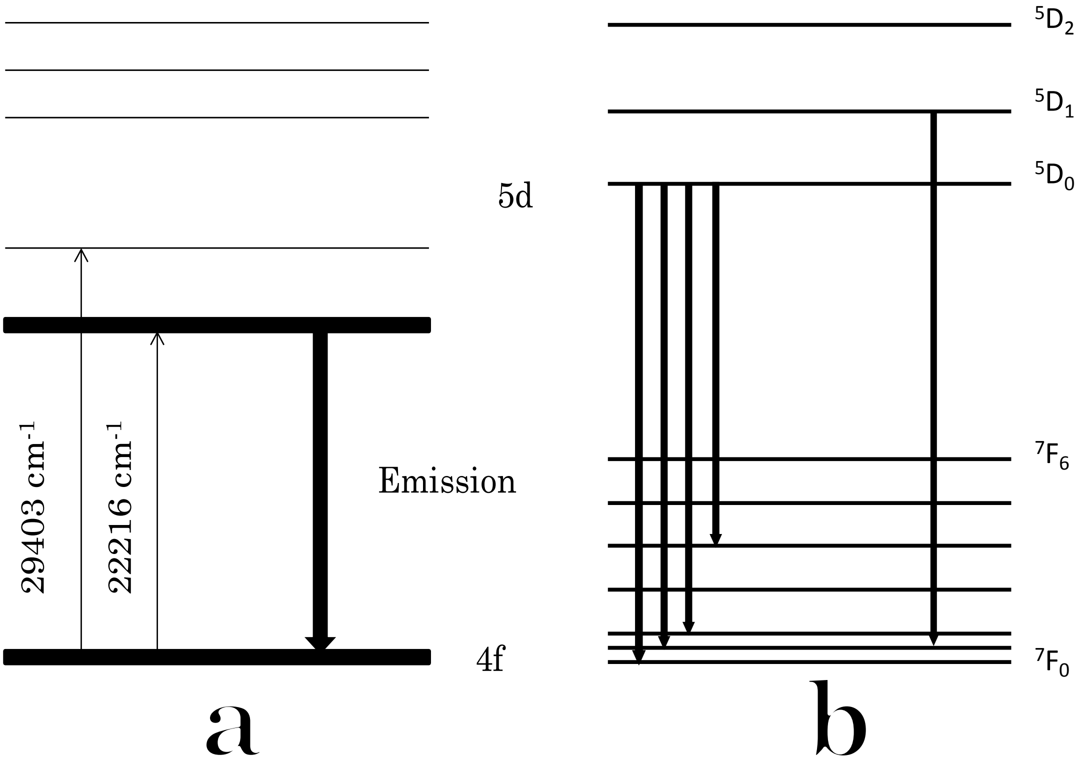

Figure 1.13 Energy levels of (a) Ce^{3+} and (b) Eu^{3+} ions.

Eu^{3+} has the electronic configuration of [Xe]$4f^6$ and ground state of the trivalent ion is $^7F_0$. Ground state splits into seven ^7F_J energy levels (J=0, 1, 2, 3, 4, 5, 6) by spin-orbit introductions. Between 550 nm and 750 nm trivalent europium ions have five transitions of $^5D_0 \rightarrow {}^7F_J$ (J = 0,1,2,3,4). Energy difference between the ground state and the lowest 5d orbital is 17210 cm^{-1}. Eu:YAG has emission peaks at red and infrared region of visible light spectrum. Figure 1.13 shows the energy levels of trivalent europium ion at the right hand side.

CHAPTER 2 Synthesis of Yttrium Aluminum Garnet (YAG)

2.1 Introduction

In 1960s first polycrystalline ceramic solid state laser material, dysprosium doped fluoride ($\mathrm{Dy{:}\,CaF_2}$) was reported [81]. Second polycrystalline ceramic laser reported was $\mathrm{Nd^{3+}}$ doped oxide yttralox ($\mathrm{Y_2O_3{:}\,ThO_2}$) [82]. However only with the recent developments polycrystalline ceramic lasers became an promising research topic.

First studies reported trials of synthesizing transparent ceramics resulted in translucent ceramic samples [83]. Translucent ceramics however were not successful in laser oscillation due to the light scattering points in the microstructure such as grain boundaries, secondary phases, and pores. Peelan *et al.* showed that transparent alumina samples can only be achieved by eliminating the residual porosity [73]. In 1995 Ikesue *et al.* reported a successful laser oscillation using neodymium doped transparent polycrystalline yttrium aluminum garnet ceramic with a similar performance to the single crystal laser oscillation [84]. Previously, YAG crystals for laser operations were being synthesized by growth from single crystal method also known as Czorchralski method. While the method offered by Ikesue *et al.* was a common method for production of advance ceramics, it had many advantages compared to the conventional Czorchralski method such as low cost, fast production capabilities and not requiring high tech equipment. Having many advantages against the conventional method, the polycrystalline ceramic method was even better than their growth from single crystal counterpart in terms of homogeneous dopant concentration, ability to be synthesized in complex and large shapes and allowing the production of novel laser materials. In 2002 Lu *et al.* reported that they can produce bulk transparent Nd:YAG samples up to 203mm long using co-precipitation method [71]. Micro structures of the reported samples had clean grain boundaries with no secondary phases and samples had no residual porosity.

Nd:YAG polycrystalline ceramics have been proven to be a better candidate than their single crystal counterparts in laser operations [4, 85, 86]. Laser performances of the polycrystalline ceramics are even better at high output powers because ceramic laser materials do not have the scattering from the residual stresses induced bifringence as in single crystal laser materials [86].

2.2 EXPERIMENTAL

2.2.1 Powder synthesis

2.2.1.1 Solid-State Method

Figure 2.1 shows the flow chart of the YAG powder synthesis process via solid state method. Stoichiometric amounts of α-Al_2O_3 (99.999%, Alfa Aesar) and Y_2O_3 powders (99.999%, Alfa Aesar) were put into a ball-mill container. TEOS (Alfa Aesar 99.99%) as a sintering aid was calculated to the end samples containing 0.28 wt. % SiO_2. 0.75 wt% PEG (Sigma Aldrich 200MW) used as binder and 2 wt% dolapix (Eurokimya) used as dispersant. Distilled water was used as a milling media and zirconium (ZrO_2) balls were added into the container. Solid content ration of the samples were 20 wt. % while ball to powder ration was 3/1. Samples were milled at 200-300 rpm for 20 h. After milling, samples were left for drying at 90˚C overnight. Dried powder was crushed with mortar and pestle. Powders were dry pressed at 20 MPa and isostatically pressed at 200Mpa afterwards. Figure 2.2 shows the schematic representation of the process.

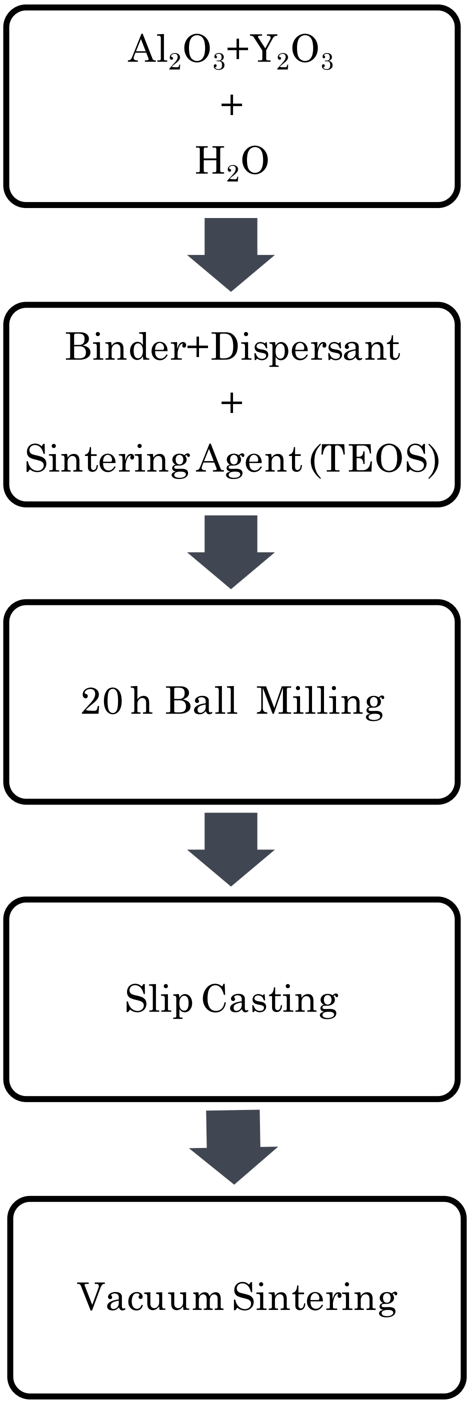

Figure 2.1 Flow chart of the solid-state method.

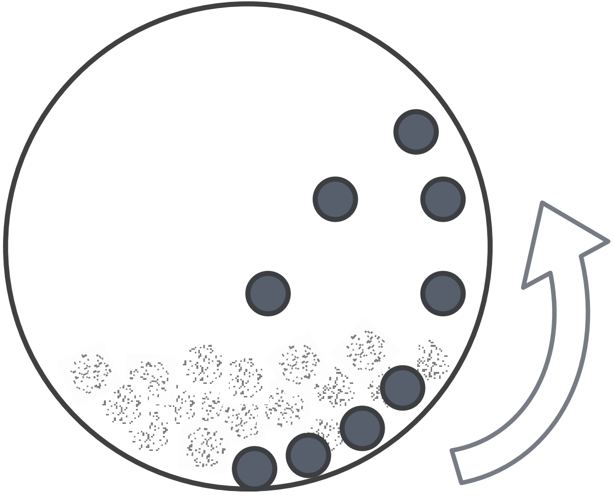

Figure 2.2 Schematic representation of solid state-method.

2.2.1.2 Citrate Method

$Al(NO_3)_3{\cdot}9H_2O$ (99.999%, Alfa Aesar) and citric acid (Alfa Aesar) were dissolved in distilled water. $Y(NO_3)_3{\cdot}6H_2O$ (Alfa Aesar 99.9%) and $Ce(NO_3)_3{\cdot}6H_2O$ (99.5%, Alfa Aesar) or $Eu(NO_3)_3{\cdot}6H_2O$ (99.9%, Alfa Aesar) solution was added upon the first solution. Nitrate salts of metal ions were calculated in stoichiometric ratios to yield 1% doped YAG in the end product. Al^{3+} ion to total H_2O molar ratio was 1:10 while Citric acid to total cation molar ratio was 3:1. Schematic of starting solutions are shown in figure 2.3

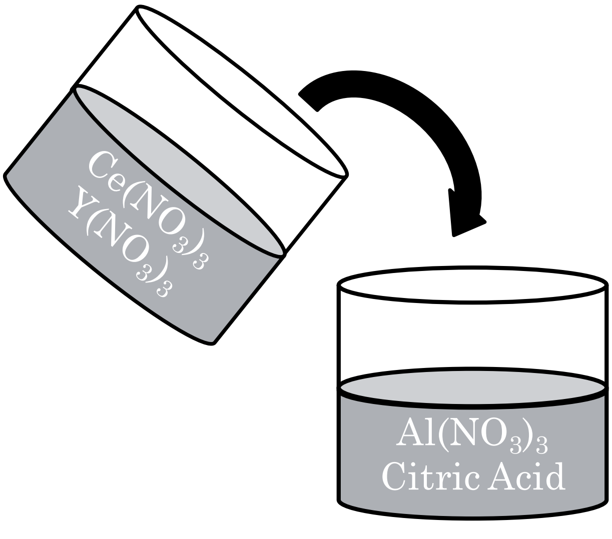

Figure 2.3 Schematic representation of citrate method.

Under constant stirring, the combined solution was heated to 90˚C. After the excess water evaporated temperature was risen to 300˚C and kept until the white foam like structure burned out completely. The acquired ash was heat treated at 3˚C/min heating rate to 900˚C and held for 3h to get pure YAG phase and to obtain around 100 nm particle size and around 35 nm crystallite size. Flow chart of the process is shown in figure 2.4.

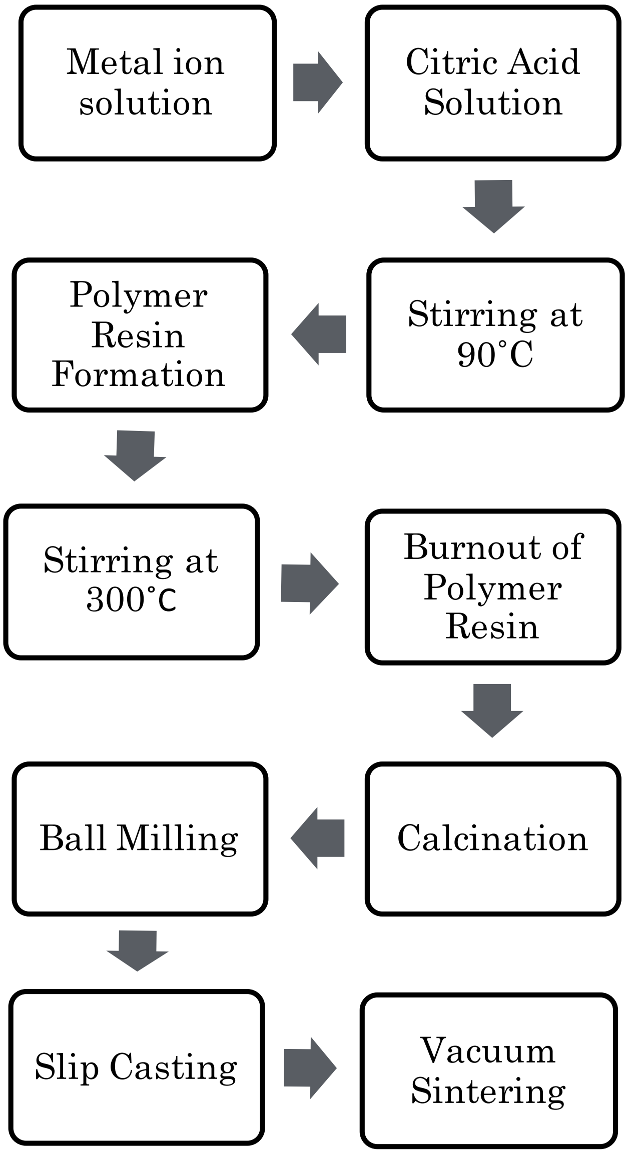

Figure 2.4 Flow chart of the citrate method.

2.2.1.3 Normal-Strike Co-precipitation Method

0.067 M metallic cation solution of $Al(NO_3)_3 \cdot 9H_2O$ (99.999%, Alfa Aesar), $Y(NO_3)_3 \cdot 6H_2O$ (Alfa Aesar 99.9%) and $Ce(NO_3)_3 \cdot 6H_2O$ (99.5%, Alfa Aesar) or $Eu(NO_3)_3 \cdot 6H_2O$ (99.9%, Alfa Aesar) was prepared in stoichiometric amounts to form 1% doped YAG samples. 13.4 M NH_3 solution added upon constantly stirred metal cation solution. Figure 2.5 shows the flow chart of the process. pH of the solution checked and reported during the experiment. After the precipitated sample was acquired, it was left for ageing for 24h at 60˚C. Sample was washed and centrifuged with distilled water after the ageing process until pH was around 7. Washed precipitate was dried at 90˚C for 24h and grinded via mortar and pestle. Powder obtained was calcined at various temperatures between 900-1300˚C to obtain the garnet phase with particle size around 100nm and crystallite size around 35nm and to evaporate the excess chemicals.

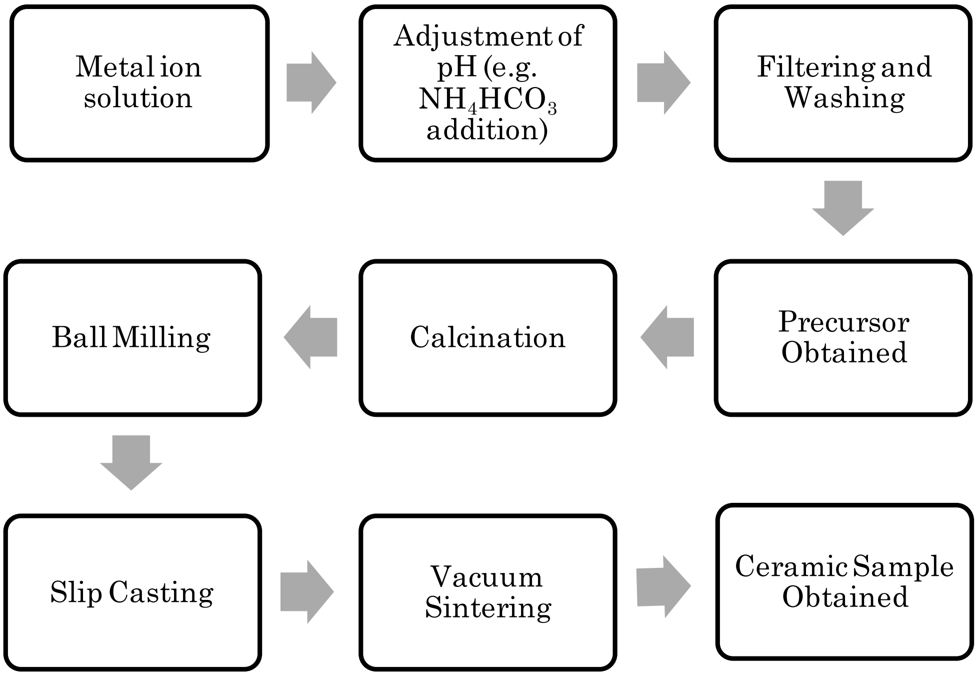

Figure 2.5 Flow chart of the normal-strike route of the co-precipitation method.

2.2.1.4 Reverse-Strike Co-precipitation Method

Ce:YAG and Eu:YAG powders were synthesized via reverse strike co-precipitation of 1.5 M aqueous solution of $Al(NO_3)_3 \cdot 9H_2O$ (Alfa Aesar 99.999%), $Y(NO_3)_3 \cdot 6H_2O$ (Alfa Aesar 99.9%) and $Ce(NO_3)_3 \cdot 6H_2O$ (Alfa Aesar 99.5%) or $Eu(NO_3)_3 \cdot 6H_2O$ (Alfa Aesar 99.9%). Figure 2.6 shows the flow chart of the process. Solutions were prepared stoichiometricly to form 1% doped YAG samples. The salt solution was added dropwise upon the fastly stirred 0.45 M NH_5SO_4 solution. Precipitation pH was set to 9.2 with the addition of 13.4 M NH_3 solution. After that precipitated sample was left for ageing 1h and precipitate was washed and centrifuged with distilled water and ethanol until the pH level returned around 7. Washed precipitate was dried at 90˚C for 24h and grinded via mortar and pestle. Powder obtained was calcined at various temperatures between 900-1300˚C to obtain the garnet phase with particle size around 100nm and crystallite size around 35nm and evaporate the excess chemicals. Figure 2.7 shows the schematic representation of reverse-strike route.

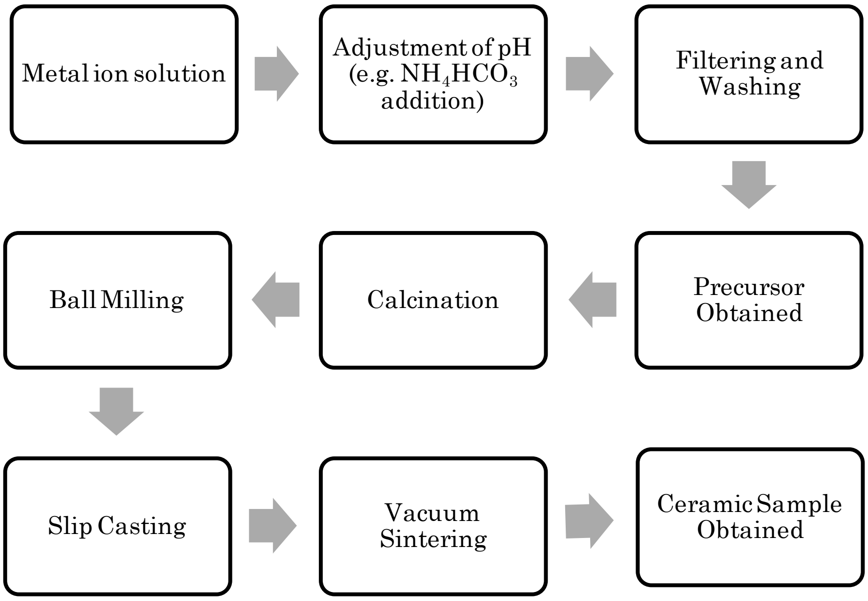

Figure 2.6 Flow chart of the reverse-strike route of the co-precipitation method.

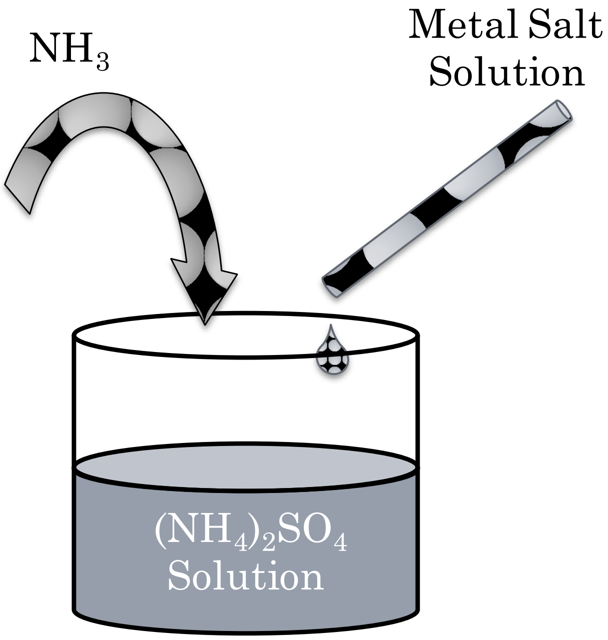

Figure 2.7 Schematic representation of the reverse-strike route of co-precipitation method.

2.2.1.5 Green Body Forming

With the addition of distilled water as the milling media, polyethylene glycol (PEG) (Sigma Aldrich 200MW) as the binder, dolapix as the dispersant powders, slurries with 20% solid content were formed. The ratio of PEG was 0.5 wt% and ratios of dolapix (Eurokimya) 2 wt% with respect to the solid content. Different amounts of tetraethoxysilane (TEOS) (Alfa Aesar 99.99%) added to YAG powders to achieve 0.2, 0.28, 0.35 wt% SiO_2 in the end product. Slurry batches ball milled for 20h using 5mm diameter, high purity ZrO_2 balls in polyethylene jars. Having ball milled slurries were poured into plaster of paris molds and kept in the molds until the green bodies were dry enough to be unmolded. Plasters molds were prepared with 1.7 plaster to water ratio. Organics were removed via heat treating the samples at 3˚C/min heating rate to 600˚C and kept for 6h.

2.2.1.6 Sintering

Samples sintered at 1700^{o}C under 3x10^{-5} torr vacuum in tungsten mesh heated vacuum furnace (Centorr Vacuum Industries, LS series). Samples were sintered for 8, 24 and

30h to examine the effect of the sintering time. The heating rate was 10˚C/min while the cooling rate was 20˚C/min.

2.2.1.7 Characterization

Characterization of thermal properties of powder samples were performed by thermogravimetry (Seiko Exstar TG/DTA 6300). Samples, under constant air flow, were heated at 10˚C/min to 1100˚C. Phase identification and structural properties were investigated via XRD (X-ray diffraction analysis, Bruker D2 Phaser). Measurements were performed between $10^\circ < 2\theta < 75^\circ$ range at room temperature. FESEM (Field emission scanning electron microscope, Zeiss Ultra) samples were prepared as 1mg samples were dispersed in 1ml ethanol and exposed to ultrasonic vibration. After drying, FESEM images were taken to examine the micro structures of powder samples.

2.3 Results and Disscussion

2.3.1 Thermogravimetric Anaysis and the Calcination Temperature

In this section thermogravimetric analysises of YAG precursors synthesised by different methods are compared. Calcination temperature of samples were decided according to the DTA data. Figure 2.8 shows the TGA/DTA signals between 0-1200˚C of YAG precursor from reverse-strike method, synthesised at pH 9. The figure shows that the samples went through several stages of decomposition when heated. Total mass loss through the experiment was calculated 37.8% until around 900˚C from the TGA curve. This mass loss is due to the loss of $\mathrm{H_2O}, \mathrm{NH_3}, \mathrm{OH^-}$ and $\mathrm{NO_3}^-$ groups in the sample . Endothermic peaks at 112˚C and 209˚C are assumed to be from evaporation of water and ammonia groups [87]. Exothermic peaks at 928˚C and 1035˚C are associated with YAP and YAG phase transformations respectively [88]. When the formation of YAP phase starts at 928˚C almost all of the sample decompose into oxides as mass loss is less than 1%.

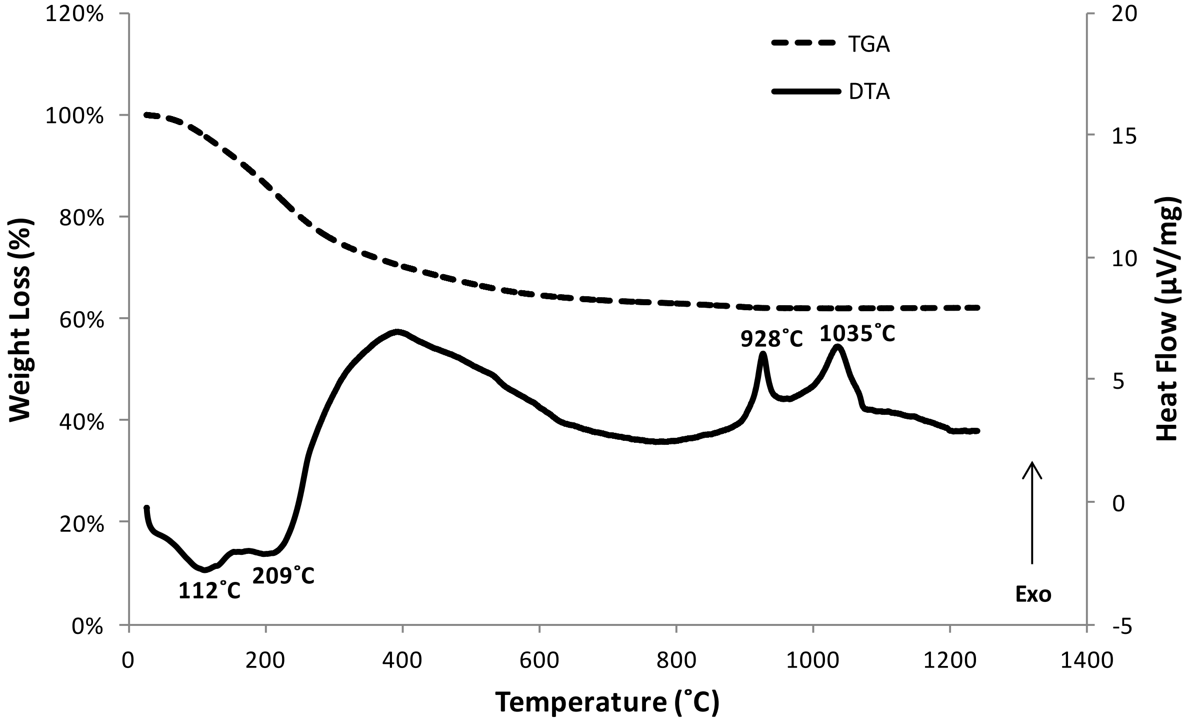

Figure 2.8 TGA/DTA signals of the YAG precursor via reverse-strike route at pH 9. Measuremets were conducted under air pressure at 10˚C/min.

Figure 2.9 shows the TGA/DTA signals between 0-1200˚C of YAG precursor from reverse-strike method, synthesised at pH 12. As the sample synthesised via reverse-strike route at pH 9, the samples at pH 12 also went through several stages of decomposition when heated. Total mass loss was calculated 24.3% until around 300˚C from the TGA curve. This loss is attributed the loss of H_2O, NH_3 and NO_3^- [88]. And sample lost 8.9% of its mass until around 900˚. This loss is attributed the decomposition of hydroxide group [89]. Endothermic peak at 201˚C are assumed to be from evaporation of water and amonia groups [87]. Exothermic peak at 929˚C indicates YAP phase transformation [88]. The peak indicates the crystallization of the YAG is missing in the sample via reverse-strike at pH 12.

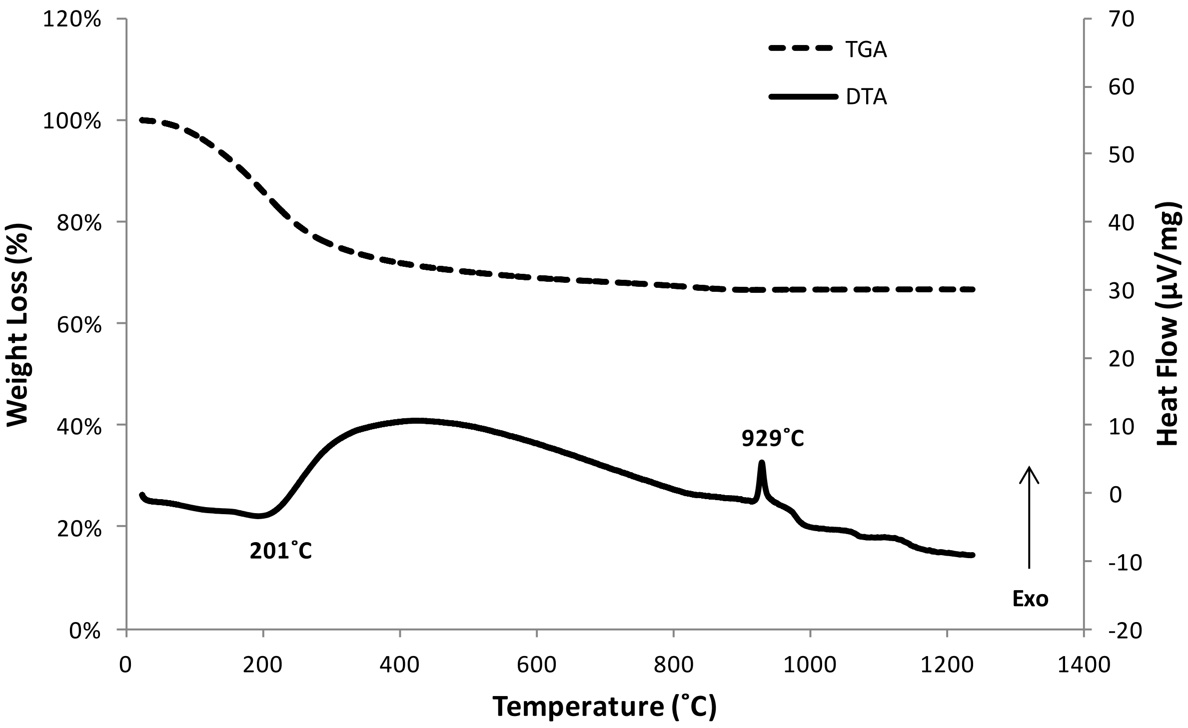

Figure 2.9 TGA/DTA signals of the YAG precursor via reverse-strike route at pH 12. Measuremets were conducted under air pressure at 10˚C/min.

Figure 2.10 shows the TGA/DTA signals between 0-1200˚C of YAG precursor from hydrothermal method with urea at 90˚C. Total mass loss through the experiment was calculated 42.8% until around 900˚C. This mass loss is higher that the samples from the reverse-strike route. The mass loss is attributed to the decomposition of H_2O, OH^- and NO_3^- groups in the sample. Endothermic peak at 104˚C is due to the evaporation of water and ammonia groups [87]. YAP and YAG phase transitions have their characteristic exothermic peaks at 924˚C and 1045˚C respectively [88]. There is an exothermic peak at 458˚C in the hydrothermal route samle. This peak is attirbuted to the decomposition of urea [90].

TGA/DTA signals from the precursors via normal-strike route between pH 2.2 and 11 is shown in figure 2.11. Mass loss calculated 36.5% up until 900˚C because of the decomposition of H_2O, NH_3, OH^- and NO_3^- groups. Endothermic peaks are present at 96˚C and 184˚C indicates evaporation of water and amonia groups [87]. Phase transition peaks are visible at 932˚C and 1016˚C belong to YAP and YAG transitions respectively [88].

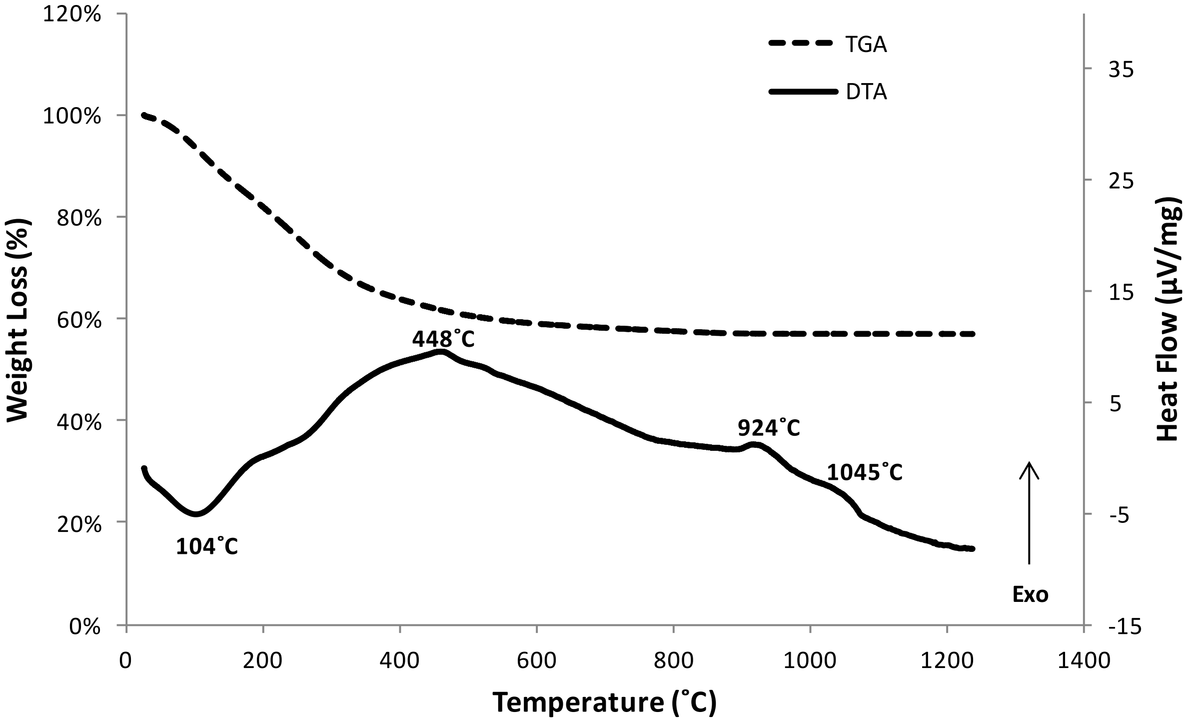

Figure 2.10 TGA/DTA signals of the YAG precursor via hydrothermal route at 95˚C with urea. Measuremets were conducted under air pressure at 10˚C/min.

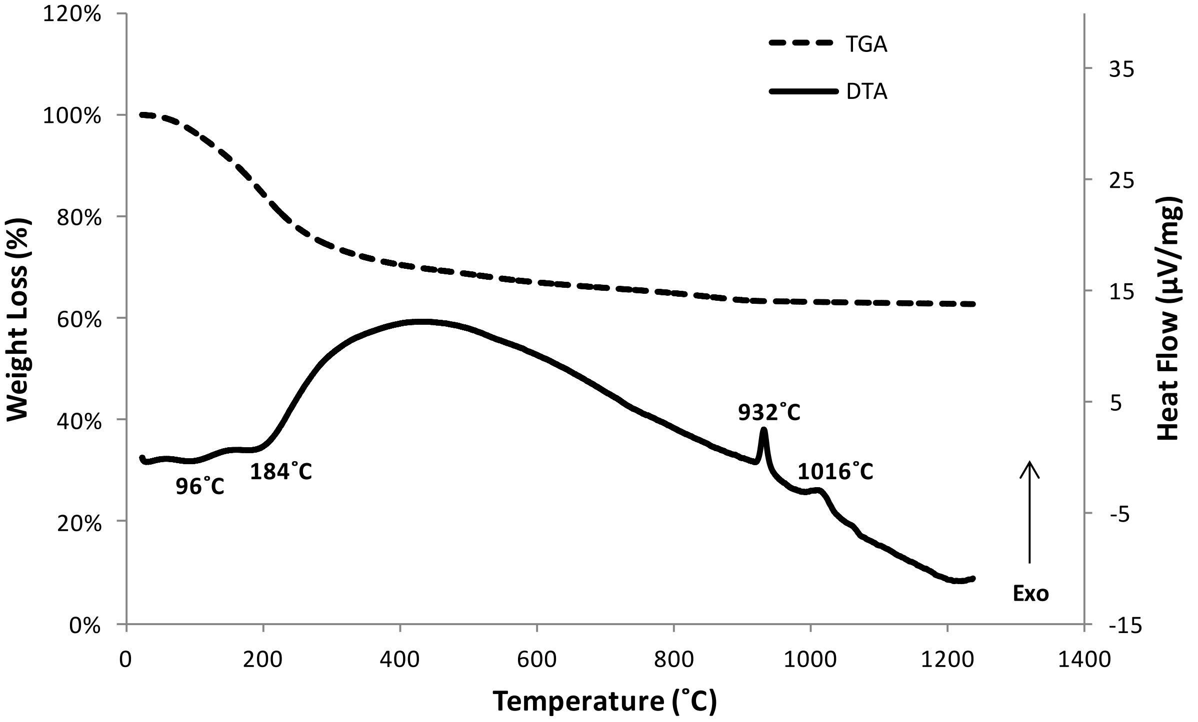

Figure 2.11 TGA/DTA signals of the YAG precursor via normal-strike route at pH from 2.2 to 11. Measuremets were conducted under air pressure at 10˚C/min.

Figure 2.12 shows the TGA/DTA signals of the YAG precursors prepared by the citrate method. Up until 350˚C there is a 8% mass loss. This loss is attributed to the decomposition of nitrate groups and the moisture absorbed during the heat treatment at 300˚C [87, 91]. The sample lost 31.5% of its total mass between 350˚C and 600˚C along with a sharp DTA peak at 434˚C. The sharp peak indicates the decomposition of metal chelates and the loss can be attributed to the decomposition and combustion of the polymeric resin [91]. The remaining mass loss may be due to the loss of the carbon atoms intermingling with metal oxides [92]. There are the very weak exothermic peaks at the 886˚C 937˚C and 1047˚C. XRD at figure 2.26 shows that the citrate route sample contains only YAG phase at 900˚C. Considering that the exothermic peak at 886˚C is attributed the YAG crystallization. The exothermal peaks at 937˚C and 1047˚C are from the oxidation of residual carbon [93].

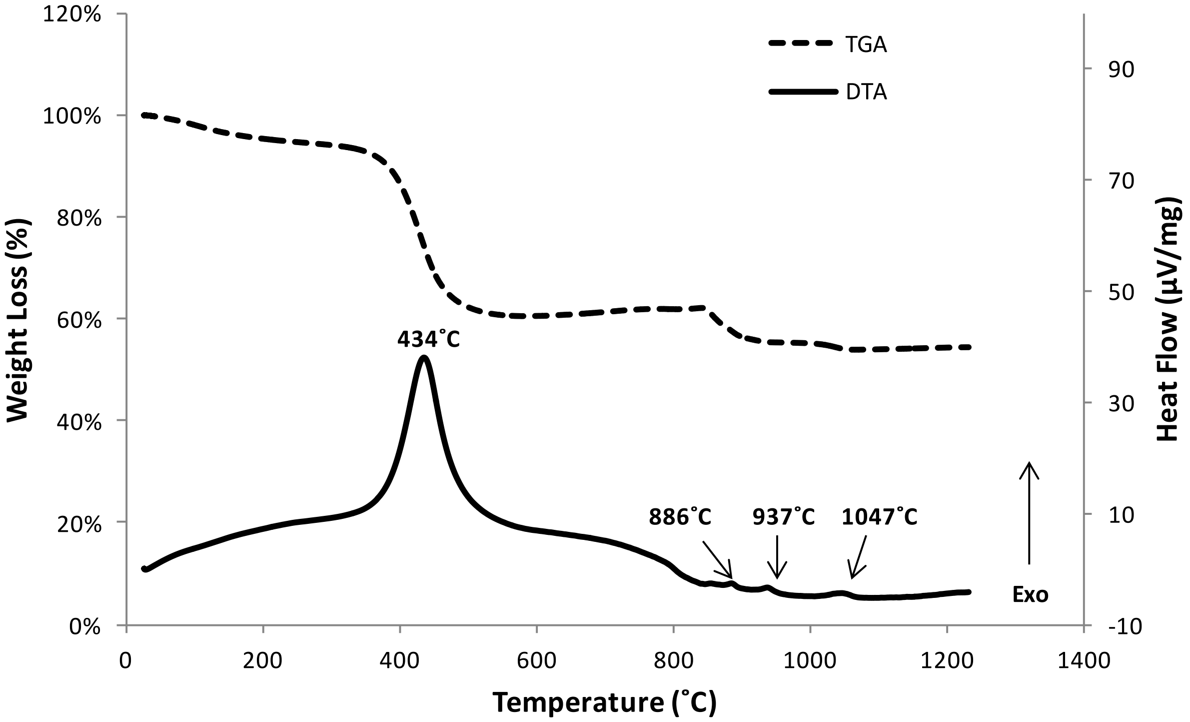

Figure 2.12 TGA/DTA signals of the YAG precursor via citrate method. Measuremets were conducted under air pressure at 10˚C/min.

Considering the TGA/DTA data of the different methods, YAG phase transition peaks are very weak in normal-strike and reverse-strike at pH 12 samples while YAP phase transition peaks are strong. This may indicate the YAG phase transition is transforming from the intermediate phases such as YAM and YAP [94]. XRD data in Figure 2.24 and 2.25 agrees with the TGA/DTA results. When calcined, samples of normal-strike and reverse-strike at pH 12 contains YAP and YAM even above the YAG phase transition temperature, 1016˚C. However, in reverse-strike at pH 9 sample YAG phase transition peak is very strong. As it is seen at the Figure 2.15, XRD patterns of reverse-strike at pH 9 samples do not contain any YAM or YAP phase when heat treated above 1100˚C. This indicates that most of the YAG phase forms from amorphous phases [94]. On the contrary, below the 1035˚C, the temperature the YAG crystallization starts, reverse-strike route sample still contains pure YAG phase. One study shows that the exothermic peak respective to the crystallization often lags behind the actual crystallization temperature because of the hysteresis of the temperature [95].

For the hydrothermal route sample and citrate sample both phase transition peaks are very faint. In Figure 2.24 and 2.25 hydrothermal route sample contains both YAP and YAG phases with no trace of YAM and YAP/YAG ratio is decreasing with the increasing temperature. However from the figure 2.20, it is clear that at the 900˚C pure YAG phase is obtained via citrate method and crystallization of YAG starts as low as 886˚C.

In citrate method endothermic decomposition peaks of water is missing despite the presence decrease in the TGA data corresponds to the loss of water. Decrease in the TGA is attributed to the loss of evaporation of the moisture during the final stage of the synthesis at 300˚C rather than the decomposition of the water [92].

2.3.2 Effect of the Temperature in Normal Strike Co-Precipitation

The X-ray diffraction patterns of the co-precipitated samples via normal strike method that are heat treated for 8h at three different temperatures between 1100˚and 1300˚C are shown in Figure 2.13. Along with characteristic YAG peaks there are also peaks of intermediate phases, YAP and YAM. In the sample calcined at 1100˚C, thirteen of the characteristic garnet phase peaks are visible at $2\theta = 18^\circ, 27.7^\circ, 29.6^\circ, 33.2^\circ, 36.6^\circ, 38.2^\circ, 41^\circ, 42.4^\circ, 46.5^\circ, 52.6^\circ, 54.8^\circ, 56^\circ$ and 57.1° along with a monoclinitic YAM phase peak at $2\theta = 30.7^\circ$. Crystallite size is calculated from the main peak and for the sample calcined at 1100˚C, it is 25.7nm. With the increasing temperature, two new characteristic YAG peaks at $2\theta = 20.9^\circ$ and 51.4° are emerged along with a new YAM phase peak at $2\theta = 18.9^\circ$ in the sample that calcined at 1200˚C. Crystallite size in this sample is calculated 27.2nm from the main peak. In the sample calcined at 1300˚C three new YAM peaks are present at $2\theta = 26.9^\circ, 44^\circ$, 49.1° and 50° and are accompanied by one YAP phase peak at $2\theta = 34.2^\circ$. Crystallite size of the sample at 1300˚C is calculated 31.3nm.

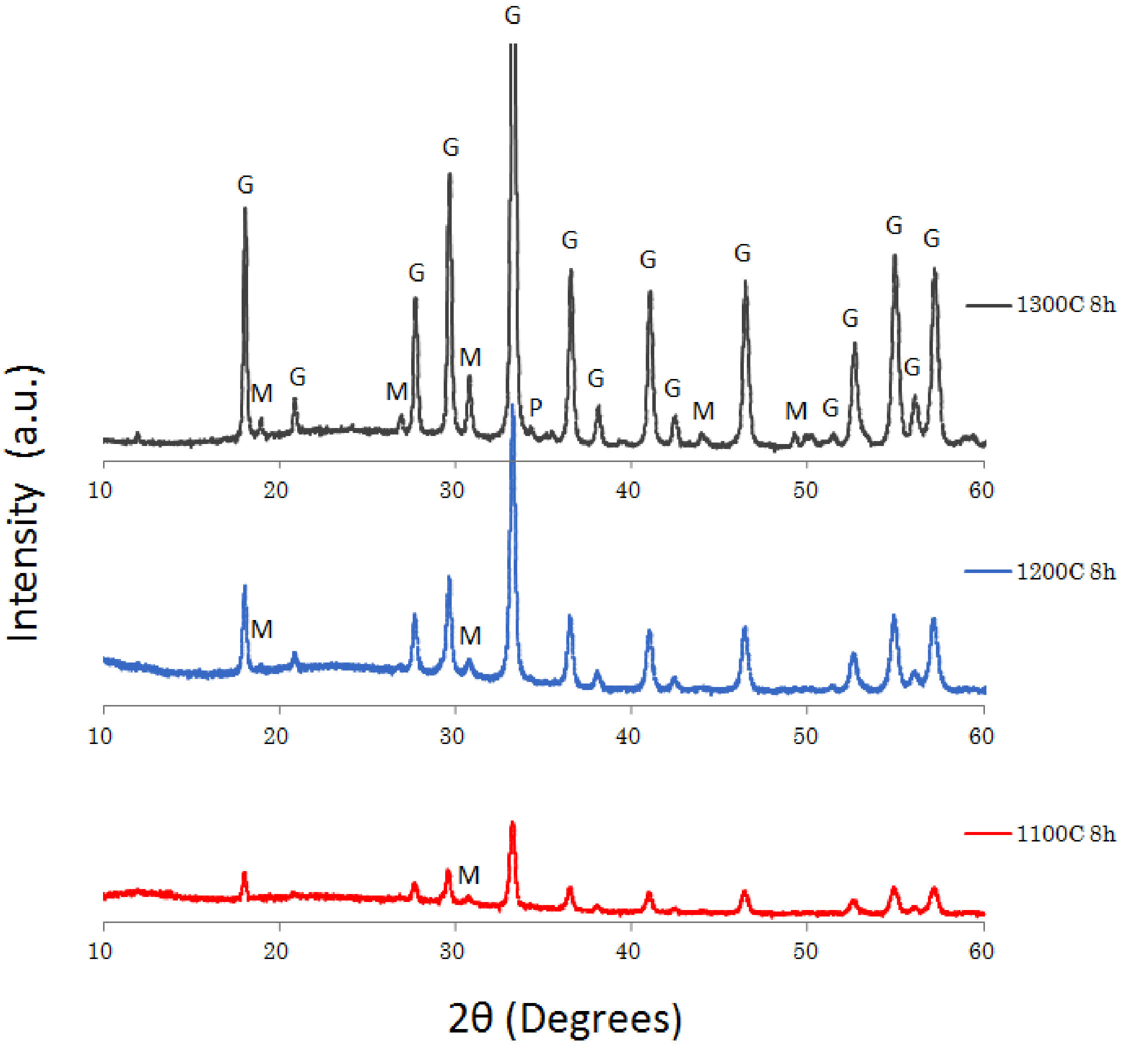

Figure 2.13 XRD patterns of the samples from normal-strike route calcined at different temperature. G, P and M stand for YAG, YAP and YAM phases respectively.

For YAG, main peak at the $2\theta = 33.35^\circ$ is the strongest peak of the cubic YAG structure and correnponds to the plane with Miller indices of $\{420\}$. However main peak of the samples calcined at all three temperatures are at 33.2˚. This slight shift indicates our samples have higher lattice parameters than the undoped YAG samples [96]. Nd^{3+}changes the lattice parameters by generating lattice stress because the ionic raius of Nd^{3+} is higher than the ionic raius of Y^{3+} [97].

With the increasing temperature crystallite size becomes higher in the samples. This behaviour can be attributed to increasing crystallization with increasing temperature. X-ray differaction patterns of the three sample also shows that YAM and phase is present in all samples but YAP phase starts to crystallize at around 1300˚C. As it is explained in the first chapter, YAG, YAP and YAM are three different crystal phases of $\mathrm{Y_2O_3}$ - $\mathrm{Al_2O_3}$ system. The reactions betwee these three phases are as:

$$\mathbf{Y_2O_3 + Al_2O_3 \rightarrow YAM + Al_2O_3 \rightarrow YAP + Al_2O_3 \rightarrow YAG} \qquad (\mathbf{2.1})$$

Figure 2.14 shows ratios of crystalline phases in the sample versus calcination temperatures that are calculated from XRD data. Figure shows that YAM phase is turning into YAP phase with the increasing temperature. And crystallization of the YAG phase is not completed at 1300˚C. Producing pure YAG single-phase have an vital effect on high luminescence efficiency [98]. However, via normal strike route several studies suggested it is very hard to achieve signle YAG phase [37]. *Glushkova et al*. explained that in normal-strike even if the Y^{3+} and Al^{3+} cations are precipitated in correct stoichometric ratios YAG phase fomed at aroun 1000˚C decomposes into other phases at higher temperatures [42].

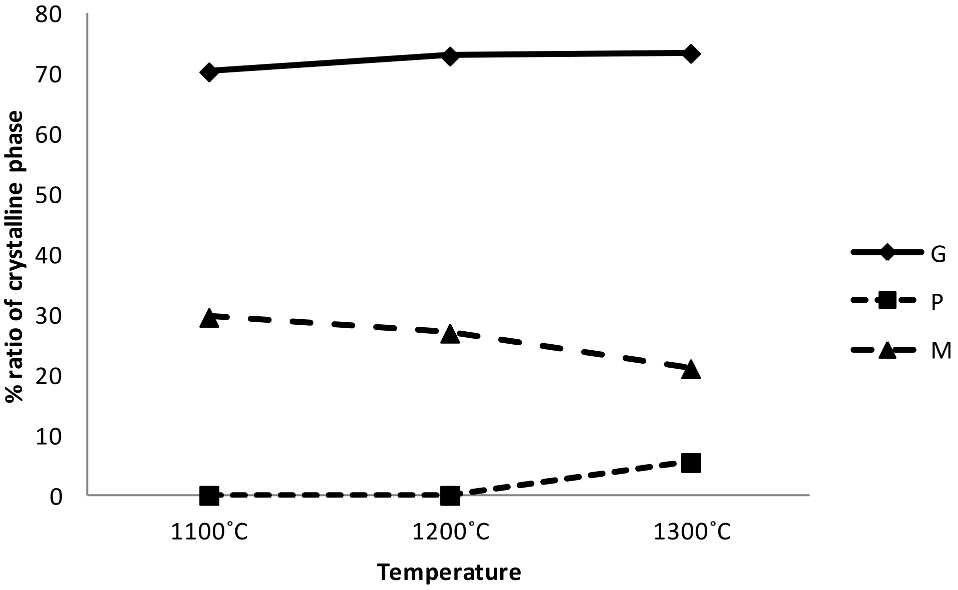

Figure 2.14 Comparison of the crystalline phases in the normal-strike sample calcined at various temperatures.

2.3.3 Effect of the Temperature in Reverse Strike Co-Precipitation

Figure 2.15 shows the X-ray diffraction patterns of the co-precipitated samples via reverse strike method that are heat treated for 8h at between 900˚C and 1200˚C. The main garnet phase peak at the $2\theta = 33.34^{\circ}$and no conciderable peak shift has been observed. Samples are crystallized with no other distich phases at 900˚C This result is not possible with the normal strike method[39] and indicates higher cation homogeneity in the samples with reverse strike method compared to the normal strike method. With the increasing calcination temperature crystallization becomes more apparent as the peaks are getting stronger. No distinctive secondary phases have been observed in samples calcined between 900˚C and 1100˚C for 8 h however, there is an unknown peak at $2\theta = 29.1^{\circ}$ which has not been reported in literature so far. Crystallite sizes are calculated 29.9nm for the sample calcined at 900˚C and 37.9 nm for the sample calcined at 1200˚C from the main garnet phase peak at the $2\theta = 33.34^{\circ}$.

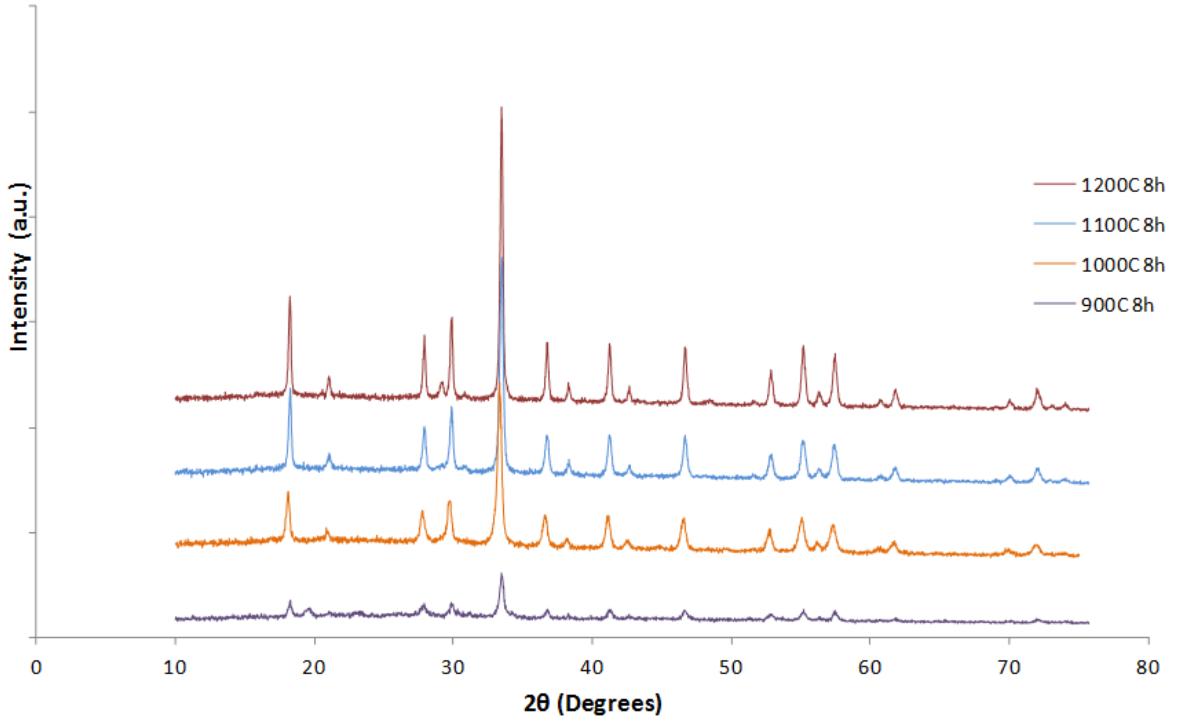

Figure 2.15 XRD patterns of samples from reverse-strike method at different temperatures.

Figure 2.16 shows the SEM images of the reverse-strike at pH 9 samples calcined at 900˚C, 1100˚C and 1200˚C for 8 hours. From the image “a” of the sample at 900˚C, crystallization has not been completed yet as distinct particles have not been formed. XRD data at figure 2.15 agrees with this result as YAG peaks are premature at 900˚C. With the increasing temperature particles become bigger. Image “b” of the sample at 1100˚C shows that the crystallization is more dominant and distinct particles are visible with higher temperatures. The image “c” shows the sample calcined at 1200˚C and grain growth is apparent in this sample compared to the image “a” and image “b”.

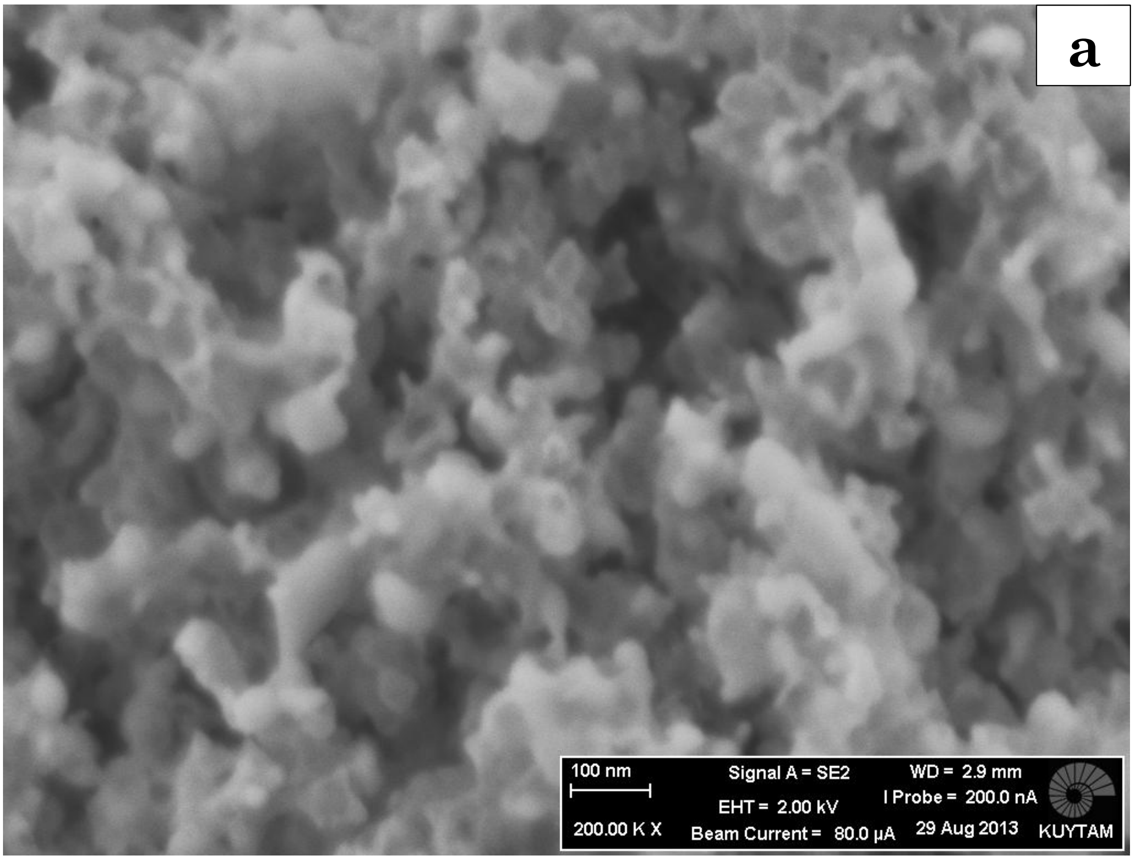
a
100 nm
200.00 K X
Signal A = SE2
EHT = 2.00 kV
Beam Current = 80.0 µA
WD = 2.9 mm
I Probe = 200.0 nA
29 Aug 2013
KUYTAM

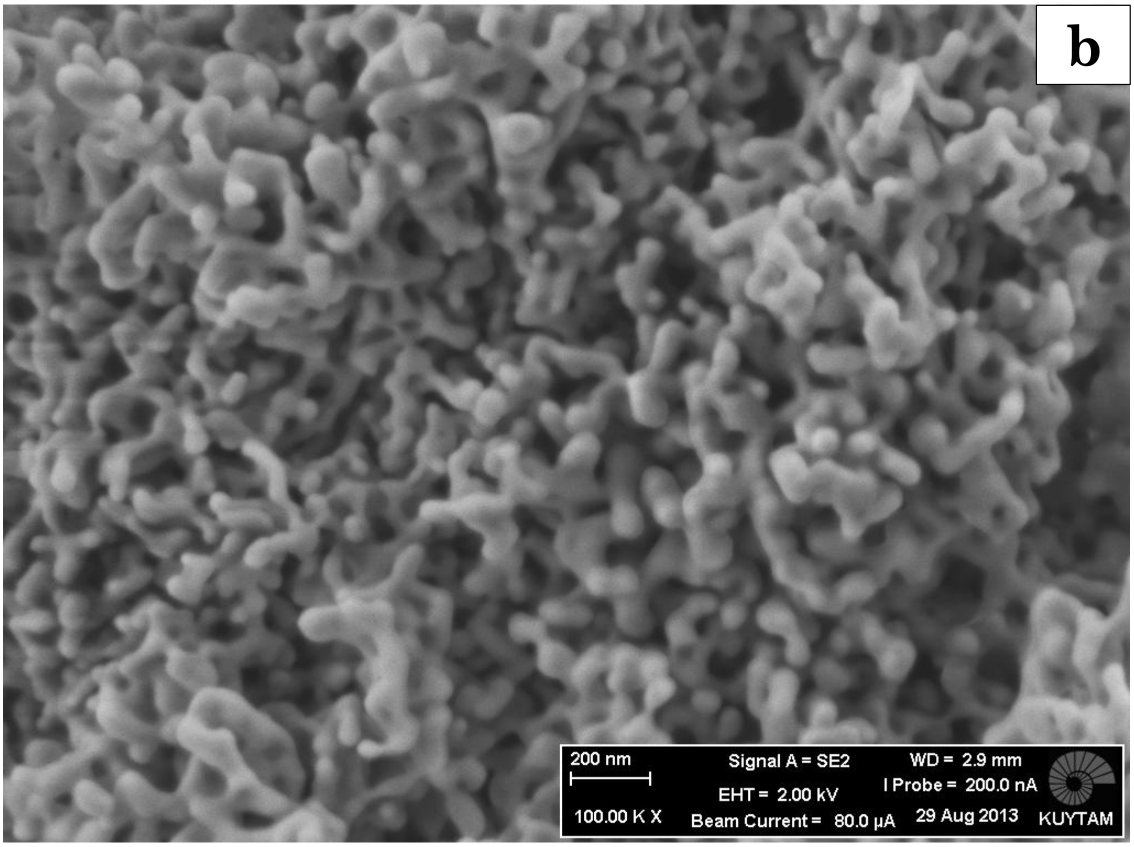
b
200 nm
100.00 K X
Signal A = SE2
EHT = 2.00 kV
Beam Current = 80.0 µA
WD = 2.9 mm
I Probe = 200.0 nA
29 Aug 2013
KUYTAM

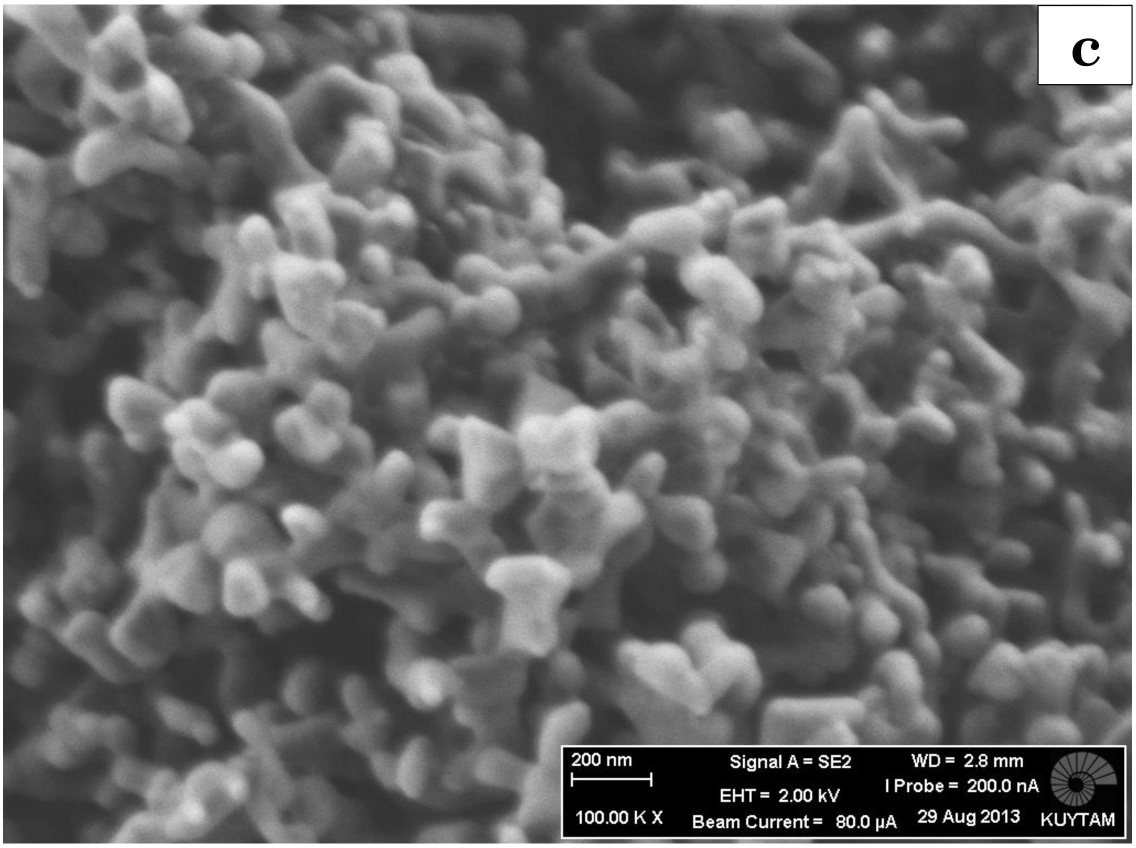

Figure 2.16 SEM images of the samples produced by reverse-strike method. Image (a) shows the sample from 900˚C while image (b) shows 1100˚C and image (c) shows 1200˚C

2.3.4 Effect of the Calcination Time and Two Step Calcination

Calcination time and how it factors grain growth investigated in this part. Figure 2.17 shows XRD patterns of Ce:YAG via co-precipitation at pH 9.2. Samples calcined at 1200˚C for 1, 8 and 12 hours. None of the samples contain only YAG phase and do not show any intermediate phase of the Y_2O_3 - Al_2O_3. However, in all samples a peak at $2\theta = 29.1^\circ$ from an unkown phase is present. Crystallite sizes are calculated 37.8nm, 37.9nm and 38nm from the XRD patterns for 1h, 8h and 12h samples respectively. Figure 2.18 shows the comparison of crystallite sizes of the Ce:YAG samples calcined at 1200˚C for 1h, 8h and 12h.

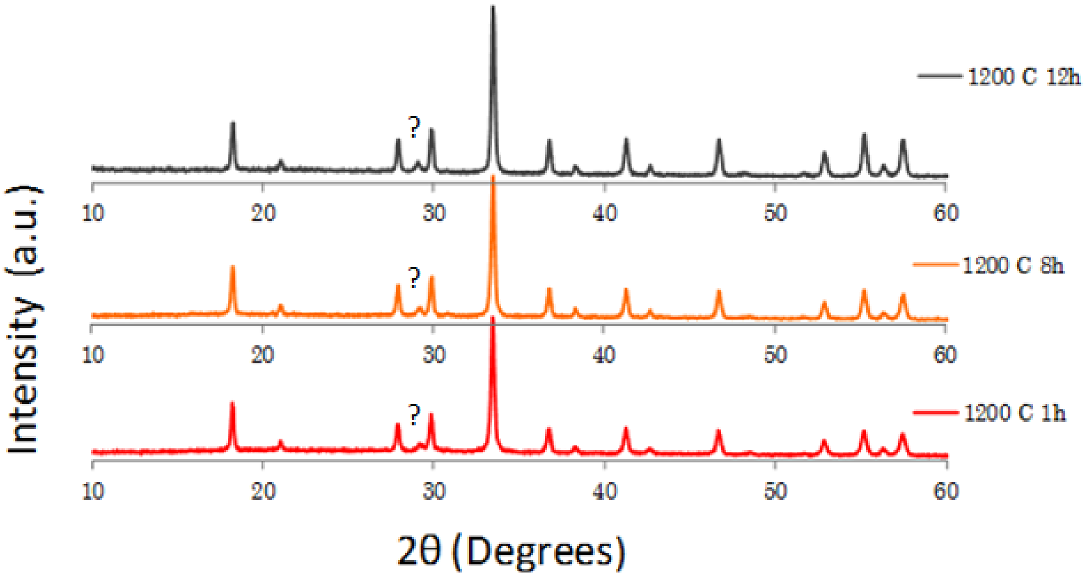

Figure 2.17 XRD patterns of Ce:YAG via reverse-strike co-precipitation calcined at 1200˚C for 1, 8 and 12 hours.

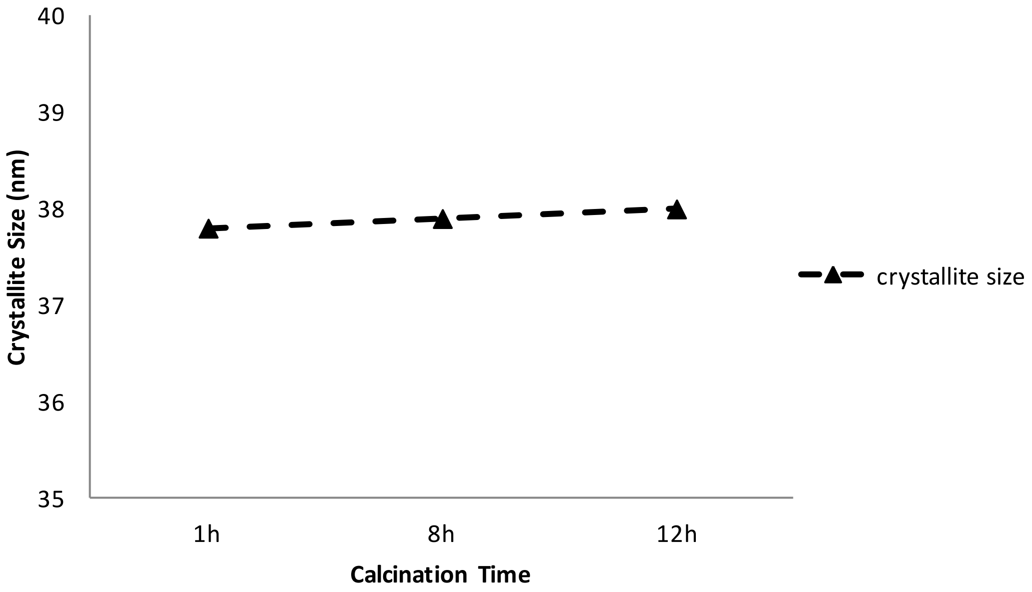

Figure 2.18 Comparison of the crystallite sizes of Ce:YAG samples calcined at 1200˚C for 1, 8 and 12 h.

Figure 2.19 shows the SEM images of the reverse-strike at pH 9 samples calcined at 1200˚C for 1, 8 and 12 hours. From the image “a” of the sample at 1200˚C for 1h, distinctive particles are visible as 1200 ˚C is above the crystallization of garnet phase seen in the DTA data in figure 2.8. XRD data from figure 2.17 also agrees crystallization has been completed at 1200˚C . From the Images at the figure 2.19, it clear that the crystallization is completed at 1200˚C as all three images show distinctive particles. Although the grain growth with increasing calcination time is apparent, it is less than the grain growth that occurs in samples from the figure 2.16.

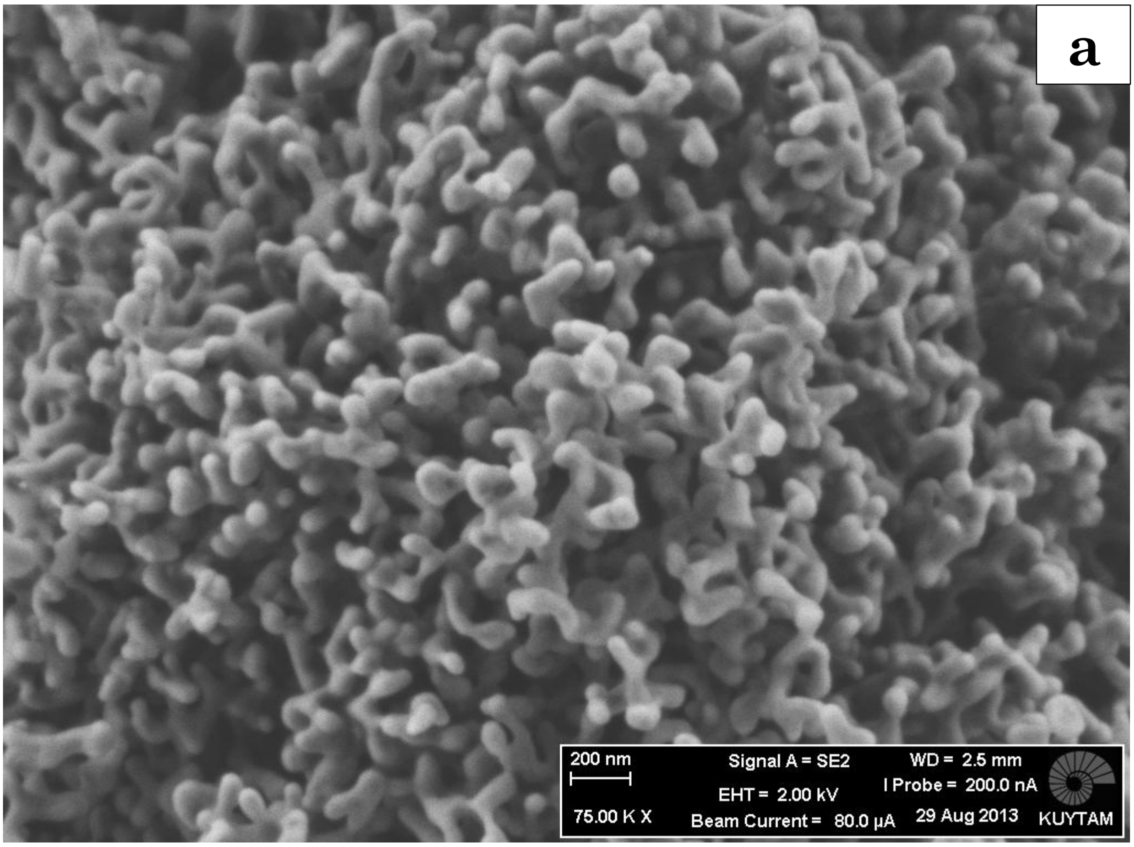

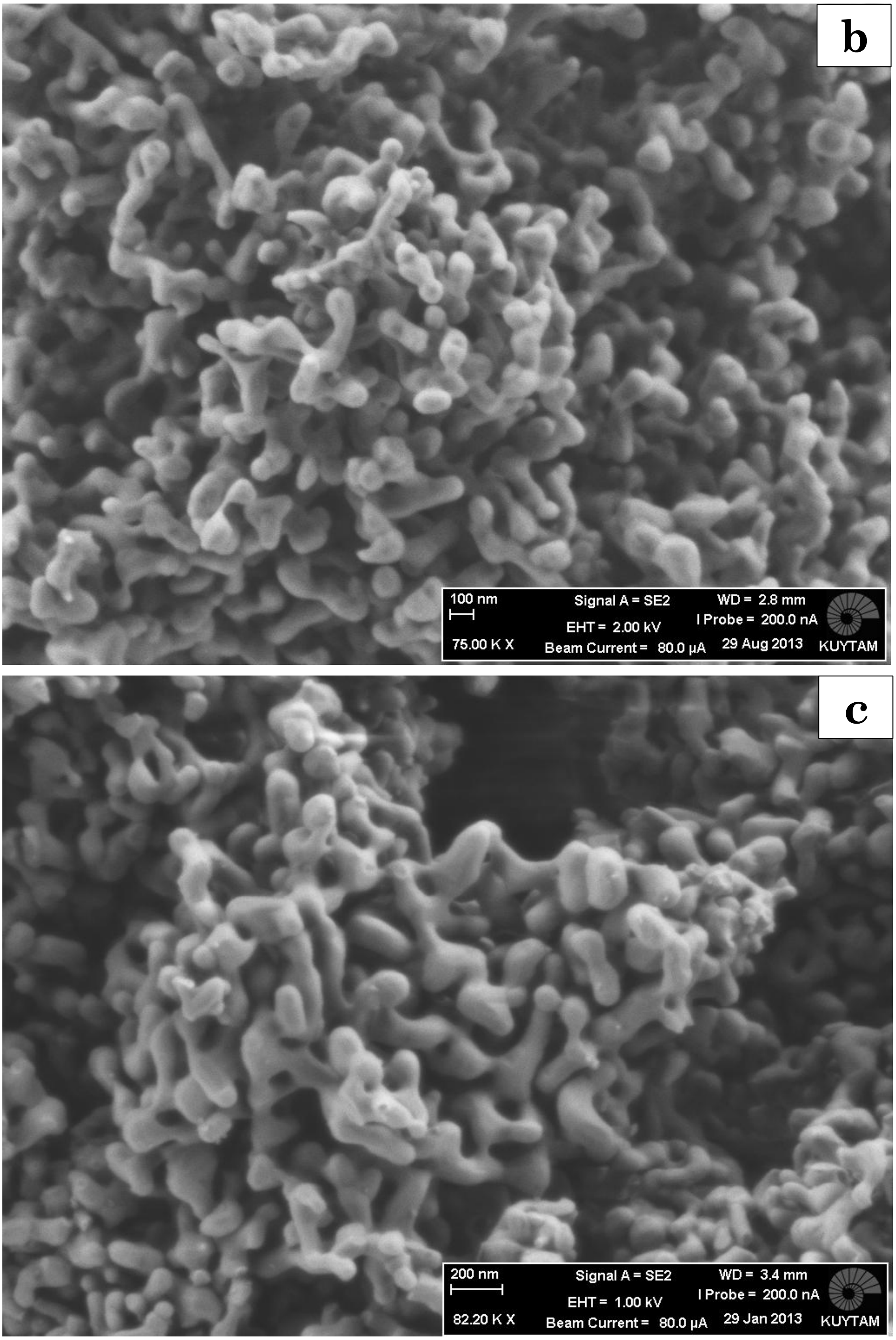

Figure 2.19 SEM images of Ce:YAG samples calcined at 1200 1h, 1200 8h, 1200 12h.

Figure 2.20 shows the XRD data from the samples produced via reverse-strike route at 9.2 pH but went through multiple step calcination. The unknown peak at $2\theta = 29.1^{\circ}$ is presistent in this sample as it is in single step calcined samples. The samples show no indication of secondary phases or any other phases of Y_2O_3 - Al_2O_3 system. The crystallite sizes are calculated from the XRD data in figure 2.20. The crtallite sizes are shown in figure 2.21. The sample calcined at 900˚C for 8h has 29.9 nm crystallites in size while the sample calcined at 900˚ for 8 h and 1200˚C for 10 h respectively has 49.6 nm crystallites. However, the three step calcination do not have efficiency of two step calcination as the sample calcined at 1200˚C for 6 h for three times has the crystallite size of 43.5 nm

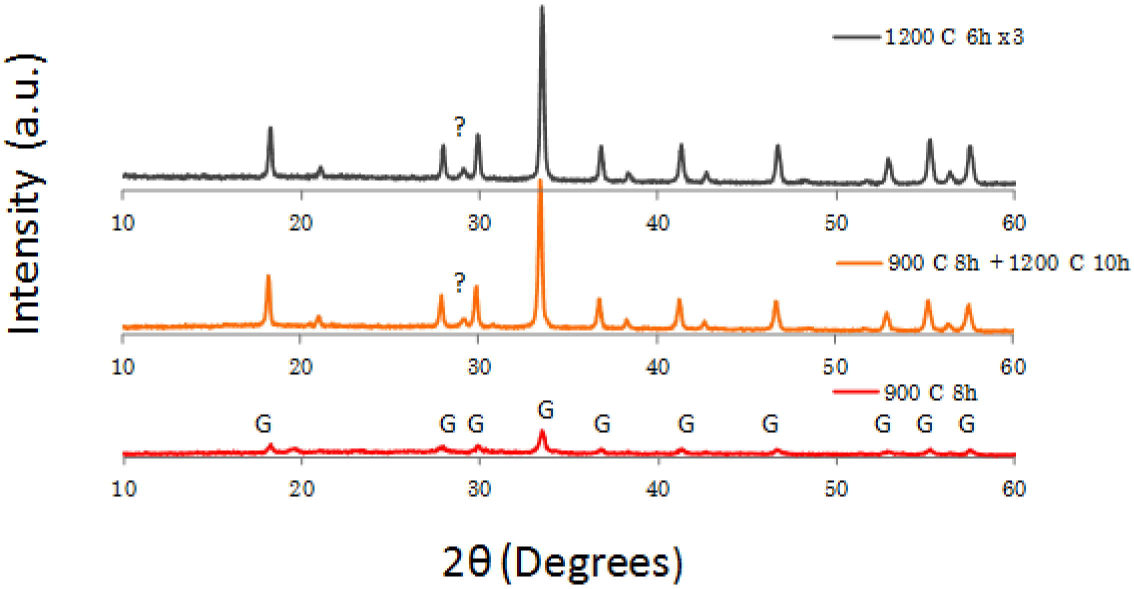

Figure 2.20 XRD patterns of Ce:YAG samples via reverse-strike co-precipitation calcined at various temperatures for multiple times. G stands for YAG phase.

The figure 2.22 shows the SEM images from the samples went through multiple step calcination. The first two images agrees with the crystallite sizes that were calculated from the XRD data. Image (a) shows the samples calcined at 900˚C for 10 h and image (b) shows the samples calcined at 900˚C for 8 h and 1200˚C 10 h respectively. The increase in particle size is clear with the additional calcination step at 1200˚C for 10h. In image (c) of the sample calcined at 1200˚C for 8h three times however shows smillar grain growth with the image (b) despite their crystallite sizes are calculated conciderably different.

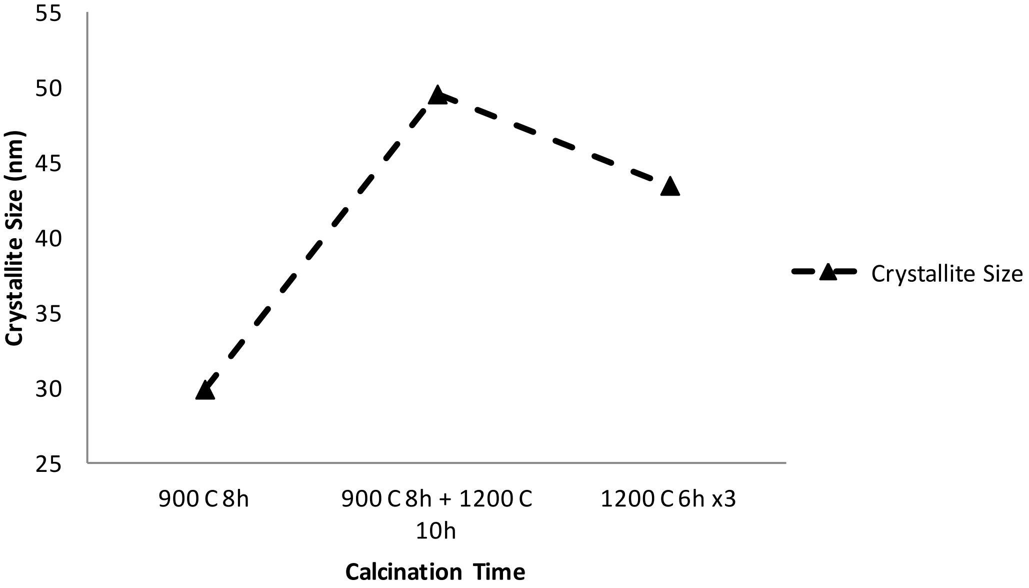

Figure 2.21 Comparison of the crystallite sizes of Ce:YAG samples calcined multiple times at 900 and 1200˚C.

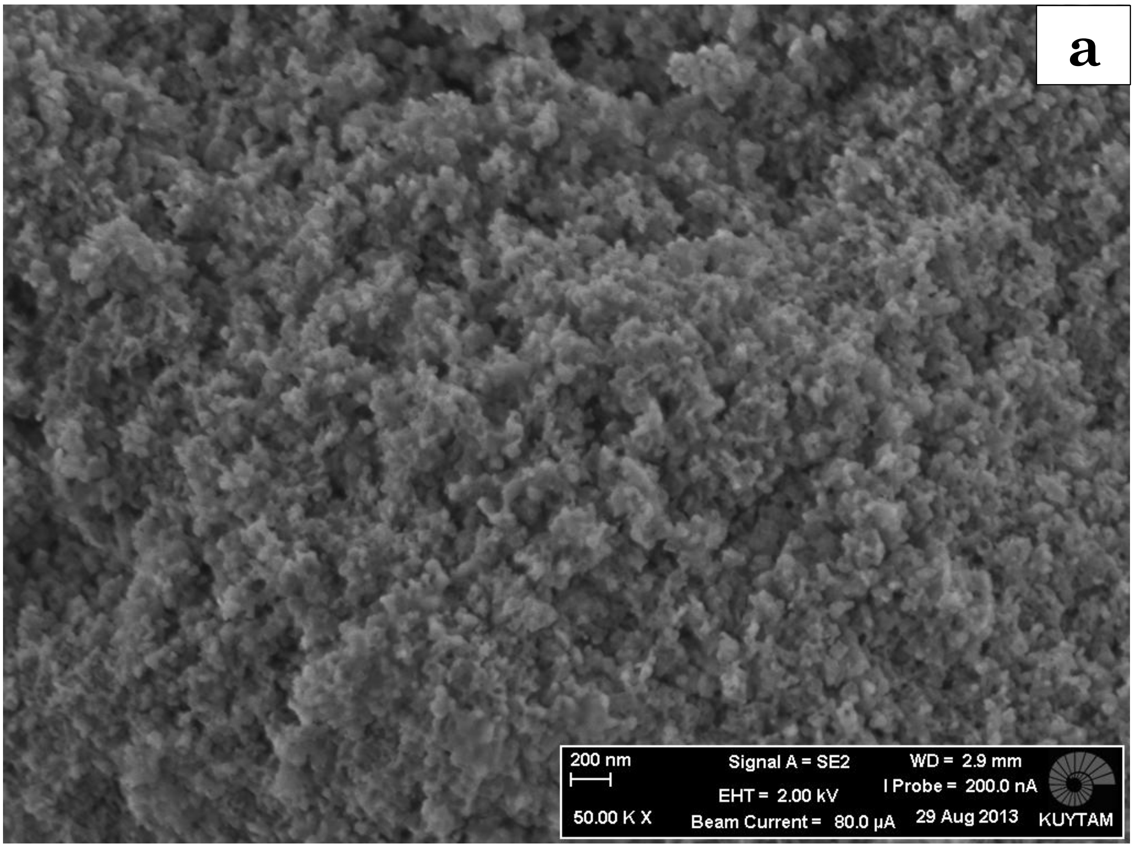
a
200 nm
50.00 K X
Signal A = SE2
EHT = 2.00 kV
Beam Current = 80.0 µA
WD = 2.9 mm
I Probe = 200.0 nA
29 Aug 2013
KUYTAM

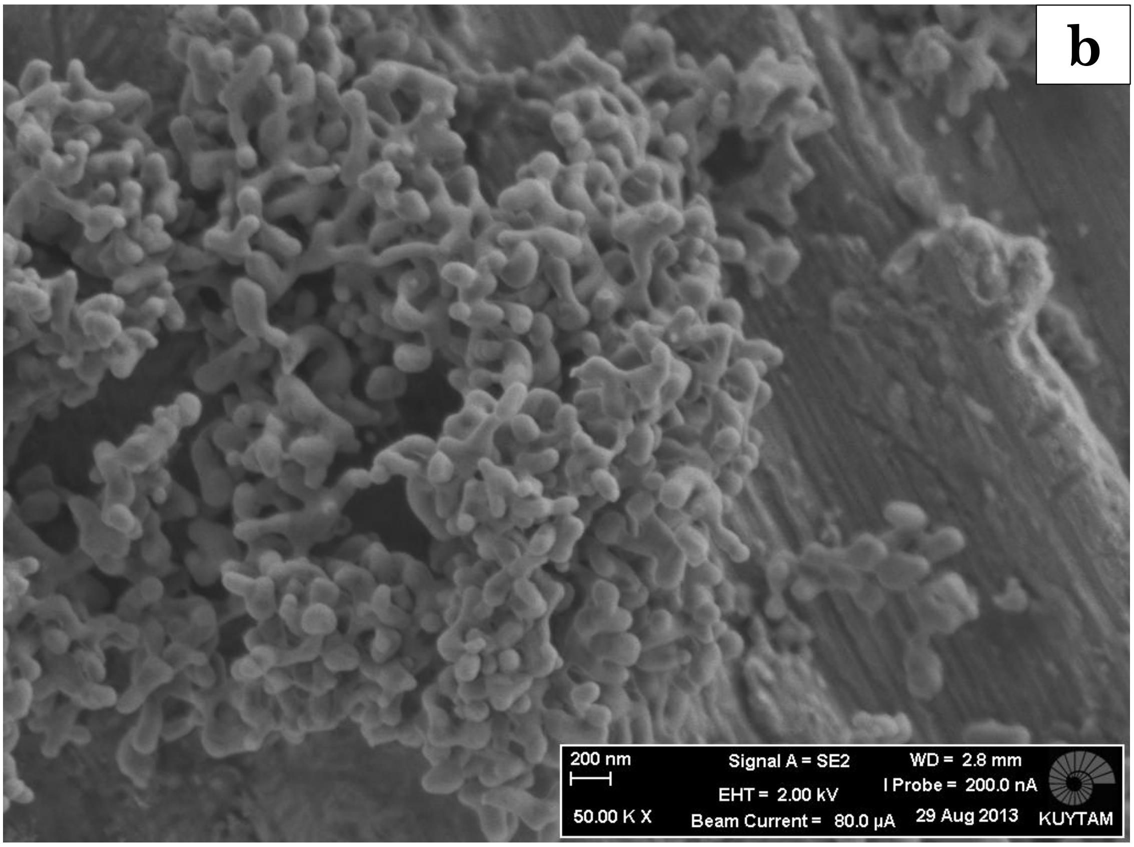
b
200 nm
50.00 K X
Signal A = SE2
EHT = 2.00 kV
Beam Current = 80.0 µA
WD = 2.8 mm
I Probe = 200.0 nA
29 Aug 2013
KUYTAM

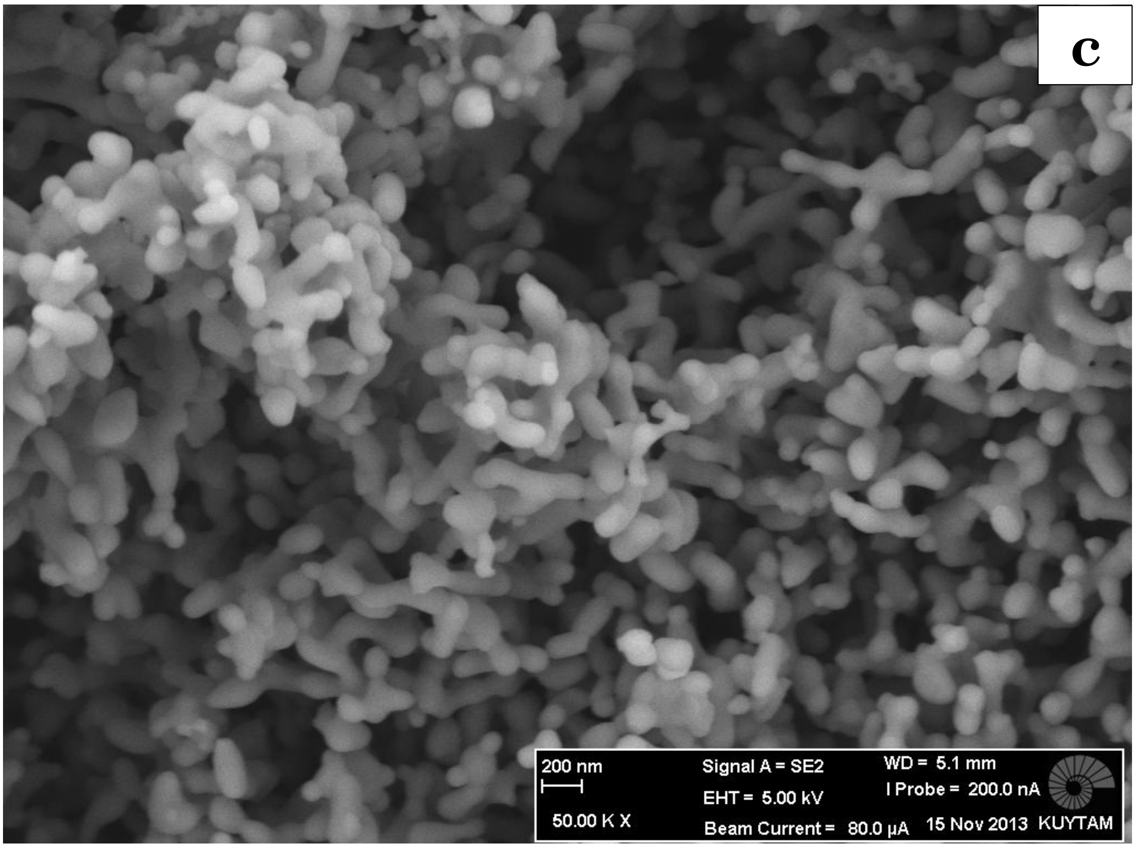

Figure 2.22 The SEM images of the samples prepared by reverse-strike route and calcined by mulitple step calcination. The image (a) is from the sample calcined at 900˚C for 8h, the image (b) is from the sample calcined at 900˚C for 8h and 1200˚C for 10h respectively and the image (c) shows the sample calcined at 1200˚C for 8h for three times.

2.3.5 Effect of pH in Reverse strike

In co-precipitation method pH has vital effect on the quality of the end product as it is a major factor in the solubility of the metallic ions. In order to control the particle size and the stoichiometry desired pH must be maintained thought the process. Figure 2.23 show the comparison of the X-ray diffraction measurements of two samples synthesized via reverse-strike co-precipitation at two different pH values 9 and 12. Samples were calcined at 1100˚C for 8. In the sample precipitated at 12 pH there are peaks from all of the ternary phases of

$Y_2O_3 - Al_2O_3$ system. YAG phase peaks are visible at $2\theta = 18^\circ, 20.8^\circ, 27.6^\circ, 29.6^\circ, 33.1^\circ, 36.4^\circ, 38.0^\circ, 40.9^\circ, 42.4^\circ, 46{,}4^\circ\ 52.5^\circ, 54.9^\circ, 56^\circ$ and 57.1°. Along with the YAG peaks there are two YAP and eleven YAM peaks are present. Crystallite size of the YAG phase is estimated 25.6nm from the main peak at the 33.1°. Similar to the samples synthesized in normal-strike route, slight negative shift is observed in the main peak compared to undoped YAG as a result of [99]. This behavior is attributed to the lattice parameter increase due to the dopant Nd^{3+} atoms with higher ionic radii than the radii of the Y^{3+} atoms they replace. The sample synthesised via reverse-strike method at pH 9 shows all of the fifteen characteristic YAG peaks between $2\theta = 10^\circ$ to $2\theta = 60^\circ$ with no other distinct phase accompanying. Main YAG peak is at $2\theta = 33.32$ thus negative shift in the main peak is less than that of the sample synthesized at 12 pH. This difference indicates that the Nd^{3+} atoms are very well dispersed in the pH 9 sample compared to the pH 12 sample as dopant atoms generate less stress in the former and cause less peak displacement [100]. Crystallite size is estimated as 29.2nm from the main peak at $2\theta = 33.32$. Better crystallization achieved in pH 9 sample.

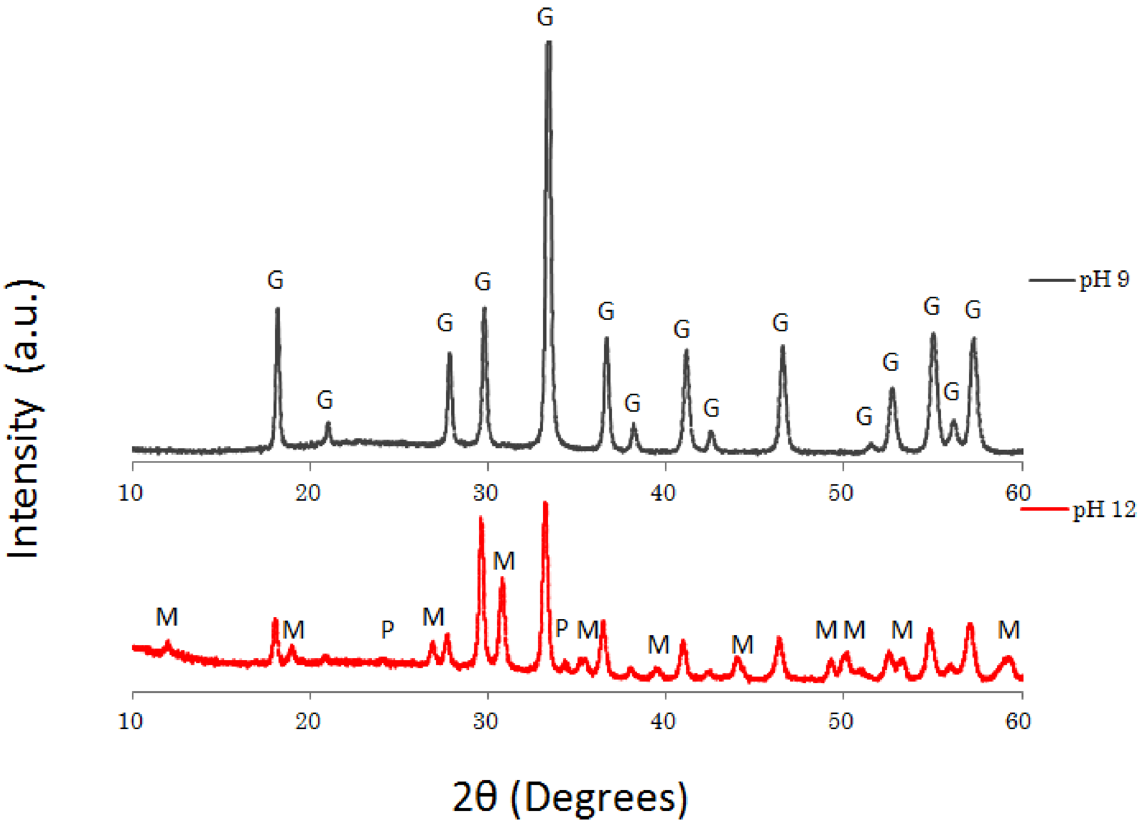

Figure 2.23 XRD patterns of Nd:YAG samples via reverse-strike method. The pattern at the below shows the samples synthesized at pH 12 while the above pattern shows the samples synthesized at pH 9. G, P and M stand for YAG, YAP and YAM phases respectively.

pH is important in reverse strike route because at pH levels below 9, not all Y^{3+} cations are precipitated effectively from the solution. At pH level 12 solubilty of cations are very low to form precursor for calcination that can grow and crystallize desirably [37]. In comparison of two samples, pH 9 sample is superior to the pH 12 in every aspect including having pure garnet phase, better crystallization and better dopant dispersion.

2.3.6 Comparison of Co-Precipitation Methods

Figure 2.24 shows the comparison of the XRD patterns of the samples that are synthesized by three different co-precipitation routes: reverse-strike, hydrothermal and normal strike. All samples are calcined at 1100˚C for 8h. In hydrothermal route urea (CH_4N_2O) was used as precipitant despite NH_3 in reverse-strike and normal-strike routes. The XRD pattern of the sample synthesized via hydrothermal route shows all fifteen characteristic YAG peaks as well as YAM peaks.

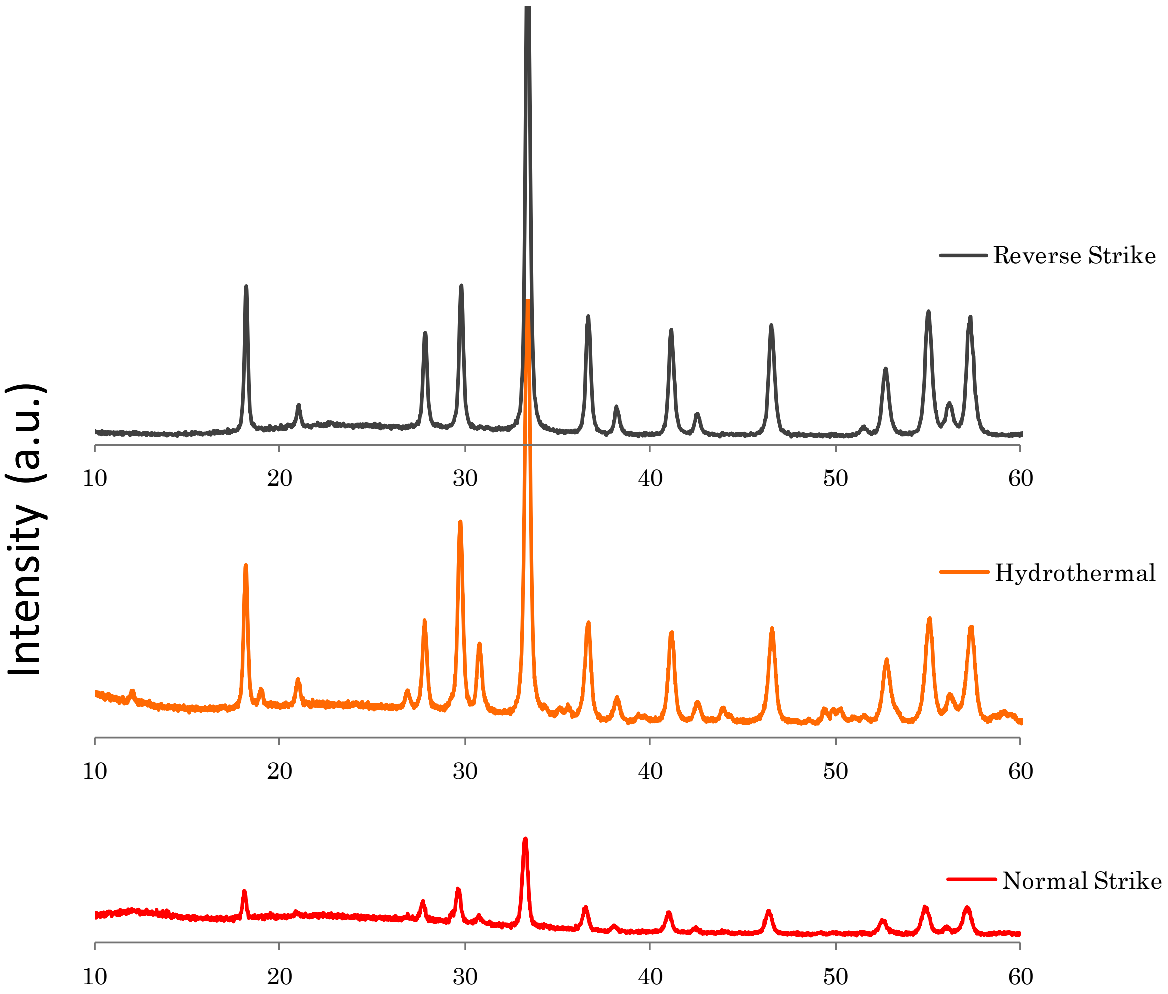

Figure 2.24 XRD patterns of Nd:YAG samples synthesized via different co-precipitation routes. All samples were calcined at 1100˚C for 8h.

Very strong YAM peaks are visible at $2\theta = 11.96^\circ$, 18.93°, 26.84°, 30.76°, 49.36°, 49.86° and 50.23°. The main YAG peak is at $2\theta = 33.31^\circ$ which is almost the same as undoped YAG samples [99]. Crystallite size of the YAG phase is calculated as 25.8nm from the main peak. No trace of YAP or Y_2O_3, Al_2O_3 peaks are encountered in the XRD pattern of the sample via hydrothermal route.

The sample synthesised via reverse-strike route is pure YAG phase with no trace of any other distinct phases. The main peak is at the $2\theta = 33.32^\circ$ and crystallite size calculated 29.2nm. In the sample via normal-strike thirteen garnet peaks are at $2\theta = 18^\circ, 27.7^\circ, 29.6^\circ, 33.2^\circ, 36.6^\circ, 38.2^\circ, 41^\circ, 42.4^\circ, 46.5^\circ, 52.6^\circ, 54.8^\circ, 56^\circ \text{ and } 57.1^\circ$ along with a monoclinitic YAM phase peak at $2\theta = 30.7^\circ$. The main peak is at $2\theta = 33.2^\circ$ and crystallite size of the YAG phase is calculated as 25.7nm.

Figure 2.25 shows ratios of crystalline phases in samples via normal-strike and hydrothermal route versus calcination temperature. The ratios are calculated from XRD data. In normal strike route, the YAM phase is present in all temperatures but decreases with increasing temperature. YAG phase increases between 1100˚C and 1200˚C however that increase is not present between 1200˚C and 1300˚C. In hydrothermal route YAG phase increases while YAM phase decreases with increasing temperature. YAP phase is not present in samples via hydrothermal route. It is mentioned above in this chapter, in reverse-strike method garnet phase is the only phase present in the sample even at relatively low calcination temperatures as 900˚C.

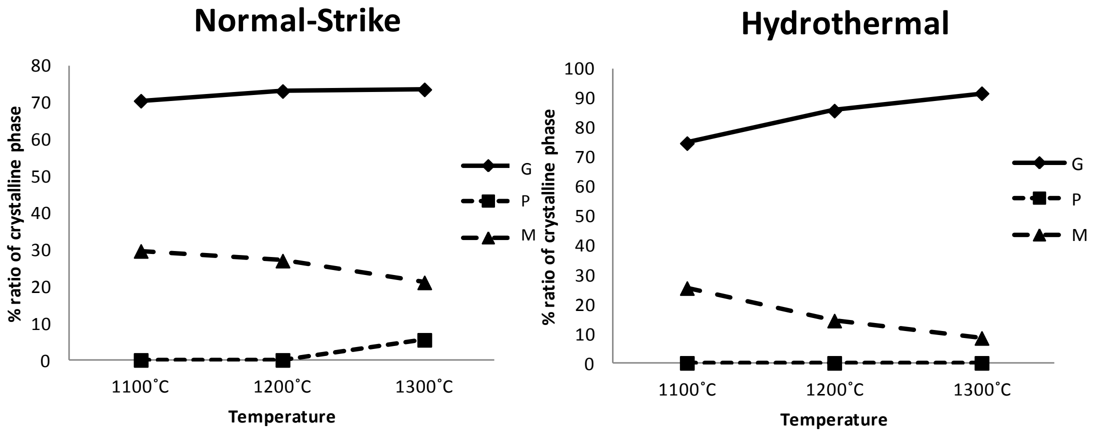

Figure 2.25 Comparison of crystalline phases in Nd:YAG samples synthesized by normal-strike route versus hydrothermal route.

In normal strike method, the precipitation is heterogenous and occurs locally in the region where the local pH is high after the addition of NH_3 drops.Different solubilities of yttrium and aluminium ions cause non-homogeneous precipitates. Therefore, the stoichiometric amount in the powder precursors cannot be maintained during the co-precipitation process. This change in stoichiometry results in the formation of other phases even if the initial stoichiometry is calculated for YAG phase only [37]. However, reverse-strike co-precipitation method is designed to overcome the different solubility problem in multi-cation materials thus, reverse-strike method has cation homogeneity advantage [101]. Hydrothemal route used in this work could not yield single garnet phase. However Takamori and David reported to had monodisperse pure YAG samples through hydrothermal route [47].

2.3.7 Comparison of Citrate, Co-precipitation and Solid State Methods

Citrate method is an attractive approach for YAG production as it has been reported that YAG crystals could be formed at temperature even as low as 850˚C without any other secondary phase [102]. In figure 2.26 we compare the ceramic powders from different methods calcined at 900˚C for 8h. Co-precipitated sample was prepared by reverse-strike route and solid state method sample was prepared by 20 h ball miling. XRD data from the solid state method shows five characteristic peaks of Y_2O_3 at $2\theta = 20.71^\circ, 29.37^\circ, 33.97^\circ, 48.68^\circ$ and 57.69° along with five characteristic peaks of Al_2O_3 at $2\theta = 25.76^\circ, 35.34^\circ, 37.95^\circ, 43.54^\circ$ and 52.71°. One peak at $2\theta = 53.34^\circ$ is attributed to the YAM phase. This result indicates that the YAM formation is just started. In solid state method, YAG phase is formed through phase transformation of YAM to YAP and YAP to YAG [49]. The samples prepared by citrate and co-precipitation methods show the fourteen characteristic peaks no trace of any other secondary peaks. Main peak of the citrate method sample is at $2\theta = 33.27^\circ$ and main peak of the co-precipitated sample is at $2\theta = 33.44^\circ$ this may indicate that less stress is generated in citrate sample. Although citrate method is superiour due to the amotic level distribution, comparable results have been achieved through reverse strike method.

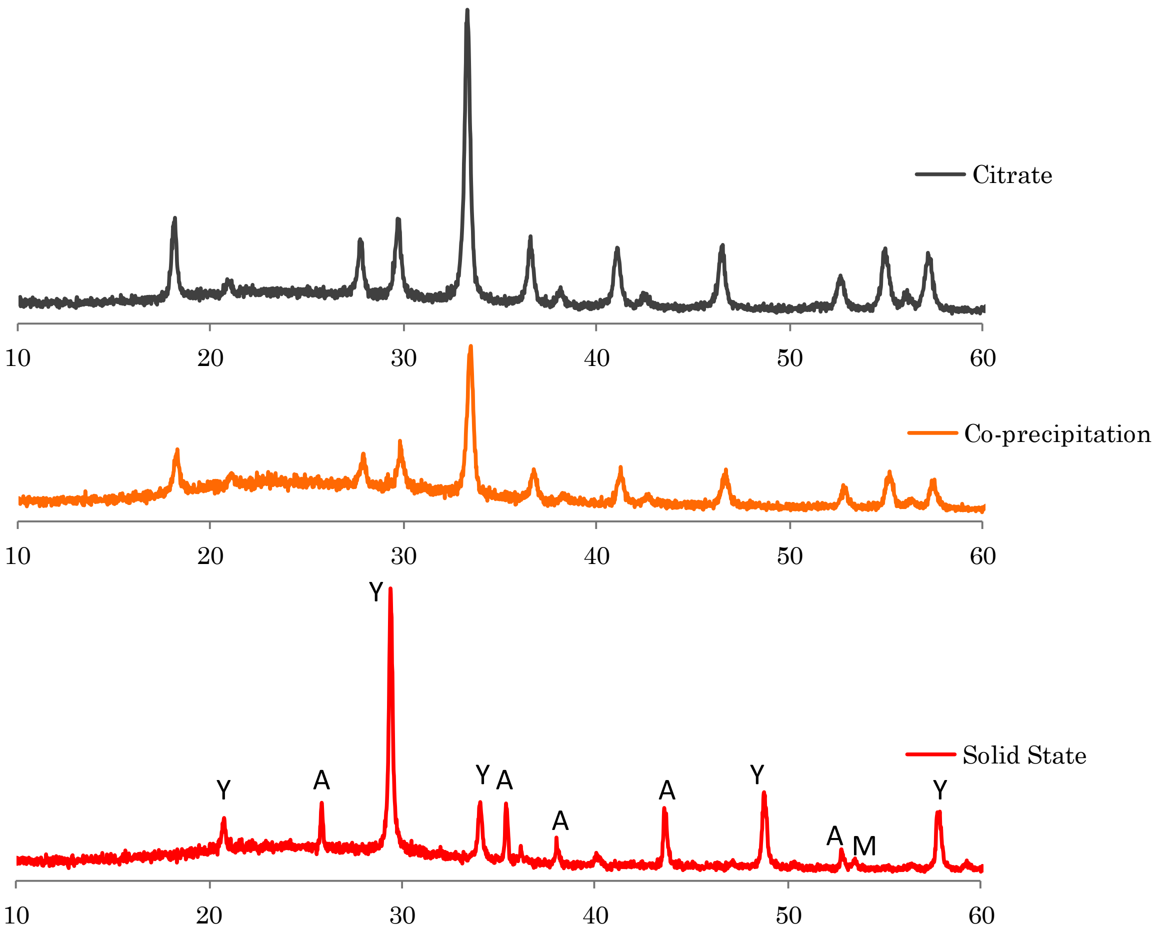

Figure 2.26 XRD patterns of samples synthesized by different methods. All samples are calcined at 900˚C for 8h. Y and A stand for Y_2O_3 and Al_2O_3 respectively.

2.3.8 Luminescent Spectra of Ce:YAG and Eu:YAG

Figure 2.27 shows the photoluminiscence data of 1 and 5% doped Ce:YAG samples prepared by reverse-strike co-precipitation. Samples were calcined at 1200˚C for 12 h. Photoluminescence measurements were performed between 480 and 800 nm. Samples were excited at 465 nm wavelength. Sample 1% shows a bump between 480 nm and 689 nm. This bump is attributed to both the$^5\mathrm{D_j} \rightarrow {}^2\mathrm{F}_{5/2}$ and $^5\mathrm{D_j} \rightarrow {}^7\mathrm{F}_{7/2}$ [103]. With the increasing dopant ratio emission peaks become stronger. However bump is shifted to the 267 nm. This may indicate that 5% dopant ratio changes the symmetry of crystal structure .

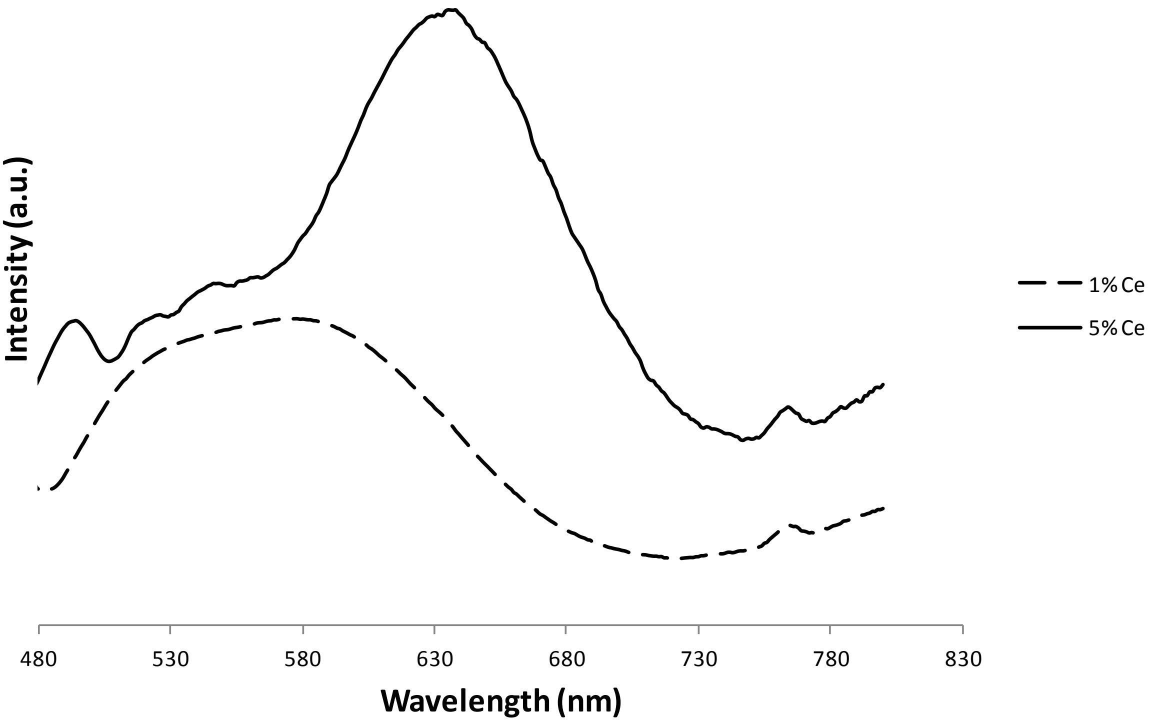

Figure 2.27 Emission spectra of 1% and 5% doped Ce:YAG samples excited at 465 nm.

Figure 2.28 shows the photoluminescence data of 0.5, 1 and 5% doped Eu:YAG samples prepared by reverse-strike co-precipitation method. Samples were calcined at 1200˚C for 12h. Photoluminescence measurements were conducted between 550 and 670 nm wavelengths. Samples are excited at 254 nm wavelength. Three peaks are present at 590, 611 and 629 nm. First peak at the 590 nm is attributed to the $^5\mathrm{D}_0 \rightarrow {}^7\mathrm{F}_1$ transition while other two peaks to the $^5D_0 \rightarrow {}^7F_2$ transition. Those peaks are characteristic emission properties of Eu^{3+} systems. The other emission peaks is at 650 nm is belongs to $^5D_0 \rightarrow {}^7F_3$ transtion [104]. From the emission spectra, Eu:YAG samples emits orange-red light. Emission intensity is stronger in with the increasing dopant ratios.

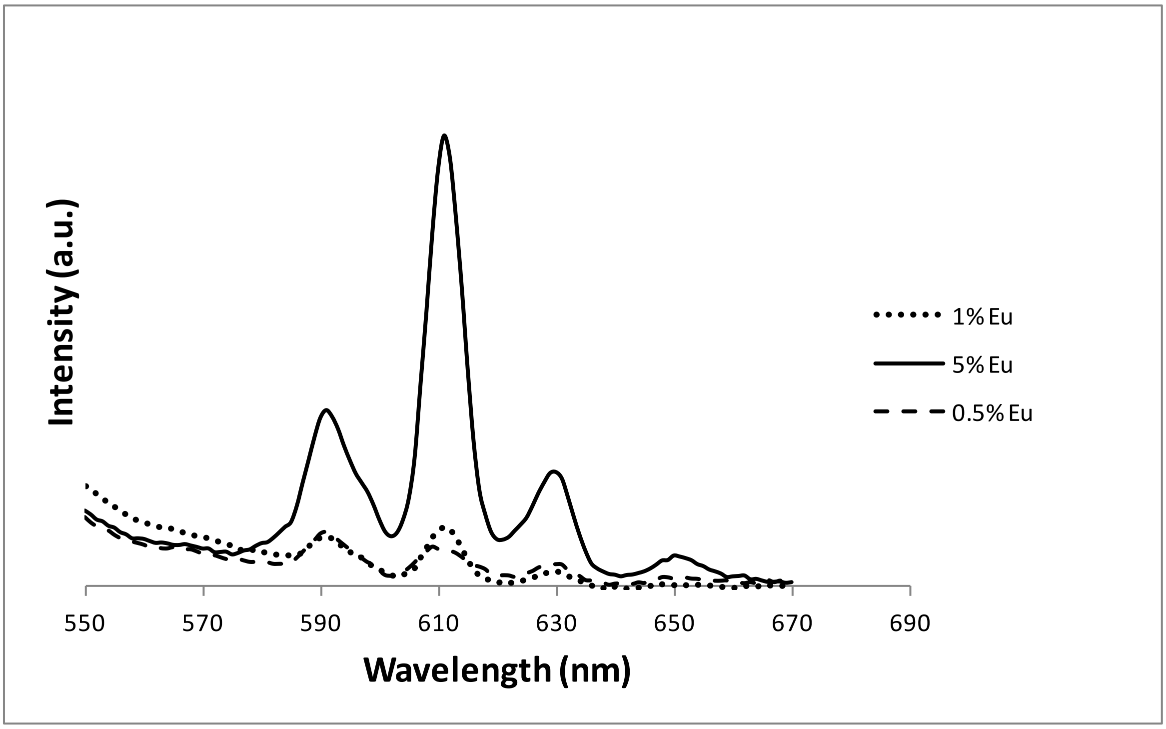

Figure 2.28 Emission spectra of 0.5, 1 and 5% doped Eu:YAG samples excited at 254 nm.

CHAPTER 3 Synthesis of Cerium dopedZnO and $Zn(OH)_2$

3.1 Introduction

Zinc oxide is one of the most important semiconductor and optoelectronic materials because of its wide band gap of 3.37 eV and large exciton binding energy of 60 meV. Because of its optical and electronic properties are heavily influenced by its size and morphology it has been in the center of interest over the past few years [105-108]. ZnO has several advantageous over other semiconductor materials such as nontoxicity, thermal stability, radiation resistance and ease to be synthesized in different nanostructures. Having those advantages make ZnO used in a wide range of applications such as UV light emitters, piezoelectric devices, chemical sensors, optoelectronic devices and photovoltaic devices [109-114]. As the morphology factors the electronic and optical properties majorly, different applications require different morphologies such as nanobelts, nanorods, nanowires, nanobridges and nanowhiskers [115-119].

Good optical properties and low cost of ZnO materials make them an excellent alternative in device applications such as optical devices. Having a large exciton binding energy (60 meV), ZnO is a promising material for light emitting devices in UV region. High efficiency UV photodetectors based on ZnO diodes have been reported in one study [120]. In 1968 Drapak reported the first ZnO based hybrid heterostructure LED with Cu_2O p-type layer [121]. In 2005, LED devices reported by only using p-type ZnO [122, 123]. ZnO also has laser applications. In 1998, Seeling *et al.* reported the first random lasing in UV region from the ZnO semiconductor powder under certain pumping conditions [124]. Some studies also reported lasing from ZnO in UV region when optically pumped [125, 126]. In near future ZnO based low threshold lasers may be used in optical applications such as pump sources for white light generation.

Due to its photocatalytic abilities ZnO is a recent interest in solar cells. Photocatalysis is an accelerator in a photoreaction. When a photon’s energy is greater than the band gap of a semiconductor one electron from the valence band promotes to the conduction band. The catalyst and absorbed materials such as $\mathrm{H_2O}$ on the catalyst surface go through redox reactions. The hole in the valence band combines with the surface water molecule to form hydroxyl radicals while the conduction band electron reduces the oxygen on the surface [127]. One dimensional ZnO morphologies such as nanowires and nanorods, show superior photocatalytic properties [128, 129]. Dye sensitized solar cells (DSSC) made of inorganic semiconductors have been in the center of interest as an cheap alternative for conventional silicon based solar cells. ZnO or $\mathrm{TiO_2}$ nanoparticles are deposited and sintered to form a film for electrical continuity. However, dye agglomeration, electrolyte leakage and loss of electron mobility due to polycrystalline structure of the semiconductors have been reported [130, 131].

ZnO also used for gas sensing. The resistivity change in the nanowire or thin film is the main mechanism that is used. ZnO nanowires with large enough surface area has been reported to used for sensing $NO_2^-\mathrm{NH_3}, \mathrm{NH_4^+}$, $\mathrm{CO}, \mathrm{H_2O}, \mathrm{O_3}$, $\mathrm{H_2S}$ and $\mathrm{C_2H_5OH}$ [132-139].

3.1.1 Structural Properties of ZnO

As stated above, the band gap of ZnO is 3.37 eV at room temperature [140]. Crystal structure of the ZnO is hexagonal wurtzite structure and lattice parameters are $a = 0.3296$ and $c = 0.5206$ nm. Alternating planes of tetrahedral $\mathrm{Zn^{2+}}$ and $\mathrm{O^{2-}}$ atoms overlap alternately overlap along c axis. The distance between $\mathrm{Zn^{2+}}$ and $\mathrm{O^{2-}}$ atoms is 0.1992 nm along c axis and 0.1973 nm in a ZnO molecule. Figure 3.1 shows the structure of ZnO [141]. Tetrahedral coordination does not have inversion symmetry and lacking of inversion symmetry brings piezoelectric and pyroelectric properties [141]. One important feature of the ZnO structure is its polar planes. Positively charged Zn^{2+} and negatively charged O^{2-} planes perpendicular to the c axis creates normal dipole moment and spontaneous polarization along c axis [142]. Although such polar surfaces usually are not stable and require massive surface reconstructions, ZnO surfaces are stable and flat, show no surface reconstruction [143, 144]. ZnO exhibits several different morphologies under different synthesizing conditions. Generally, all of these structures are determined by different growth rates of $\langle 2\bar{1}\bar{1}0\rangle$, $\langle 01\bar{1}0\rangle$ and $\pm[0001]$ directions.

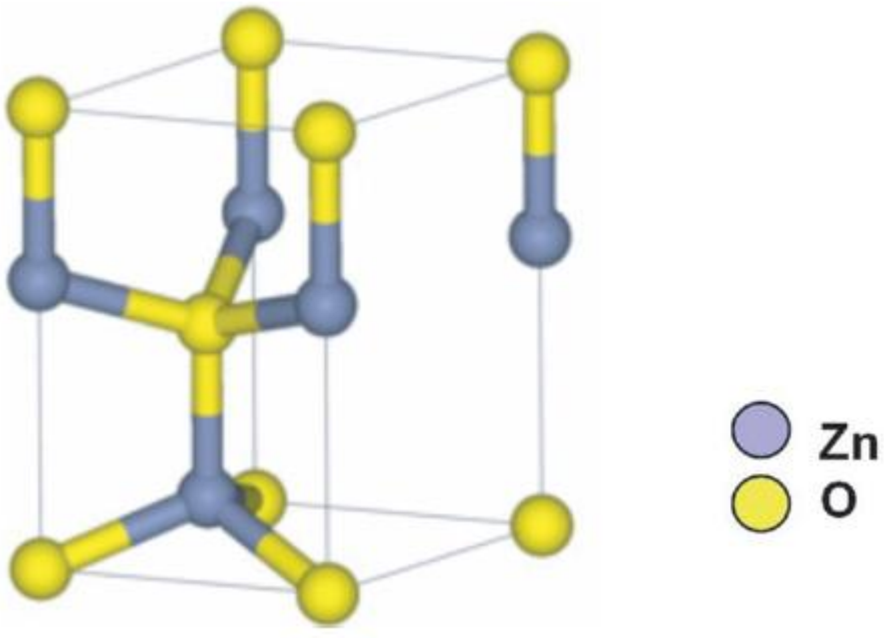

Figure 3.1 Wurtzite structure of $\mathbf{ZnO}$ molecule [141].

3.1.2 Synthesis of ZnO Nanoparticles via Hydrothermal

Conventionally, three methods are used in ZnO synthesis including, vapor phase deposition technique, chemical synthesis method and induction heating [145]. Hydrothermal method is a chemical method and has three basic steps during the growth of ZnO:

(1) Zinc salts ($Zn(NO_3)2\cdot6H_2O$) and hexamethylenetetramine ($(CH_2)_6N_4$) are kept in a container at temperatures between 70˚C and 90˚C.

(2) Concentration, pH, the temperature and the reaction time are optimized to achieve controlled morphologies.

(3) After reaction completes, precipitated sample is collected and rinsed with water. Samples are dried at 60˚C-90˚C.

Hydrothermal method is in particular interest because the changes in the solution conditions have a strong influence in morphology [146, 147]. Addition of the organic agents also factors the morphology [148, 149]. Hexamine has been reported to form crystals with large prismatic face, when added to the growth solution [150]. In hydrothermal method the reaction rate is increased by increasing the solubility of the solid content in a solvent about its critical point with the aid of the increasing temperature and pressure. Usually a solution of the precursor and an agent adjusting crystal growth is prepared in stoichiometric ratios reacts at elevated temperature and pressures.

At 90˚C and pH 11.5, zinc sample is in $Zn(OH)_4^{2-}$ solution form [151]. $Zn(OH)_4^{2-}$ molecules add to the surface of the growing ZnO crystals from the solution [152]. When small organic surfactants attached to the certain planes of $Zn(OH)_4^{2-}$ molecule, the surfactant molecule inhibits the growth of that crystal face [150]. $Zn(OH)_2$ is an intermediate phase during ZnO growth. Shaporev *et al.* reported that, at low temperatures $Zn(OH)_2$ is formed from basic aqueous zinc solution and when the $Zn(OH)_2$ is heated it turns into ZnO [153]. They concluded that ZnO particles are formed from $Zn(OH)_4^{2-}$ intermediate phase depending on the solution conditions. Although several structures of $Zn(OH)_2$ have been reported, only naturally occurring structure is Wülfingite [154]. Wülfingite has orthorhombic crystal structure however, ZnO Würtzite structure is close packed hexagonal. Zn^{2+} ion is attached to four oxygen atoms tetrahedraly in both structures. In Würtzite structure oxygen connects four zinc tetrahedral while in Wülfingite it only connects two. The reaction of $Zn(OH)_2$ to ZnO is represented as following:

$$\mathbf{Zn(OH)_{2\,(s)} \rightarrow ZnO_{(s)} + H_2O_{(l)}} \qquad (3.1)$$

Sun *et al.* explained the hydrothermal synthesis of ZnO using dodecyltrimethyl ammonium bromide ($C_{12}TAB$) and Zn powder as [155]:

$$\mathbf{Zn + H_2O \rightarrow Zn^{2+} + H_2 \uparrow + OH^-} \qquad (3.2)$$

$$\mathbf{Zn^{2+} + 4OH^- \rightarrow Zn(OH)_4^{2-} + C_{12}TAB \rightarrow ZnO + H_2O + C_{12}TAB} \qquad (3.3)$$

Surface free energy needed to form ZnO nuclei is lowered by the surfactant as surfactant lowers the surface tension of the solution. Therefore, ZnO crystals can be grown at lower supersaturation conditions. With the crystal growth, $C_{12}TAB$ film is formed between the ZnO and solution as an interface layer. $C_{12}TAB$ molecules release the growing units at the (0001) surface of the ZnO single crystal because in $C_{12}TAB$ film the molecules tend to be perpendicular to the growth surface of the ZnO single crystal. Addition of growing units results in the formation of $\mathrm{Zn-O-Zn}$ bonds in [0001] surface. These steps are repeated and the ZnO crystal grows along the [0001] direction [155].

3.1.3 Synthesis of Layered ZnO Particles with SDS

Layered $Zn(OH)_2$ structures has been in the center of interest as lamellar structure enhance the electrochemical and photoelectrochemical properties by increasing the surface area [156-160]. Different anionic surfactants such ethylenediaminetetraacetic acid (EDTA), sodium dodecyl sulfate (SDS), cetyltrimethylammonium bromide (CTAB), polyethylene glycol (PEG) and polyethyleneimine (PEI) have been investigated [161-166]. Layered zinc hydroxide structure is same with $\mathrm{Mg(OH)_2}$ (brucite) structure. In $\mathrm{Mg(OH)_2}$, Mg^{2+} ions are octahedraly coordinated with OH^- groups. These octahedras form layers and OH^- groups are perpendicular to the layers stack upon each other [167]. With the addition of an anionic surfactant, surfactant molecules can be intercalated between these layers therefore layered structure formed. The structure can be represented:

$$\mathbf{M^{2+}(OH)_{2-x}(A^{m-})_{x/m} \cdot nH_2O} \qquad \textbf{(3.4)}$$

where $\mathrm{M^{2+}}$ is metal ion and $\mathrm{A^{m-}}$ is counter ion.

If anionic surfactant is added into the solution during the hydrothermal synthesis of $Zn(OH)_2$, hydroxide layers are intercalated by anionic surfactant molecules. When SDS is used as surfactant in the zinc salt solution, SDS molecule attaches to the Zn^{2+} ion and form micelles. With the increasing temperature HMTA or urea decomposes and release NH_4^+ to the environment therefore the Zn^{2+} ions precipitates and forms $Zn(OH)_2$ layers. SDS molecules attached to the Zn^{2+} ions at the edges of the zinc tetrahedrons. Figure 3.2 shows the formation of the SDS molecules attached to the zinc tetrahedrons. Alkyl chains of SDS molecules create interlayer interactions between the layers [168].

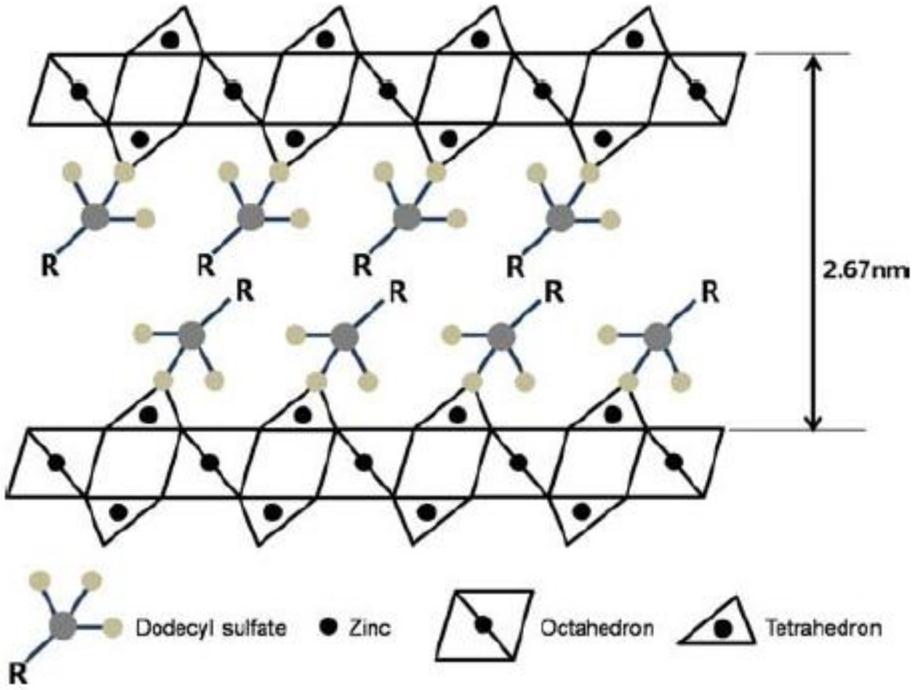

Figure 3.2 Shows the formation of the layered $Zn(OH)_2$ structures and intercalated dodecyl sulfate groups [169].

Lamellar zinc oxide films prepared by electrochemical methods were also reported [170, 171]. In this method acidic zinc nitrate solution is used to synthesize lamellar structure. With the reduction of the nitrate, pH increases and the ZnO film precipitates. Reduction of nitrate represented as:

$$\mathbf{NO_3^- + H_2O + 2e^- \rightarrow NO_2^- + 2OH^-} \tag{3.5}$$

Layered structure is reported when the electrolyte contains a small amount of anionic surfactant [171].

3.2 Purpose of the Study

The second purpose of this study is investigating the evolution of ZnO and $Zn(OH)_2$ morphologies under various conditions. ZnO materials are important for optical and photochemical applications and through the modification of their morphologies, the optical and electrical properties can be altered to the desired level.

3.3 Experimental

3.3.1 Hydrothermal Synthesis of Ce:ZnO

Ce^{3+} doped ZnO samples were prepared by hydrothermal route and $Ce(NO_3)_3·6H_2O$ (Alfa Aesar 99.5%) and $Zn(NO_3)_3·6H_2O$(Alfa Aesar 99%) salts were used as starting materials. Figure 3.3 shows the flow chart of the process. 0.002 mol Zn^{2+} salt were dissolved in 100 ml distilled water. Ce^{3+} salt was calculated in stoichiometric amounts which yield 1, 5 and 10% in the end products. Various amounts of HMT and SDS were added into the solution as pH altering agent and surfactant respectively. The solution was poured into a three necked bottle with a cooling block attached. After the stir bar was put in to the three necked bottle, the system was sealed with rubber bands. Under constant stirring the system was heated to the 90˚C for varying time amounts. When the reaction completed the sample was centrifuged at 6000 rpm to separate the precipitates from the liquid part. Solid sample was rinsed with distilled water to get rid of unwanted chemicals. After a drying process at 60˚C for 24 h, the samples were obtained. The table 3.1 shows the list of samples synthesized for this study.

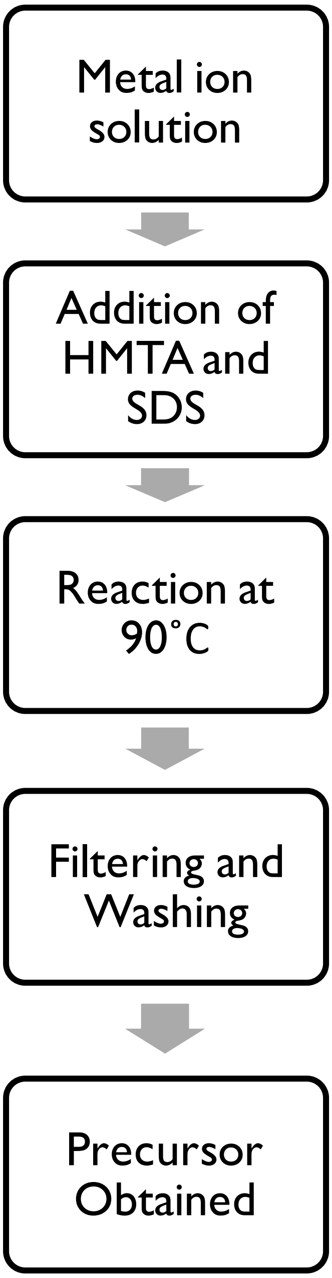

Figure 3.3 Flow chart of hydrothermal ZnO and $Zn(OH)_2$ synthesis process.

Table 3.1 ZnO and $Zn(OH)_2$ samples used in this study.

Sample #	Dopant (%)	SDS (mol)	HMT (mol)	Time
Zn1	1%	-	0,002	6
Zn2	1%	-	0,005	6
Zn3	1%	-	0,012	6
Zn4	5%	-	0,012	6
Zn5	10%	-	0,012	6
Zn6	1%	0,005	0,002	6
Zn7	1%	0,005	0,002	24
Zn8	5%	0,005	0,002	6
Zn9	5%	0,005	0,005	6
Zn10	5%	0,005	0,012	6
Zn11	5%	0,005	0,012	12
Zn12	5%	0,005	0,012	24
Zn13	1%	0,005	0,005	6
Zn14	1%	0,005	0,012	6
Zn15	1%	0,005	0,005	24

3.3.2 Characterization

Characterization of samples was performed by XRD, FESEM, and FTIR. Phase identification and structural properties were investigated via XRD (X-ray diffraction analysis, Bruker D2 Phaser). Measurements were performed between $0^\circ<2\theta<90^\circ$ range at room temperature. FESEM (Field emission scanning electron microscope, Zeiss Ultra) samples were prepared as 1mg samples were dispersed in 1ml ethanol and exposed to ultrasonic vibration. After drying, FESEM images were taken to examine the micro structures of powder samples. For Fourier Transformed Infrared Spectroscopy (FTIR) measurements, Omnic 6.0 Software is used to monitor/analyze the spectra. ATR-IR spectra were recorded on a thermo scientific Smart iTR Instrument with Diamond ATR crystal and with an incident angle of 42° 16 scans between 4000 and 525 cm^{-1} were taken for each spectrum with a resolution of 4 cm^{-1}.

3.4 Results and Discussion

3.4.1 The Effect of the Reaction Time

In order to understand effect of the time on the growth mechanism of the ZnO microcones SEM pictures of 6 h reacted and 24 h reacted samples are collected. Samples synthesized via hydrothermal route with 0.005 mol SDS and 0.002 mol HMT per 0.002 mol $\mathrm{Zn(NO_3)_2 \cdot H_2O}$ are shown in figure 3.5. Cone shaped morphology for Co^{2+} and Cd^{2+} was reported before but we have not seen any publication related to cone morphology for $Zn(OH)_2$ [172].

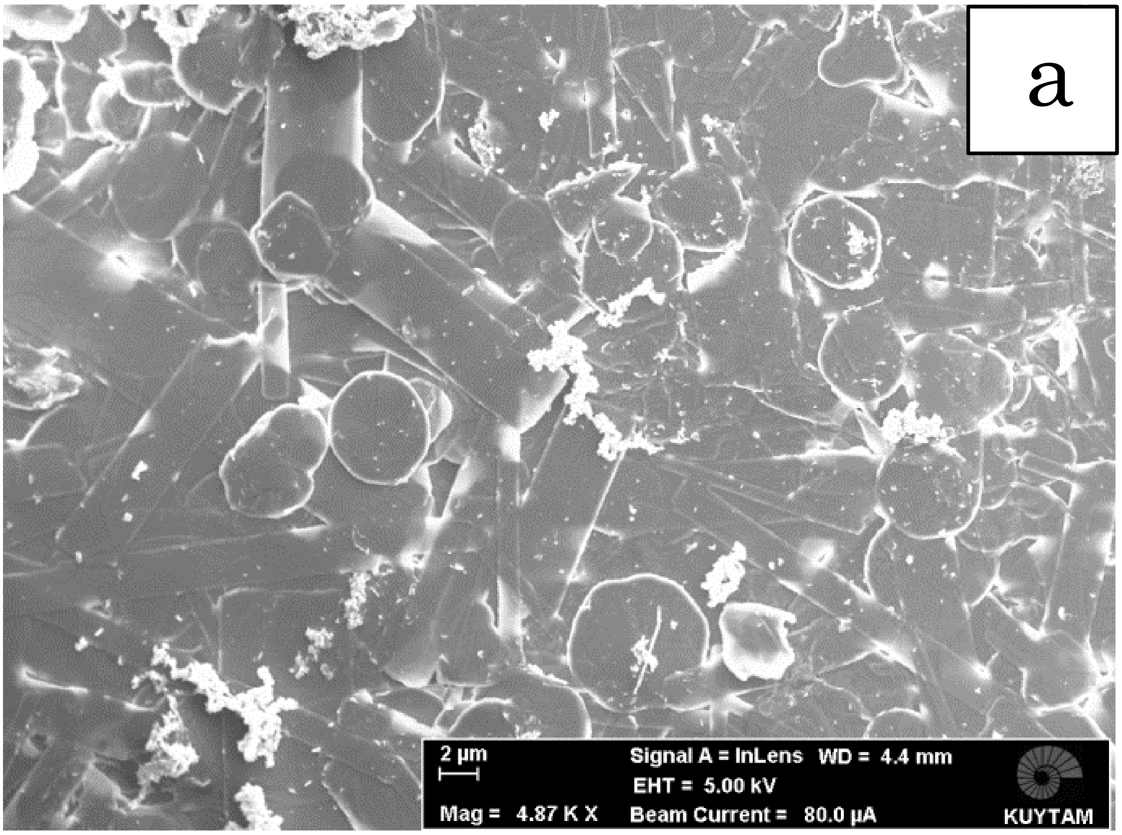

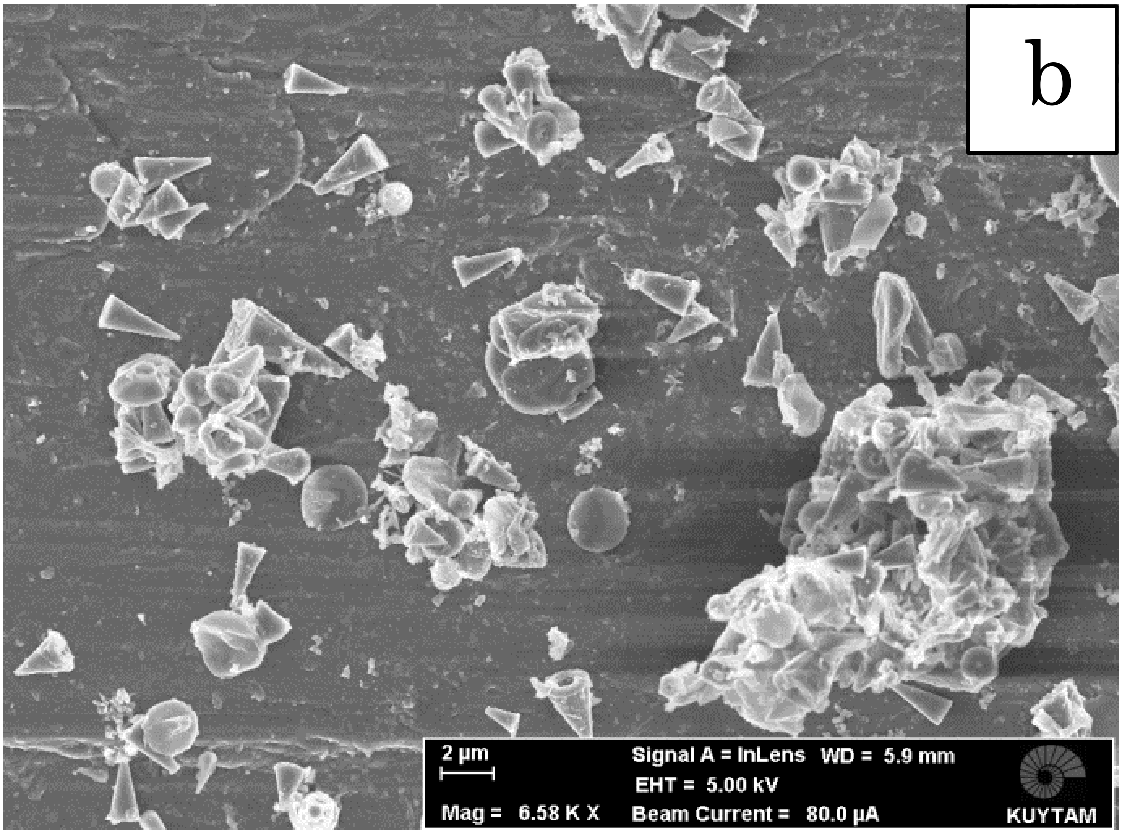

Figure 3.4 SEM images of the ZnO precursor samples synthesized via hydrothermal route with SDS. Image (a) is from Zn6 reacted 6 h and image (b) is from Zn7 reacted 24.

For the formation of nanocones, reaction time longer than 6 hours was required as seen in the figure 3.5. The samples have a plate like shapes after 6 h of reaction. The lamellar structures observed for the morphology of 6 hours reaction time was typical for metal hydroxides. However, as it is seen in the image (b) the sample turn into a cone like morphology with the increasing reaction time. Figure 3.6 shows the samples synthesized via hydrothermal route with 0.005 mol SDS as the samples discussed above but with 0.012 mol HMT per 0.002 mol $\mathrm{Zn(NO_3)_2 \cdot H_2O}$. Results are similar with the samples discussed above. Image (a) shows the sample reacted 12 h. Even though plate like morphology is visible at the 12h reacted sample, majority of the sample consist of microcones. The 6 h reacted sample has plate like shape and microcones have not been formed yet as seen in image (b).

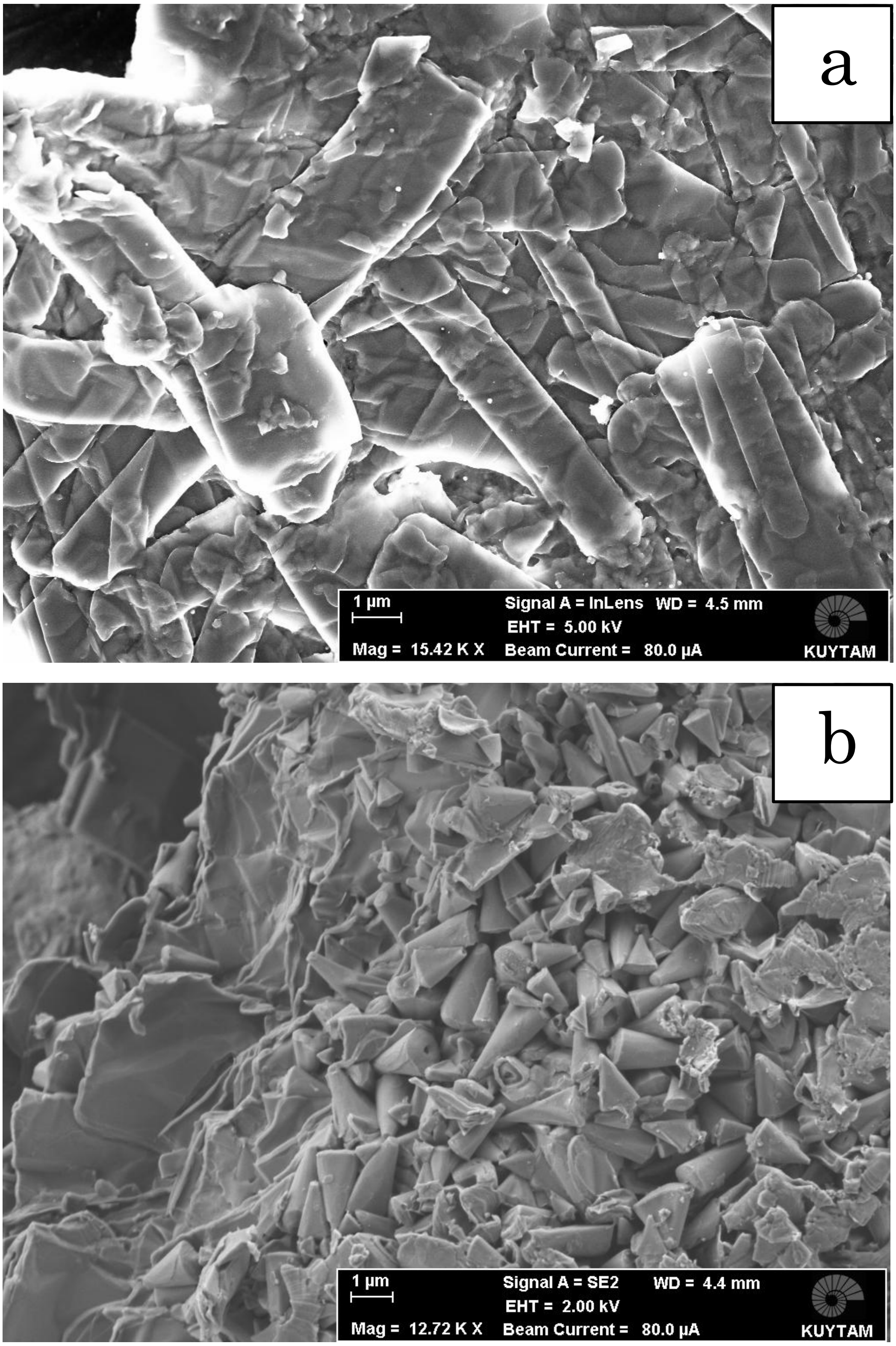

Figure 3.5 SEM images of the ZnO precursor samples synthesized via hydrothermal route with SDS. Image (a) is from Zn Zn10 reacted 6 h and image (b) is from Zn11 reacted 12 h.

XRD data in figure 3.7 shows the samples synthesized via hydrothermal route for 6 h 12h and 24 h with using 0.005 mol SDS and 0.012 mol HMT per 0.002 mol $\mathrm{Zn(NO_3)_2 \cdot H_2O}$ used. $\theta = 2.9^\circ, 5.95^\circ, 8.77^\circ, 11.66^\circ$ and 14.55° peaks are present in all three samples. XRD patterns are typical for SDS intercalated metal hydroxides [173]. Periodic *(00l)* peaks at low 2theta angles are the evidence of intercalation of SDS into the interlayer. Intercalated SDS expands the interlayer distance as explained in further sections. Crystallite sizes of the samples are 38.6 nm, 51.8 nm and 43.4 nm respectively for 6 h, 12 h and 24 h samples. Crystallite sizes are calculated from the peak at $\theta = 2.9^\circ$. The d value (interlayer distance) is around 30 Å which indicates that dodecylsulfate was oriented perpendicularly. For intercalation products with such interlayer distance, bilayer perpendicular arrangement of SDS molecules is the most probable. In the bilayer arrangement, the hydrophobic chains of the SDS molecules overlap in the interlayer. The complete overlap with 90^o arrangement with respect to the metal hydroxide layer would give a layer distance of around 26 Å. Thus, the arrangement of the SDS molecules in $Zn(OH)_2$ molecules in this study is probably with a slight inclination with respect to the metal hydroxide layer.

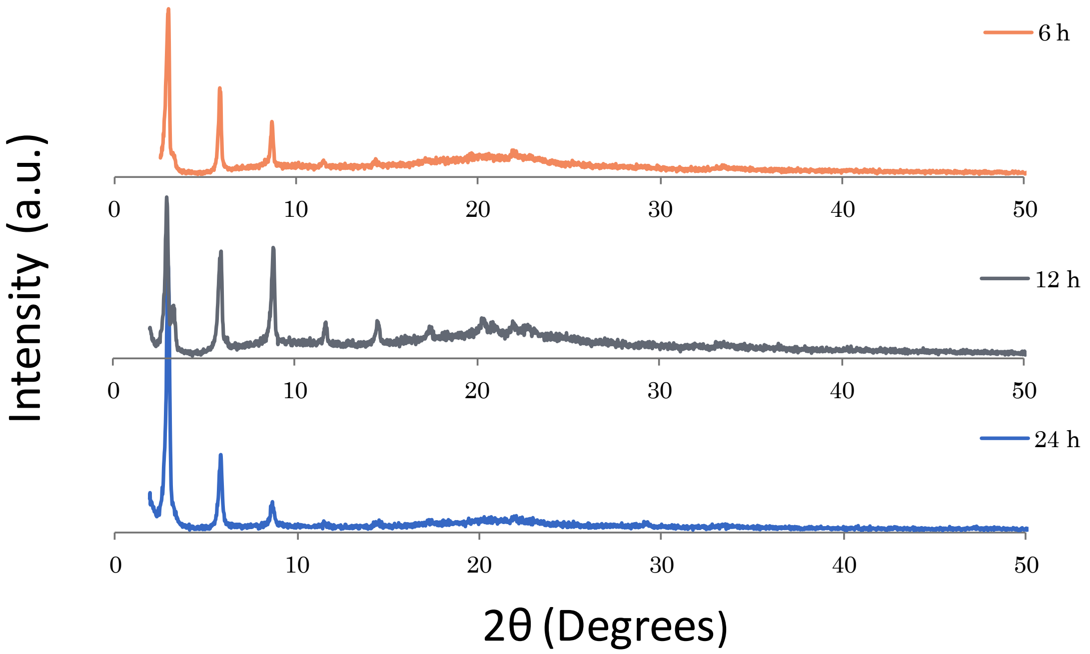

Figure 3.6 XRD patterns of Zn10, Zn11 and Zn12 samples synthesized via hydrothermal route for 6 h 12h and 24 h.

3.4.2 The Effect of the SDS

The effects of SDS were investigated on the formation of the cone morphologies. Figure 3.8 shows the SEM images from the samples synthesized via hydrothermal route with same amount of HMT and reacted same time but with different amounts of SDS. Image (a) and (c) show how the morphology is formed with the aid of SDS. Microcones were formed in the samples with the 0.005 mol SDS. Each cone is about 1 μm in size. However, image (c) and (d) from the sample with no SDS shows the common hexagonal morphology reported in the literature [141, 174]. Hexagonal structure is the typical ZnO structure as ZnO crystals tend to maximize the $\{2\bar{1}\bar{1}0\}$ and $\{01\bar{1}0\}$ areas in order to minimize the energy [141].

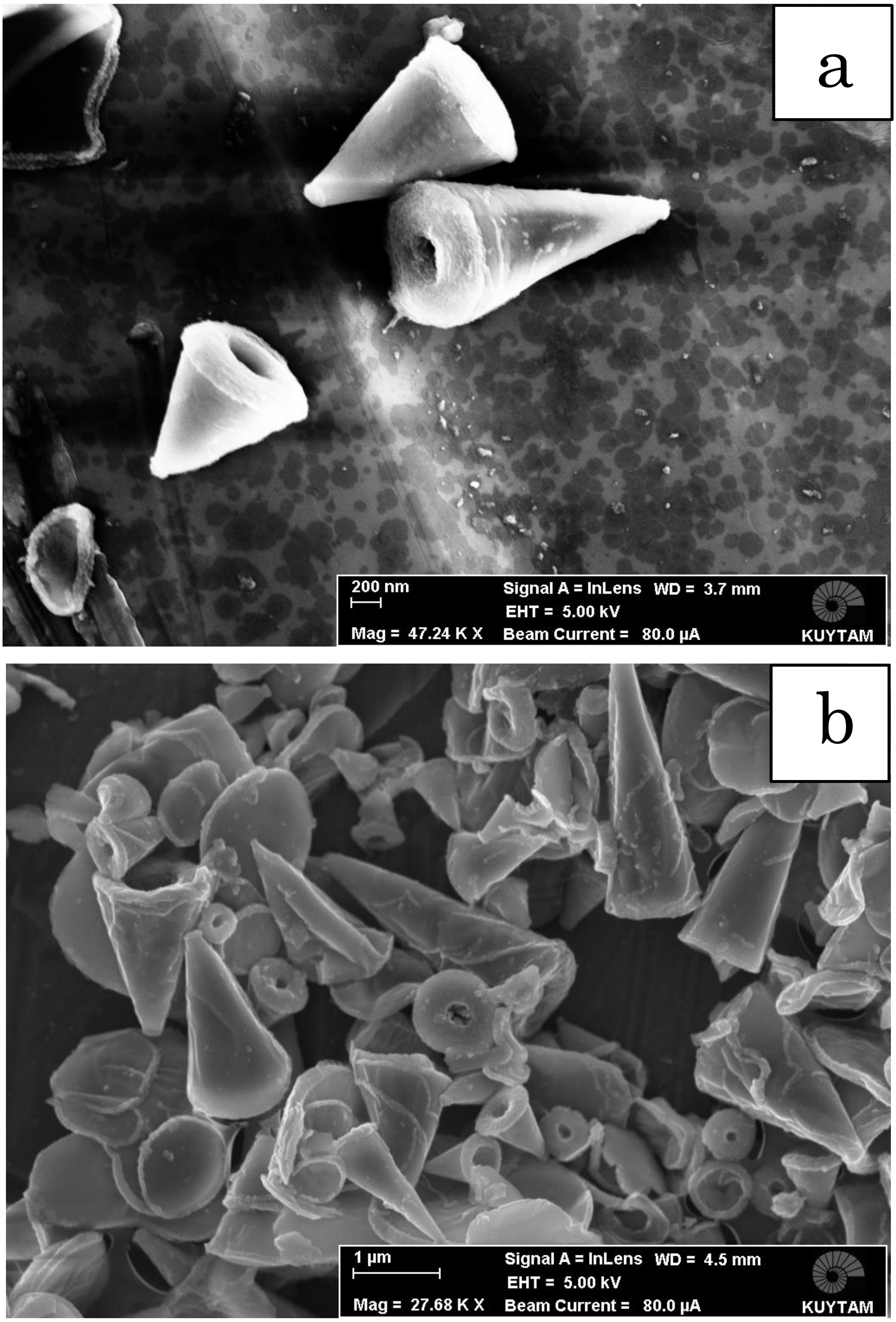
a
200 nm
Signal A = InLens WD = 3.7 mm
EHT = 5.00 kV
Mag = 47.24 K X Beam Current = 80.0 µA
KUYTAM
b
1 µm
Signal A = InLens WD = 4.5 mm
EHT = 5.00 kV
Mag = 27.68 K X Beam Current = 80.0 µA
KUYTAM

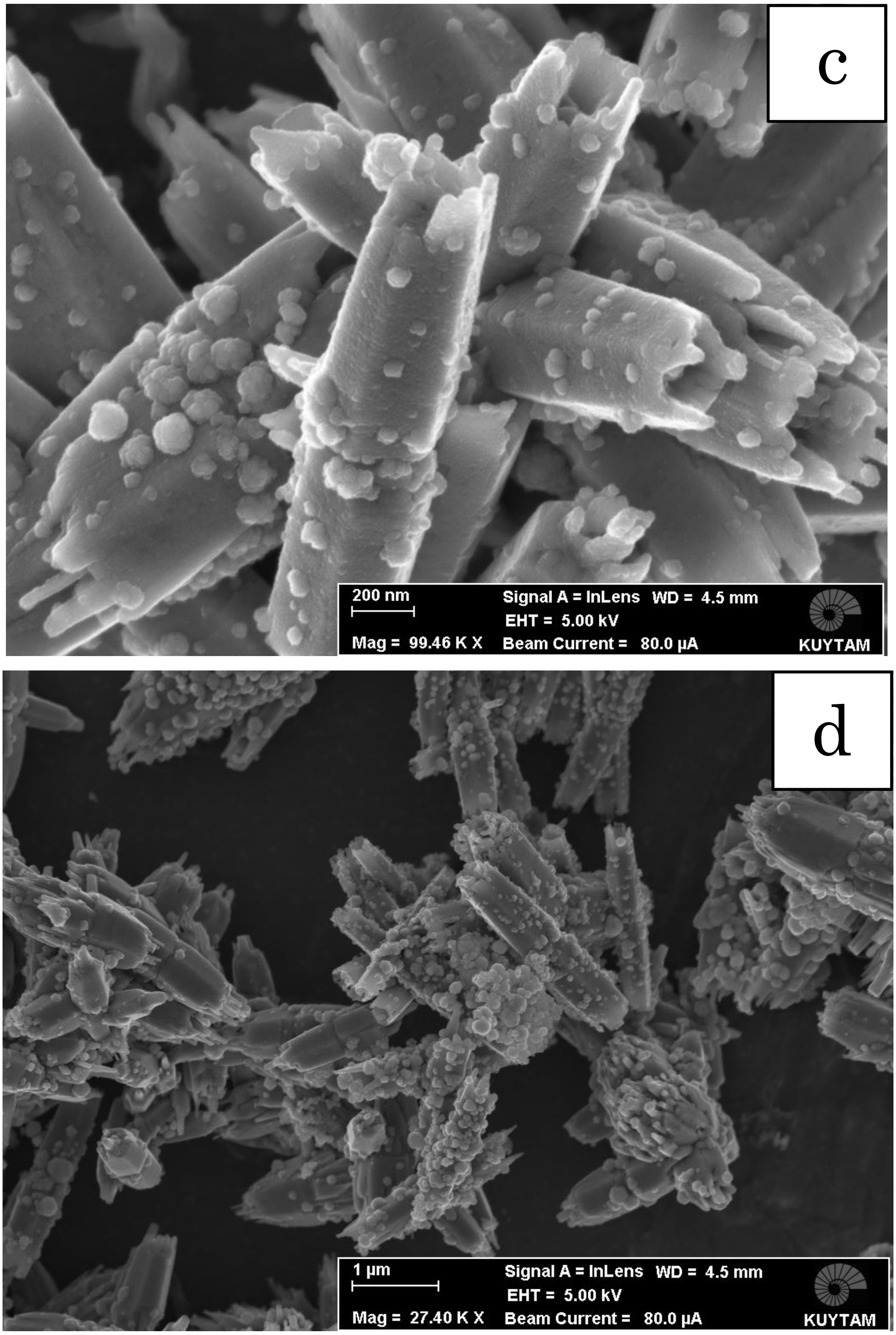

Figure 3.7 SEM images of the ZnO precursor samples synthesized via hydrothermal route with and without SDS. Image (a) and (b) belong to Zn10 sample while image (c) and (d) belong to Zn4.

XRD data in figure 3.9 shows the effect of SDS on crystal structure. The samples synthesized via hydrothermal route for 6 h with using 0.012 mol HMT per 0.002 mol $\mathrm{Zn(NO_3)_2 \cdot H_2O}$. The XRD pattern of the sample with 0.005 mol SDS has five peaks at $2\theta = 2.9^\circ, 5.95^\circ, 8.77^\circ, 11.66^\circ$ and 14.55°. However none of those peaks are characteristic peaks of ZnO wurtzite structure [175]. However samples reacted with no SDS show the three characteristic peaks at $\theta = 32.03^\circ, 34.7^\circ$ and 36.48° of ZnO wurtzite structure [176]. Crystallite sizes of the samples are 38.6 nm, 51.8 nm and 43.4 nm respectively for 6 h, 12 h and 24 h samples. Crystallite sizes are calculated from the peak at $\theta = 2.9^\circ$.

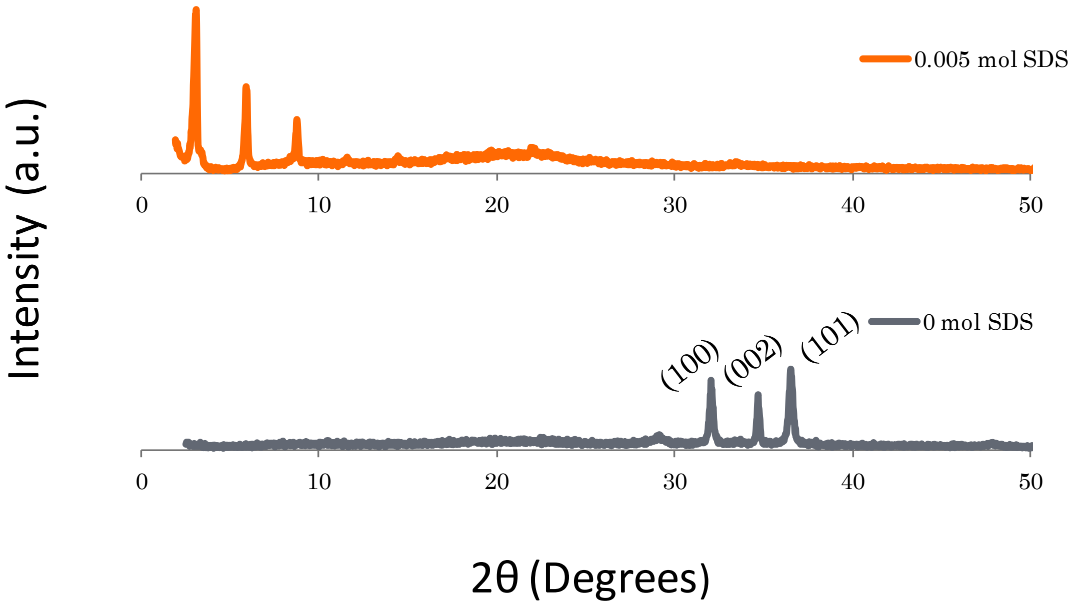

Figure 3.8 Comparison of the XRD patterns of the Zn4 and Zn10 samples with different SDS amounts. Samples are synthesized via hydrothermal route with 0.012 mol HMT per 0.002 mol $\mathbf{Zn(NO_3)_2 \cdot H_2O}$.

3.4.3 The Effect of the HMT

Figure 3.10 shows the samples synthesized with no SDS but varying amounts of HMT. The samples reacted for 6 h in hydrothermal conditions. As it is discussed above cone shape is not present without the SDS Image (a) is from the sample with 0.002 mol HMT per 0.002 mol $\mathrm{Zn(NO_3)_2 \cdot H_2O}$. The sample consists of starlike and rodlike morphologies. Stars are formed by aggregation of many 1D rods as reported in literature [177]. The sample contains 0.005 mol HMT per 0.002 mol $\mathrm{Zn(NO_3)_2 \cdot H_2O}$ is shown in the image (b). Comparing the two images, despite the similar particle size morphology of the sample with 0.005 HMT is rodlike and no star shapes is present. Image (c) is from the sample synthesized with 0.012 mol HMT and the sample has bigger particles that two previous samples. $\mathrm{CeO_2}$clusters are visible upon the rods. All samples show hexagonal shape without the SDS.

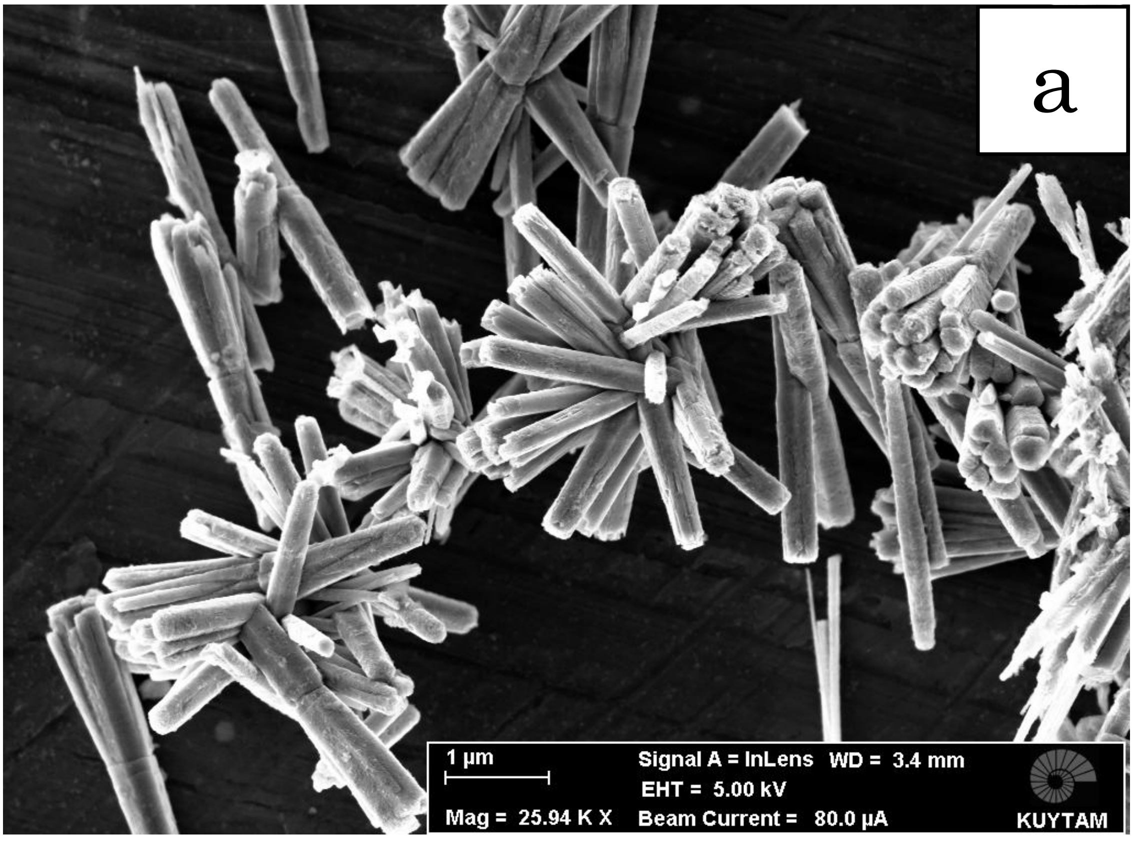

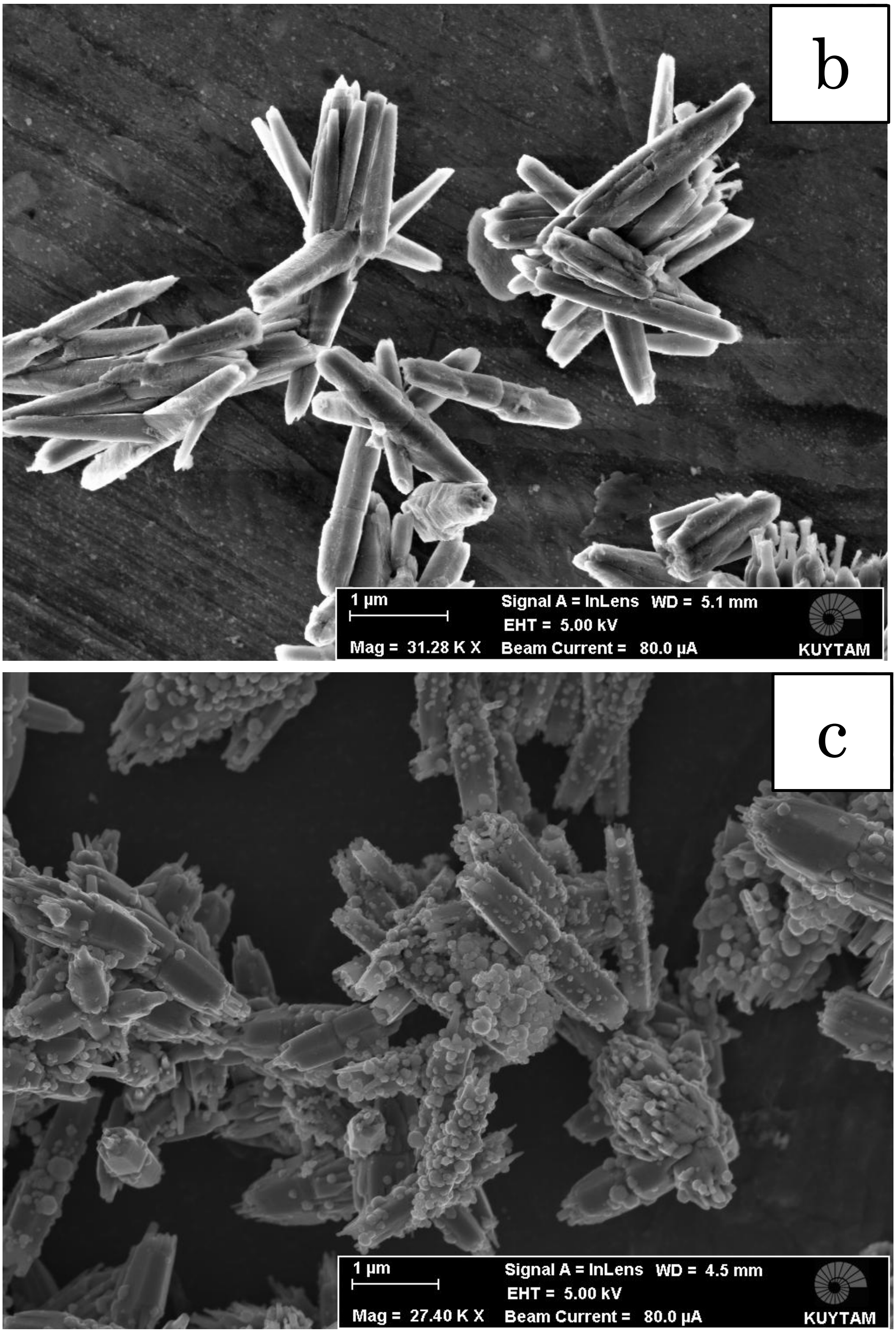

Figure 3.9 SEM images of the Ce:ZnO precursor samples synthesized via hydrothermal route with no SDS and reacted 6 h. The image (a) image (b) and image (c) show the Zn1, Zn2 and Zn4 samples containing 0.002, 0.005 and 0.012 mol HMT respectively. The sample in image (c) is 5% doped while the ones in image (b) and (c) contains 1% Ce^{3+}

In figure 3.11, samples reacted 6 h with the aid of SDS are shown. As discussed above, with the addition of SDS morphology tends to be in conelike. However in 6 h samples cone shape is not visible and sample shows microplates. The samples shown in image (a), image (b) and image (c) contain 0.002 mol HMT, 0.005 mol HMT and 0.012 mol HMT per 0.002 mol $Zn(NO_3)_2 \cdot H_2O$ respectively. Comparing the decreasing HMT amount the particle size of plates becomes bigger.

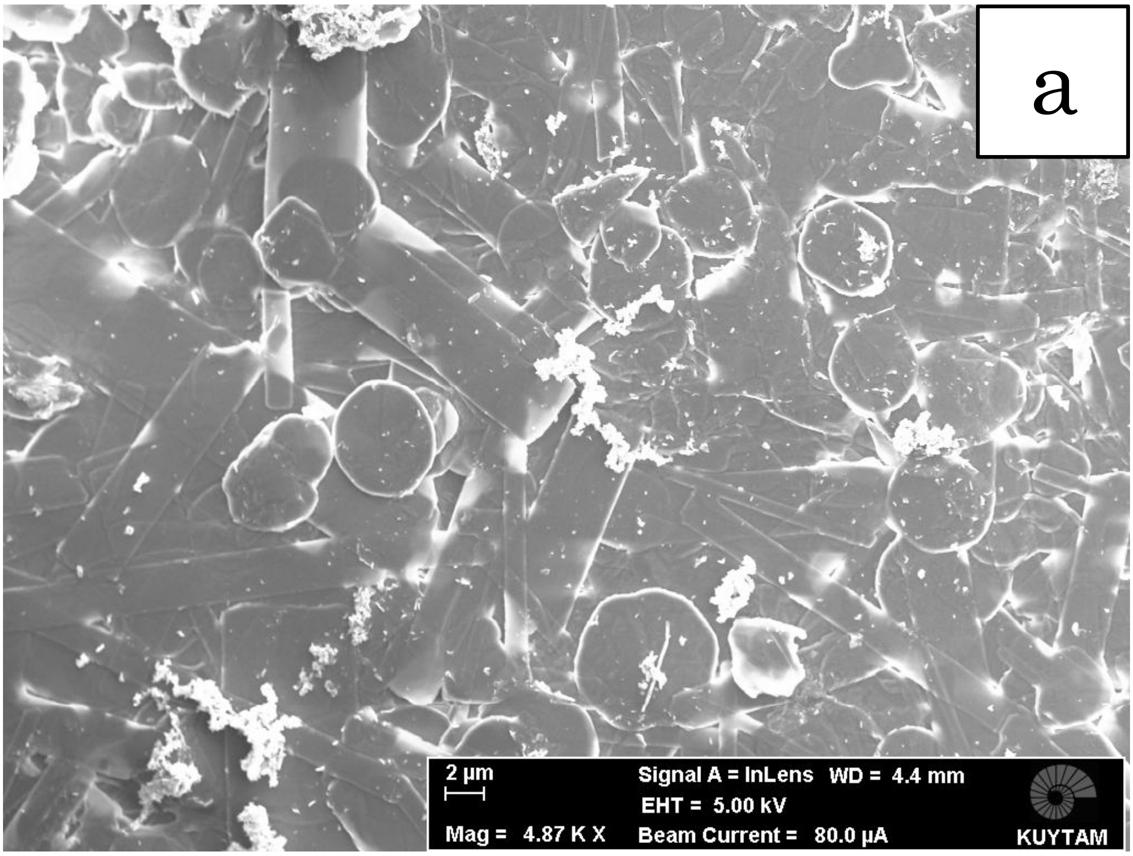

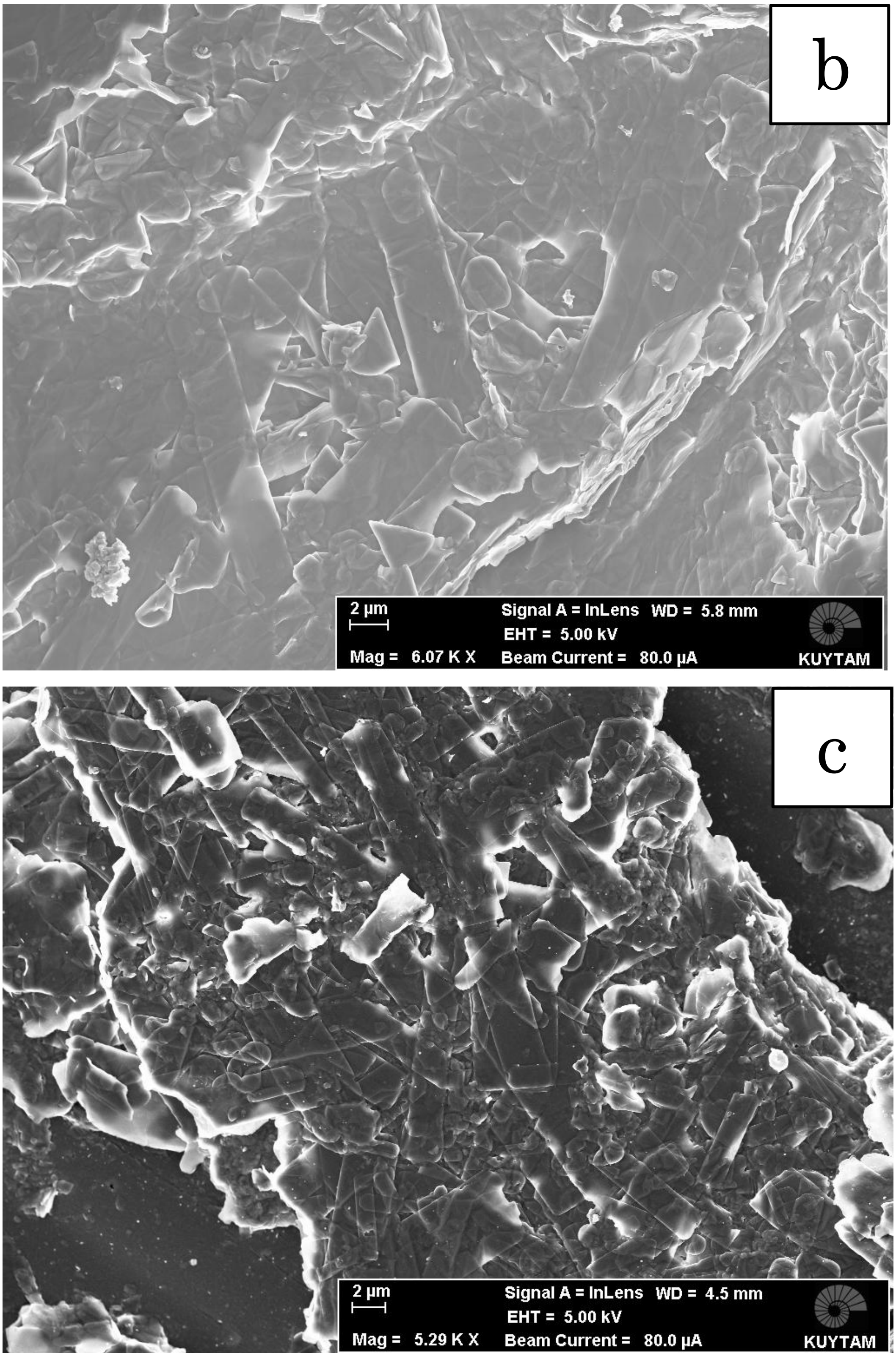

Figure 3.10 SEM images of the $Zn(OH)_2$ samples synthesized via hydrothermal route with 0.005 mol SDS. The image (a) image (b) and image (c) show the samples Zn6, Zn13 and Zn14 with 0.002, 0.005 and 0.012 mol HMT respectively.

Results from the samples reacted 24 h in the figure 3.12 agree with this decrease in particle size. With the increasing time cone shaped particles are dominant. Comparing the sample contains 0.002 mol HMT per 0.002 mol $\mathrm{Zn(NO_3)_2 \cdot H_2O}$ in image (a) with the sample contains 0.005 mol HMT per 0.002 mol $\mathrm{Zn(NO_3)_2 \cdot H_2O}$ in image (b), increasing HMT amount cause a decrease in the particle size.

Formation of cones for metal hydroxides in the presence of SDS was also observed in the literature [178]. Synthesis of metal hydroxides in the presence of surfactants like SDS forms a layered structure with surfactants intercalated into the space between metal hydroxide layers and these structures have been commonly observed in the literature. Formation of cones, however, was reported only in a few article. In principle, surfactant molecules in an aqueous solution of a metal react with the metal cation and metal-SDS ion pairs are formed. In order to minimize the energy, these cation-SDS pairs forms micelles, which is commonly known behavior of surfactant in an aqueous solution. When a precipitating agent like HMTA or NaOH is introduced into the solution metal ions reacts with hydroxyl ions to form metal hydroxide layers and a layered metal hydroxide lamellar structure with SDS intercalated between the metal hydroxide layers was obtained. Observed structure is generally a planar lamellar structure [179] but tubular or conical structures may also be obtained [172]. According to Tsai et al formation of conical structure may be more likely because of higher stability of cones than the lamellar structure [172]. We have observed in our study that cone formation is time dependant and longer reaction times result in formation of cones.

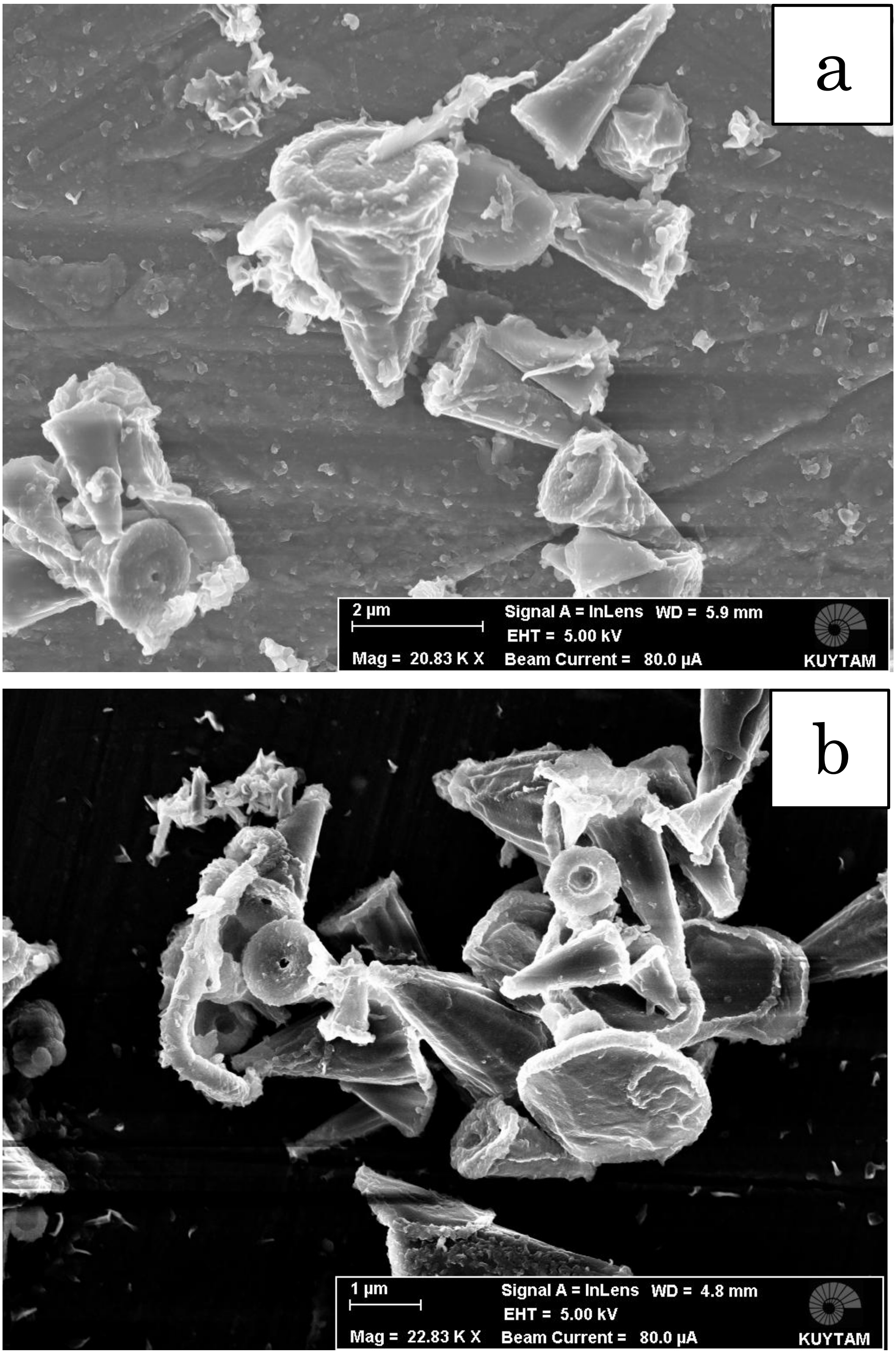

Figure 3.11 SEM images of the ZnO precursor samples synthesized via hydrothermal route with 0.005 mol SDS. The image (a) and image (b) show the samples Zn7 and Zn15 respectively.

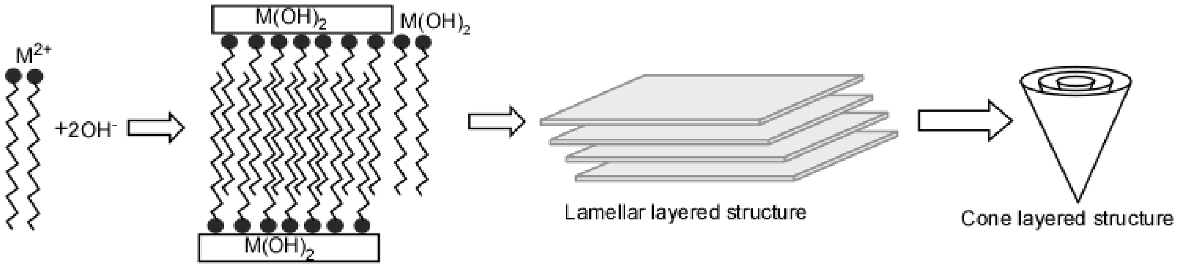

Figure 3.12 Crystallization of SDS intercalated layered metal hydroxide layers and cone formation

3.4.4 FTIR results

Fourier transform infrared spectroscopy (FTIR) was used in order to confirm the existence of the interlayer SDS molecules. Figure 3.14 shows the FTIR spectrum of ZnO samples with SDS reacted at 6 h and 24 h. The FTIR spectra of the SDS intercalated ZnO samples show band belong to both surfactant and zinc hydroxide lattice vibrations. As seen in the figure, the longer reaction time will not bring any abrupt change in the structure of the surfactant. The broad peak in the region 3150-3600 cm^{-1} is typically as a result of O-H stretching mode and intercalated H_2O. The small shoulder around 3060 cm^{-1} indicates the hydrogen bonded hydroxyl groups from the metal hydroxide [180]. The peaks at 1620 cm^{-1} is due to the bending mode of water. We have observed characteristic 2848, 2916 and 2985 cm^{-1} bands attributed to the C-H stretching vibrations of dodecyl sulfate [180]. The bending peak for $-CH_2$ is observed at 1466 cm^{-1}. The symmetric vibration of S=O can be observed at 1084 cm^{-1} for free SDS but it is shifted t0 1060 cm^{-1} for the intercalated SDS. Asymmetric vibration of S=O can be observed at 1220 cm^{-1}.

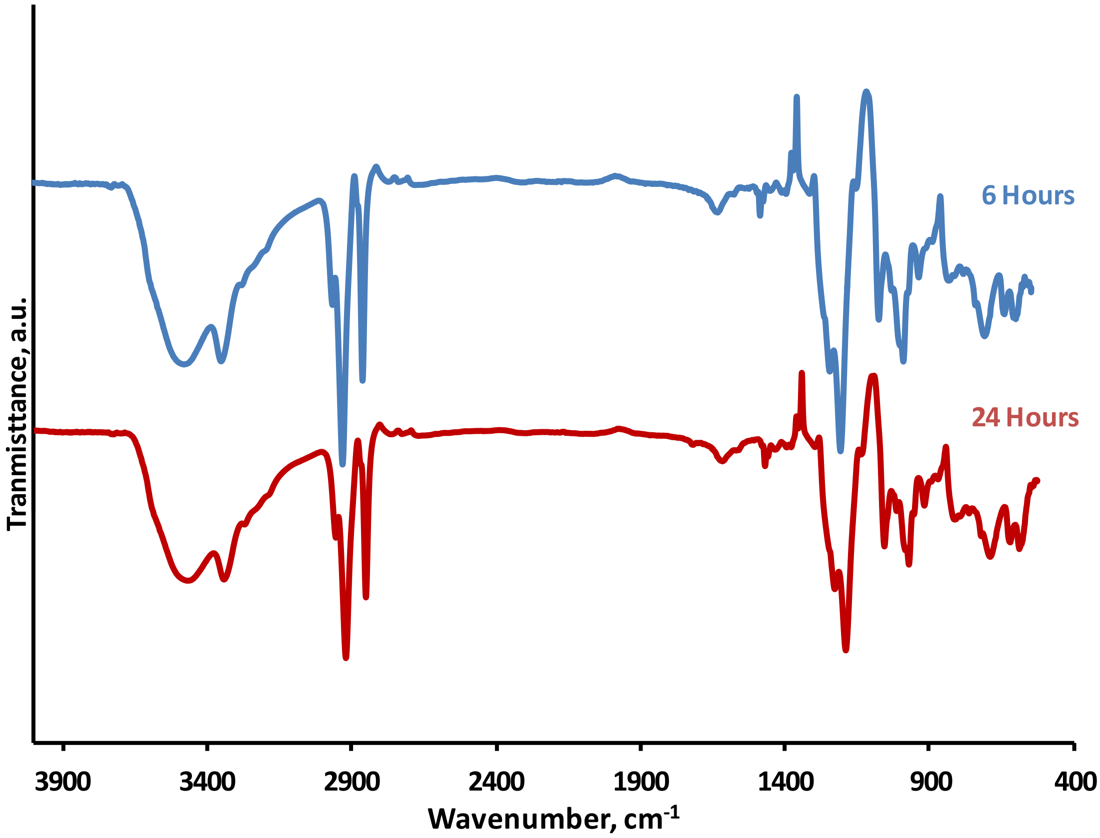

Figure 3.13 FTIR results of samples reacted for 6 and 24 h with SDS

CHAPTER 4 Conclusion & Summary

4.1 Synthesis of YAG Powders

Effects of powder synthesis methods over powder characteristics were investigated. Solid state reaction, citrate method and three routes of co-precipitation, reverse-strike, normal-strike and hydrothermal, were used to produce 1% Ce^{3+}, Eu^{3+} and Nd^{3+} doped yttrium aluminum garnet (YAG) samples. Samples were calcined from 900˚C to 1300˚C for several hours through one step or multi steps. X-ray diffraction analysis (XRD) was used to characterize the structural properties of the samples and the evaluation of phases present in the microstructure. Results show the pure YAG phase for reverse-strike and citrate samples calcined at even at 900˚C. These results were not be able to replicated in the samples produced via other methods. Crystallite sizes were calculated from the XRD patterns. Grain growth was more dominant in the samples which calcined through multiple steps. Scanning electron microscopy images were taken to verify the grain growth of the samples. The findings agreed with XRD patters as the particles became larger in samples calcined through multiple steps. Ce^{3+} and Eu^{3+} samples were excited at 465 nm and 256 nm respectively. Emission spectra of the samples were similar with those reported in the literature.

4.2 Synthesis of ZnO and $Zn(OH)_2$

ZnO and $Zn(OH)_2$ samples synthesized via hydrothermal method with the aid of HMT at 90˚C. Sodiumdodecyl sulfate (SDS) were added as anionic surfactant in some samples. Samples doped with 1%, 5% and 10 % Ce^{3+} ion in the end product were tried to be synthesized. XRD analysis was performed to distinguish the present phases in the samples. XRD data showed that samples were in ZnO phase when no SDS molecules were added during reaction. However with the addition of SDS, samples showed $Zn(OH)_2$ phase. SEM pictures were taken in order to evaluate the morphology of the samples. Samples with SDS had layered morphology after 6 h of reaction. After 24 h of reaction, layers rolled up into a conic morphology. Samples without SDS only showed hexagonal rodlike structure independent from the reaction time. However, with the increasing HMT ratio rods become significantly larger. FTIR analysis was performed to confirm the intercalation of SDS molecules into the layers of $Zn(OH)_2$. Data show the characteristic peaks belongs to the SDS molecules.

Future work

Through the thesis, we have studied synthesis of pure YAG phase with both citrate and reverse strike Co precipitation method at relatively low temperatures. Although the garnet samples were green formed via slip casting and sintered under vacuum at various conditions only 50% transparency was achieved.

One important aspect of slip casting this study does not address is the effect of the dispersant. Therefore several rheology experiments are required to be preformed. Different batches of YAG slips with varying amounts of dispersant will be prepared and their shear viscosity will be measured. In addition, the pure YAG powders from different synthesis methods will green formed into bulk samples and sintered under constant vacuum. As its discussed in the first chapter shrinkage during sintering is an indication of the elimination of porosity therefore density of sintered samples must be measured by the Archimedes method. Although the density alone is not sufficient parameter for transparency, it is a good indicator as denser samples tends to be transparent. Lastly the optical properties must be measured of the transparent samples. Transmittance is vital for evaluation of transparency however; emission and absorption spectroscopy measurements must be performed in order to understand the effects of dopant ions.

At the third chapter of the thesis Cerium doped ZnO and $Zn(OH)_2$ SDS intercalated materials were studied. Synthesis was performed through the hydrothermal method at 90˚C. Also a unique morphology of SDS intercalated $Zn(HO)_2$ was achieved. However the study does not address optical properties and dopant effects to the full detail. Therefore, absorption and emission spectroscopy measurements should be performed. At Electron Microscope pictures of samples without SDS showed that different particles nucleated upon the hexagonal ZnO particles. These nucleated particles were predicted to be Ce_2O_3 however; further chemical and structural analysis is required to evaluate their true composition. Lastly layered structures of $Zn(OH)_2$ samples will exfoliated in order to separate each layer and to obtain individual nano sheets.

BIBLIOGRAPHY

[1] A. Ikesue and Y. L. Aung, "Ceramic laser materials," *Nature Photonics,* vol. 2, pp. 721-727, Dec 2008.

[2] T. H. Maiman, "Simulated optical radiation in ruby," *Nature,* vol. 187, pp. 493-94, 1960.

[3] E. Geusic, Marcos, H. M. & van Uitert, L. G., "Laser oscillation in Nd doped yttrium aluminum,

yttrium gallium and gadolinium garnets," *Appl. Phys. Lett.,* vol. 4, pp. 182–184, 1964.

[4] A. Ikesue and Y. L. Aung, "Synthesis and performance of advanced ceramic lasers," *Journal of the American Ceramic Society,* vol. 89, pp. 1936-1944, Jun 2006.

[5] C. R. Shawley, C. L. Wang, and K. G. Lynn, "Influence of defects in the output power of c- and a-axis growth Nd : YVO4 single laser crystals," *Journal of Applied Physics,* vol. 99, Jun 15 2006.

[6] S. E. Hatch, Parsons, W. F. & Weagley, R. J., "Hot pressed polycrystalline CaF2:Dy2+ laser," *Appl. Phys. Lett. 5,* pp. 153–154, 1964.

[7] H. Yagi, T. Yanagitani, and K. I. Ueda, "Nd3+: Y3Al5O12 laser ceramics: Flashlamp pumped laser operation with a UV cut filter," *Journal of Alloys and Compounds,* vol. 421, pp. 195-199, Sep 14 2006.

[8] R. Apetz and M. P. B. van Bruggen, "Transparent alumina: A light-scattering model," *Journal of the American Ceramic Society,* vol. 86, pp. 480-486, Mar 2003.

[9] W. Zhang, T. C. Lu, N. A. Wei, Y. Z. Wang, B. Y. Ma, F. Li*, et al.*, "Assessment of light scattering by pores in Nd:YAG transparent ceramics," *Journal of Alloys and Compounds,* vol. 520, pp. 36-41, Apr 15 2012.

[10] I. Yamashita and K. Tsukuma, "Light scattering by residual pores in transparent zirconia ceramics," *Journal of the Ceramic Society of Japan,* vol. 119, pp. 133-135, Feb 2011.

[11] R. Boulesteix, A. Maitre, J. F. Baumard, Y. Rabinovitch, and F. Reynaud, "Light scattering by pores in transparent Nd:YAG ceramics for lasers: correlations between microstructure and optical properties," *Optics Express,* vol. 18, pp. 14992-15002, Jul 5 2010.

[12] A. Ikesue and K. Yoshida, "Influence of pore volume on laser performance of Nd : YAG ceramics," *Journal of Materials Science,* vol. 34, pp. 1189-1195, Mar 15 1999.

[13] A. Ikesue and K. Yoshida, "Scattering in polycrystalline Nd : YAG lasers," *Journal of the American Ceramic Society,* vol. 81, pp. 2194-2196, Aug 1998.

[14] P. Zhang, G. R. Qian, Z. P. Xu, H. S. Shi, X. X. Ruan, J. Yang*, et al.*, "Effective adsorption of sodium dodecylsulfate (SDS) by hydrocalumite (CaAl-LDH-Cl) induced by self-dissolution and re-precipitation mechanism," *Journal of Colloid and Interface Science,* vol. 367, pp. 264-271, Feb 1 2012.

[15] A. Ikesue, K. Yoshida, T. Yamamoto, and I. Yamaga, "Optical scattering centers in polycrystalline Nd:YAG laser," *Journal of the American Ceramic Society,* vol. 80, pp. 1517-1522, Jun 1997.

[16] M. Liu, S. W. Wang, D. Y. Tang, L. D. Chen, and J. Ma, "Fabrication and microstructures of YAG transparent ceramics," *Science of Sintering,* vol. 40, pp. 311-317, 2008.

[17] A. P. Patel, M. R. Levy, R. W. Grimes, R. M. Gaume, R. S. Feigelson, K. J. McClellan*, et al.*, "Mechanisms of nonstoichiometry in Y(3)Al(5)O(12)," *Applied Physics Letters,* vol. 93, Nov 10 2008.

[18] Y. N. Xu and W. Y. Ching, "Electronic structure of yttrium aluminum garnet (Y3Al5O12)," *Physical Review B,* vol. 59, pp. 10530-10535, Apr 15 1999.

[19] B. Cockayne, "The Uses and Enigmas of the Al2o3-Y2o3 Phase System," *Journal of the Less-Common Metals,* vol. 114, pp. 199-206, Dec 2 1985.

[20] W. Koechner, *Solid-State Laser Engineering pp. 28-53.* Germany: Springer-Verlag Berlin Heidelberg, 1999.

[21] S. A. P. R. C. Powell, L. L. Chase and G. D. Wilke, "Index-of-Refraction Change in Optically Pumped Solid-State Laser Materials," *Opt. Lett.,* vol. 14 [21], pp. 1204-1206, 1989.

[22] W. F. Krupke, M. D. Shinn, J. E. Marion, J. A. Caird, and S. E. Stokowski, "Spectroscopic, Optical, and Thermomechanical Properties of Neodymium-Doped and Chromium-Doped Gadolinium Scandium Gallium Garnet," *Journal of the Optical Society of America B-Optical Physics,* vol. 3, pp. 102-114, Jan 1986.

[23] A. E. Nielsen, *Kinetics of Precipitation*. New York: MacMillan, 1964.

[24] J. W. Christian, *The Theory of Transformations in Metals and Alloys* Oxford: Pergamon, 1975.

[25] A. G. Walton, "In Nucleation," in *Nucleation in Liquids and Solutions*, A. C. Zettlemoyer, Ed., ed New York: Marcel Dekker, 1969, pp. 225-307.

[26] R. E. Mesmer, Jr., *The Hydrolisis of Cations*. New York: Wiley, 1976

[27] M. N. Rahaman, *Ceramic Processing and Sintering*: Marcel Dekker Inc, 2003.

[28] V. K. D. LaMer, R. H. J., *Am. Chem. Soc.,* vol. 72, p. 4847, 1950.

[29] A. Krell, P. Blank, H. W. Ma, T. Hutzler, M. P. B. van Bruggen, and R. Apetz, "Transparent sintered corundum with high hardness and strength," *Journal of the American Ceramic Society,* vol. 86, pp. 12-18, Jan 2003.

[30] J. G. Li, T. Ikegami, J. H. Lee, T. Mori, and Y. Yajima, "Co-precipitation synthesis and sintering of yttrium aluminum garnet (YAG) powders: the effect of precipitant," *Journal of the European Ceramic Society,* vol. 20, pp. 2395-2405, Dec 2000.

[31] J. G. Li, T. Ikegami, J. H. Lee, T. Mori, and Y. Yajima, "Reactive yttrium aluminate garnet powder via coprecipitation using ammonium hydrogen carbonate as the precipitant," *Journal of Materials Research,* vol. 15, pp. 1864-1867, Sep 2000.

[32] D. J. Sordelet, M. Akinc, M. L. Panchula, Y. Han, and M. H. Han, "Synthesis of Yttrium-Aluminum-Garnet Precursor Powders by Homogeneous Precipitation," *Journal of the European Ceramic Society,* vol. 14, pp. 123-130, 1994.

[33] K. M. Kinsman and J. Mckittrick, "Phase Development and Luminescence in Chromium-Doped Yttrium-Aluminum-Garnet (Yag-Cr) Phosphors," *Journal of the American Ceramic Society,* vol. 77, pp. 2866-2872, Nov 1994.

[34] H. Z. Wang, L. Gao, and K. Niihara, "Synthesis of nanoscaled yttrium aluminum garnet powder by the co-precipitation method," *Materials Science and Engineering a-Structural Materials Properties Microstructure and Processing,* vol. 288, pp. 1-4, Aug 31 2000.

[35] S. M. Sim, K. A. Keller, and T. I. Mah, "Phase formation in yttrium aluminum garnet powders synthesized by chemical methods," *Journal of Materials Science,* vol. 35, pp. 713-717, Feb 2000.

[36] A. Fernandez and J. Somers, "Highly porous yttrium aluminium garnet (YAG) particles synthesised by a gel supported precipitation (GSP) process," *Journal of Materials Science,* vol. 38, pp. 2331-2335, Jun 1 2003.

[37] P. Apte, H. Burke, and H. Pickup, "Synthesis of Yttrium-Aluminum-Garnet by Reverse Strike Precipitation," *Journal of Materials Research,* vol. 7, pp. 706-711, Mar 1992.

[38] J. G. Li, T. Ikegami, J. H. Lee, and T. Mori, "Well-sinterable Y3Al5O12 powder front carbonate precursor," *Journal of Materials Research,* vol. 15, pp. 1514-1523, Jul 2000.

[39] A. Verma, M. Nath, N. Malhan, and A. K. Ganguli, "Improved optical properties in nanocrystalline Ce:YGG garnets via normal and reverse strike co-precipitation method," *Materials Letters,* vol. 93, pp. 21-24, Feb 15 2013.

[40] A. M. George, N. C. Mishra, M. S. Nagar, and N. C. Jayadevan, "Formation of YAG from coprecipitated yttrium aluminium hydroxides," *Journal of Thermal Analysis,* vol. 47, pp. 1701-1708, Dec 1996.

[41] R. J. Bratton, *American Ceramic Society Bulletin,* vol. 48 (8), p. 759, 1959.

[42] V. B. Glushkova, O. N. Egorova, V. A. Krzhizhanovskaya, and K. Y. Merezhinskii, "Synthesis of Yttrium Aluminates by Precipitation of Hydroxides," *Inorganic Materials,* vol. 19, pp. 1015-1018, 1983.

[43] C. C. Chiang, M. S. Tsai, C. S. Hsiao, and M. H. Hon, "Synthesis of YAG : Ce phosphor via different aluminum sources and precipitation processes," *Journal of Alloys and Compounds,* vol. 416, pp. 265-269, Jun 8 2006.

[44] W. J. Dawson, *American Ceramic Society Bulletin,* vol. 67 (10), p. 1673, 1988.

[45] M. N. Rahaman and Y. C. Zhou, "Effect of Solid-Solution Additives on the Sintering of Ultra-Fine Ceo2 Powders," *Journal of the European Ceramic Society,* vol. 15, pp. 939-950, 1995.

[46] J. H. Peterson, "U.S. Patent # 2,216,655," Oct. 22, 1940.

[47] T. Takamori and L. D. David, "Controlled Nucleation for Hydrothermal Growth of Yttrium-Aluminum-Garnet Powders," *American Ceramic Society Bulletin,* vol. 65, pp. 1282-1286, Sep 1986.

[48] A. Ikesue, I. Furusato, and K. Kamata, "Fabrication of Polycrystalline, Transparent Yag Ceramics by a Solid-State Reaction Method," *Journal of the American Ceramic Society,* vol. 78, pp. 225-228, Jan 1995.

[49] S. Kochawattana, "Phase formation and sintering of YAG ceramics," PhD, Material Science and Engineering, The Pennsylvania State University, 2007.

[50] S. H. Lee, S. Kochawattana, G. L. Messing, J. Q. Dumm, G. Quarles, and V. Castillo, "Solid-state reactive sintering of transparent polycrystalline Nd : YAG ceramics," *Journal of the American Ceramic Society,* vol. 89, pp. 1945-1950, Jun 2006.

[51] L. Z. Predoana, M., in *Sol-Gel Process*, R. E. Morris, Ed., ed: Nova Science Publishers, Inc., 2011.

[52] J. Zarzycki, M. Prassas, and J. Phalippou, "Synthesis of Glasses from Gels - the Problem of Monolithic Gels," *Journal of Materials Science,* vol. 17, pp. 3371-3379, 1982.

[53] Y. Huan, X. H. Wang, L. M. Guo, and L. T. Li, "Low Temperature Sintering and Enhanced Piezoelectricity of Lead-Free (Na0.52K0.4425Li0.0375)(Nb0.86Ta0.06Sb0.08)O-3 Ceramics Prepared from Nano-Powders," *Journal of the American Ceramic Society,* vol. 96, pp. 3470-3475, Nov 2013.

[54] C. C. Marcilly, P.; Delmon, B. J., *Am. Ceram. Soc.,* vol. 53, p. 56, 1970.

[55] P. M. P., " U.S. Patent # 3,330,697," 1967.

[56] M. L. Liu and D. S. Wang, "Preparation of La1-Zsrzco1-Yfeyo3-X Thin-Films, Membranes, and Coatings on Dense and Porous Substrates," *Journal of Materials Research,* vol. 10, pp. 3210-3221, Dec 1995.

[57] E. Zych, A. Walasek, L. Kpinski, and J. Legendziewicz, "Low temperature synthesis of YAG : Eu spheroidal monocrystalline submicron-sized particles," *Journal of Luminescence,* vol. 119, pp. 576-580, Jul-Oct 2006.

[58] P. F. S. Pereira, J. M. A. Caiut, S. J. L. Ribeiro, Y. Messaddeq, K. J. Ciuffi, L. A. Rocha*, et al.*, "Microwave synthesis of YAG : Eu by sol-gel methodology," *Journal of Luminescence,* vol. 126, pp. 378-382, Oct 2007.

[59] H. M. H. Fadlalla and C. C. Tang, "YAG:Ce3+ nano-sized particles prepared by precipitation technique," *Materials Chemistry and Physics,* vol. 114, pp. 99-102, Mar 15 2009.

[60] J. Su, Q. L. Zhang, S. F. Shao, W. P. Liu, S. M. Wan, and S. T. Yin, "Phase transition, structure and luminescence of Eu:YAG nanophosphors by co-precipitation method," *Journal of Alloys and Compounds,* vol. 470, pp. 306-310, Feb 20 2009.

[61] Y. H. Zhou, J. Lin, M. Yu, S. M. Han, S. B. Wang, and H. J. Zhang, "Morphology control and luminescence properties of YAG : Eu phosphors prepared by spray pyrolysis," *Materials Research Bulletin,* vol. 38, pp. 1289-1299, Jul 14 2003.

[62] L. Y. H. Yang, G. Zhu, A. Yu, H. Xu,, "Luminescent properties of YAG:Ce3+ phosphor powders prepared by hydrothermal-homogeneous precipitation method," *Mater. Lett. ,* vol. 63, pp. 2271–2273, 2009.

[63] R. V. Kamat, K. T. Pillai, V. N. Vaidya, and D. D. Sood, "Synthesis of yttrium aluminium garnet by the gel entrapment technique using hexamine," *Materials Chemistry and Physics,* vol. 46, pp. 67-71, Oct 1996.

[64] P. Vaqueiro and M. A. Lopez-Quintela, "Synthesis of yttrium aluminium garnet by the citrate gel process," *Journal of Materials Chemistry,* vol. 8, pp. 161-163, Jan 1998.

[65] W. D. Kingery, *Ceramic Fabrication Processes* vol. Part I. Cambridge, MA: The MIT Press.

[66] F. M. Tiller and C. D. Tsai, "Theory of Filtration of Ceramics .1. Slip Casting," *Journal of the American Ceramic Society,* vol. 69, pp. 882-887, Dec 1986.

[67] J. H. D. Hampton, "Experimental and Theoretical Studies of The Filtration of Ceramic Suspensions," Civil Engineering and Applied Mechanics, McGill University, Montreal, Canada.

[68] W.P.Kelley, *Cation Exehange in Soils*. New York: Reinhold Pub. Corp., 1948.

[69] E. J. W. V. a. J.Th.G.Overbeek, *Theory of the Solubility of Lyophobic Colloids*. New York Elsevier Pub. Co., 1948.

[70] G. V. D. De With, H. J. A., "Translucent $Y_3Al_5O_{12}$ Ceramics," *Material Research Bulletin,* vol. 19, pp. 1669-1674, 1984.

[71] J. R. Lu, K. Ueda, H. Yagi, T. Yanagitani, Y. Akiyama, and A. A. Kaminskii, "Neodymium doped yttrium aluminum garnet (Y3Al5O12) nanocrystalline ceramics - a new generation of solid state laser and optical materials," *Journal of Alloys and Compounds,* vol. 341, pp. 220-225, Jul 17 2002.

[72] R. L. Coble, "Transparent Alumina and Method of Preparation, U.S. Patent 3026210," March 20, 1962.

[73] G. J. P. a. R. Metselaar and (). "Light-Scattering by Pores in Polycrystalline Materials—Transmission Properties of Alumina," *J. Appl. Phys.,* pp. 216–20, 1974.

[74] A. J. Stevenson, X. Li, M. A. Martinez, J. M. Anderson, D. L. Suchy, E. R. Kupp*, et al.*, "Effect of SiO2 on Densification and Microstructure Development in Nd:YAG Transparent Ceramics," *Journal of the American Ceramic Society,* vol. 94, pp. 1380-1387, May 2011.

[75] A. Ikesue and K. Kamata, "Role of Si on Nd Solid-Solution of Yag Ceramics," *Journal of the Ceramic Society of Japan,* vol. 103, pp. 489-493, May 1995.

[76] A. Maitre, C. Salle, R. Boulesteix, J. F. Baumard, and Y. Rabinovitch, "Effect of silica on the reactive sintering of polycrystalline Nd : YAG ceramics," *Journal of the American Ceramic Society,* vol. 91, pp. 406-413, Feb 2008.

[77] S. Kochawattana, A. Stevenson, S. H. Lee, M. Ramirez, V. Gopalan, J. Dumm*, et al.*, "Sintering and grain growth in SiO2 doped Nd : YAG," *Journal of the European Ceramic Society,* vol. 28, pp. 1527-1534, 2008.

[78] S. R. Rotman and C. Warde, "Defect Luminescence in Cerium-Doped Yttrium Aluminum Garnet," *Journal of Applied Physics,* vol. 58, pp. 522-525, 1985.

[79] G. B. Blasse, A., "Investigation of Some Ce3+Activated Phosphors," *The Journal of Chemical Physics,* vol. 47, pp. 5139-5145, 1967.

[80] T. Tomiki, H. Akamine, M. Gushiken, Y. Kinjoh, M. Miyazato, T. Miyazato*, et al.*, "Ce3+ Centers in Y3al5o12 (Yag) Single-Crystals," *Journal of the Physical Society of Japan,* vol. 60, pp. 2437-2445, Jul 1991.

[81] E. Carnell, Hatch, S. E., Parson, W. F., *Material Science Research,* vol. 3Plenum, p. 165, 1966.

[82] C. Greskovich, Chernoch, J. P., *Journal of Applied Physics,* vol. 44, p. 4599, 1973.

[83] R. L. Coble, "Sintering crystalline solid II. Experimental test of diffusion models in powder compacts," *Journal of Applied Physics,* pp. 793–799, 1961.

[84] A. Ikesue, T. Kinoshita, K. Kamata, and K. Yoshida, "Fabrication and Optical-Properties of High-Performance Polycrystalline Nd-Yag Ceramics for Solid-State Lasers," *Journal of the American Ceramic Society,* vol. 78, pp. 1033-1040, Apr 1995.

[85] G. A. Kumar, J. R. Lu, A. A. Kaminskii, K. I. Ueda, H. Yagi, T. Yanagitani*, et al.*, "Spectroscopic and stimulated emission characteristics of Nd3+ in transparent YAG ceramics," *Ieee Journal of Quantum Electronics,* vol. 40, pp. 747-758, Jun 2004.

[86] J. R. Lu, T. Murai, K. Takaichi, T. Uematsu, K. Misawa, M. Prabhu*, et al.*, "72 W Nd : Y3Al5O12 ceramic laser," *Applied Physics Letters,* vol. 78, pp. 3586-3588, Jun 4 2001.

[87] Z. H. Sun, D. R. Yuan, H. Q. Li, X. L. Duan, H. Q. Sun, Z. M. Wang*, et al.*, "Synthesis of yttrium aluminum garnet (YAG) by a new sol-gel method," *Journal of Alloys and Compounds,* vol. 379, pp. L1-L3, Oct 6 2004.

[88] C. Marlot, E. Barraud, S. Le Gallet, M. Eichhorn, and F. Bernard, "Synthesis of YAG nanopowder by the co-precipitation method: Influence of pH and study of the reaction mechanisms," *Journal of Solid State Chemistry,* vol. 191, pp. 114-120, Jul 2012.

[89] S. Bhattacharyya and S. Ghatak, "Synthesis and characterization of YAG precursor powder in the hydroxyhydrogel form," *Ceramics International,* vol. 35, pp. 29-34, Jan 2009.

[90] A. M. Wynne, "The Thermal-Decomposition of Urea - an Undergraduate Thermal-Analysis Experiment," *Journal of Chemical Education,* vol. 64, pp. 180-182, Feb 1987.

[91] H. He, R. L. Fu, H. Wang, X. F. Song, Z. W. Pan, X. R. Zhao*, et al.*, "Li(2)SrSiO(4):Eu(2+) phosphor prepared by the Pechini method and its application in white light emitting diode," *Journal of Materials Research,* vol. 23, pp. 3288-3294, Dec 2008.

[92] S. A. Hassanzadeh-Tabrizi, "Synthesis and luminescence properties of YAG:Ce nanopowder prepared by the Pechini method," *Advanced Powder Technology,* vol. 23, pp. 324-327, May 2012.

[93] J. L. Zarate, R. Aguilar, E. A., "Synthesis of Yttrium Aluminum Garnet by Modifying the Citrate Precursor Method," *The AZo Journal of Materials,* 2005.

[94] X. Z. Guo, P. S. Devi, B. G. Ravi, J. B. Parise, S. Sampath, and J. C. Hanson, "Phase evolution of yttrium aluminium garnet (YAG) in a citrate-nitrate gel combustion process," *Journal of Materials Chemistry,* vol. 14, pp. 1288-1292, 2004.

[95] J. Su, Q. L. Zhang, C. J. Gu, D. L. Sun, Z. B. Wang, H. L. Qiu*, et al.*, "Preparation and characterization of Y3Al5O12 (YAG) nano-powder by co-precipitation method," *Materials Research Bulletin,* vol. 40, pp. 1279-1285, Aug 11 2005.

[96] Y. C. Jia, Y. J. Huang, Y. H. Zheng, N. Guo, H. Qiao, Q. Zhao*, et al.*, "Color point tuning of Y3Al5O12:Ce3+ phosphor via Mn2+-Si4+ incorporation for white light generation," *Journal of Materials Chemistry,* vol. 22, pp. 15146-15152, 2012.

[97] D. R. Lide, *Handbook of the Chemistry and Physics*: CRC, Taylor and Francis, 2005.

[98] D. Ravichandran, R. Roy, A. G. Chakhovskoi, C. E. Hunt, W. B. White, and S. Erdei, "Fabrication of Y3Al5O12:Eu thin films and powders for field emission display applications," *Journal of Luminescence,* vol. 71, pp. 291-297, May 1997.

[99] B. Vaidhyanathan and J. G. P. Binner, "Microwave assisted synthesis of nanocrystalline YAG," *Journal of Materials Science,* vol. 41, pp. 5954-5957, Aug 2006.

[100] M. L. Saladino, E. Caponetti, D. C. Martino, S. Enzo, and G. Ibba, "Effect of the dopant selection (Er, Eu, Nd or Ce) and its quantity on the formation of yttrium aluminum garnet nanopowders," *Optical Materials,* vol. 31, pp. 261-267, Oct-Dec 2008.

[101] J. W. G. A. W. Vrolijk, J.W.M.M.; Metselaar, R., "Sol–gel synthesis for preparation of yttrium aluminum garnet," *Euro Ceramics,* vol. 1, pp. 104-108, 1989.

[102] A. L. Costa, L. Esposito, V. Medri, and A. Bellosi, "Synthesis of Nd-YAG material by citrate-nitrate sol-gel combustion route," *Advanced Engineering Materials,* vol. 9, pp. 307-312, Apr 2007.

[103] Y. T. Nien, K. M. Chen, I. G. Chen, and T. Y. Lin, "Photoluminescence Enhancement of Y(3)Al(5)O(12):Ce Nanoparticles Using HMDS," *Journal of the American Ceramic Society,* vol. 91, pp. 3599-3602, Nov 2008.

[104] S. A. Hassanzadeh-Tabrizi, "Low temperature synthesis and luminescence properties of YAG:Eu nanopowders prepared by modified sol-gel method," *Transactions of Nonferrous Metals Society of China,* vol. 21, pp. 2443-2447, Nov 2011.

[105] S. H. Ko, I. Park, H. Pan, N. Misra, M. S. Rogers, C. P. Grigoropoulos*, et al.*, "ZnO nanowire network transistor fabrication on a polymer substrate by low-temperature, all-inorganic nanoparticle solution process," *Applied Physics Letters,* vol. 92, Apr 14 2008.

[106] Y. Khan, S. K. Durrani, M. Mehmood, J. Ahmad, M. R. Khan, and S. Firdous, "Low temperature synthesis of fluorescent ZnO nanoparticles," *Applied Surface Science,* vol. 257, pp. 1756-1761, Dec 15 2010.

[107] Y. F. Zhu and W. Z. Shen, "Synthesis of ZnO compound nanostructures via a chemical route for photovoltaic applications," *Applied Surface Science,* vol. 256, pp. 7472-7477, Oct 1 2010.

[108] L. B. Feng, A. H. Liu, J. Wei, M. Liu, Y. Y. Ma, and B. Y. Man, "Synthesis, characterization and optical properties of multipod ZnO whiskers," *Applied Surface Science,* vol. 255, pp. 8667-8671, Jul 30 2009.

[109] E. Topoglidis, A. E. G. Cass, B. O'Regan, and J. R. Durrant, "Immobilisation and bioelectrochemistry of proteins on nanoporous TiO2 and ZnO films," *Journal of Electroanalytical Chemistry,* vol. 517, pp. 20-27, Dec 28 2001.

[110] S. H. Ko, D. Lee, H. W. Kang, K. H. Nam, J. Y. Yeo, S. J. Hong*, et al.*, "Nanoforest of Hydrothermally Grown Hierarchical ZnO Nanowires for a High Efficiency Dye-Sensitized Solar Cell," *Nano Letters,* vol. 11, pp. 666-671, Feb 2011.

[111] Z. Y. Zhang, X. H. Li, C. H. Wang, L. M. Wei, Y. C. Liu, and C. L. Shao, "ZnO Hollow Nanofibers: Fabrication from Facile Single Capillary Electrospinning and Applications in Gas Sensors," *Journal of Physical Chemistry C,* vol. 113, pp. 19397-19403, Nov 12 2009.

[112] R. Ferro, J. A. Rodriguez, P. Bertrand, M. Henry, and C. Poleunis, "Response enhancement of sprayed ZnO thin film-based NO2 sensor by indium-doping," *Revista Mexicana De Fisica,* vol. 52, pp. 23-25, Feb 2006.

[113] S. H. Seo, W. C. Shin, and J. S. Park, "A novel method of fabricating ZnO/diamond/Si multilayers for surface acoustic wave (SAW) device applications," *Thin Solid Films,* vol. 416, pp. 190-196, Sep 2 2002.

[114] Z. Z. Shao, L. Y. Wen, D. M. Wu, X. A. Zhang, S. L. Chang, and S. Q. Qin, "AFM analysis of piezoelectric nanogenerator based on n(+)-diamond/n-ZnO heterojunction," *Applied Surface Science,* vol. 257, pp. 4919-4922, Mar 15 2011.

[115] C. Y. Zang, C. H. Zang, B. Wang, Z. X. Jia, S. R. Yue, Y. S. Li*, et al.*, "Fabrication and photoluminescence of P doped ZnO nanobelts by thermal evaporation method," *Physica B-Condensed Matter,* vol. 406, pp. 3479-3483, Sep 15 2011.

[116] J. H. Lee, K. Y. Lee, B. Kumar, and S. W. Kim, "Synthesis of Ga-Doped ZnO Nanorods Using an Aqueous Solution Method for a Piezoelectric Nanogenerator," *Journal of Nanoscience and Nanotechnology,* vol. 12, pp. 3430-3433, Apr 2012.

[117] F. Guell, J. O. Osso, A. R. Goni, A. Cornet, and J. R. Morante, "Synthesis and optical spectroscopy of ZnO nanowires," *Superlattices and Microstructures,* vol. 45, pp. 271-276, Apr-May 2009.

[118] J. Y. Lao, J. Y. Huang, D. Z. Wang, and Z. F. Ren, "ZnO nanobridges and nanonails," *Nano Letters,* vol. 3, pp. 235-238, Feb 2003.

[119] P. Li, H. Liu, F. X. Xu, and Y. Wei, "Controllable growth of ZnO nanowhiskers by a simple solution route," *Materials Chemistry and Physics,* vol. 112, pp. 393-397, Dec 1 2008.

[120] M. Nakano, T. Makino, A. Tsukazaki, K. Ueno, A. Ohtomo, T. Fukumura*, et al.*, "Transparent polymer Schottky contact for a high performance visible-blind ultraviolet photodiode based on ZnO," *Applied Physics Letters,* vol. 93, Sep 22 2008.

[121] I. T. Drapak, "Visible luminescence of a ZnO–Cu_2O heterojunction," *Semiconductors,* vol. 2, pp. 624-625, 1968.

[122] A. Tsukazaki, A. Ohtomo, T. Onuma, M. Ohtani, T. Makino, M. Sumiya*, et al.*, "Repeated temperature modulation epitaxy for p-type doping and light-emitting diode based on ZnO," *Nature Materials,* vol. 4, pp. 42-46, Jan 2005.

[123] A. Tsukazaki, M. Kubota, A. Ohtomo, T. Onuma, K. Ohtani, H. Ohno*, et al.*, "Blue light-emitting diode based on ZnO," *Japanese Journal of Applied Physics Part 2-Letters & Express Letters,* vol. 44, pp. L643-L645, 2005.

[124] H. Cao, Y. G. Zhao, S. T. Ho, E. W. Seelig, Q. H. Wang, and R. P. H. Chang, "Random laser action in semiconductor powder," *Physical Review Letters,* vol. 82, pp. 2278-2281, Mar 15 1999.

[125] X. Wu, A. Yamilov, X. Liu, S. Li, V. P. Dravid, R. P. H. Chang*, et al.*, "Ultraviolet photonic crystal laser," *Applied Physics Letters,* vol. 85, pp. 3657-3659, Oct 25 2004.

[126] M. Scharrer, A. Yamilov, X. H. Wu, H. Cao, and R. P. H. Chang, "Ultraviolet lasing in high-order bands of three-dimensional ZnO photonic crystals," *Applied Physics Letters,* vol. 88, May 15 2006.

[127] O. K. Dalrymple, D. H. Yeh, and M. A. Trotz, "Removing pharmaceuticals and endocrine-disrupting compounds from wastewater by photocatalysis," *Journal of Chemical Technology and Biotechnology,* vol. 82, pp. 121-134, Feb 2007.

[128] M. Ladanov, M. K. Ram, G. Matthews, and A. Kumar, "Structure and Opto-electrochemical Properties of ZnO Nanowires Grown on n-Si Substrate," *Langmuir,* vol. 27, pp. 9012-9017, Jul 19 2011.

[129] N. V. Kaneva, D. T. Dimitrov, and C. D. Dushkin, "Effect of nickel doping on the photocatalytic activity of ZnO thin films under UV and visible light," *Applied Surface Science,* vol. 257, pp. 8113-8120, Jul 1 2011.

[130] W. J. E. Beek, M. M. Wienk, and R. A. J. Janssen, "Efficient hybrid solar cells from zinc oxide nanoparticles and a conjugated polymer," *Advanced Materials,* vol. 16, pp. 1009-+, Jun 17 2004.

[131] M. Law, L. E. Greene, J. C. Johnson, R. Saykally, and P. D. Yang, "Nanowire dye-sensitized solar cells," *Nature Materials,* vol. 4, pp. 455-459, Jun 2005.

[132] P. S. Cho, K. W. Kim, and J. H. Lee, "NO2 sensing characteristics of ZnO nanorods prepared by hydrothermal method," *Journal of Electroceramics,* vol. 17, pp. 975-978, Dec 2006.

[133] G. S. Devi, V. B. Subrahmanyam, S. C. Gadkari, and S. K. Gupta, "NH3 gas sensing properties of nanocrystalline ZnO based thick films," *Analytica Chimica Acta,* vol. 568, pp. 41-46, May 24 2006.

[134] H. Gong, J. Q. Hu, J. H. Wang, C. H. Ong, and F. R. Zhu, "Nano-crystalline Cu-doped ZnO thin film gas sensor for CO," *Sensors and Actuators B-Chemical,* vol. 115, pp. 247-251, May 23 2006.

[135] H. T. Wang, B. S. Kang, F. Ren, L. C. Tien, P. W. Sadik, D. P. Norton*, et al.*, "Hydrogen-selective sensing at room temperature with ZnO nanorods," *Applied Physics Letters,* vol. 86, Jun 13 2005.

[136] X. H. Wang, Y. F. Ding, J. Zhang, Z. Q. Zhu, S. Z. You, S. Q. Chen*, et al.*, "Humidity sensitive properties of ZnO nanotetrapods investigated by a quartz crystal microbalance," *Sensors and Actuators B-Chemical,* vol. 115, pp. 421-427, May 23 2006.

[137] S. Christoulakis, M. Suchea, E. Koudoumas, M. Katharakis, N. Katsarakis, and G. Kiriakidis, "Thickness influence on surface morphology and ozone sensing properties of nanostructured ZnO transparent thin films grown by PLD," *Applied Surface Science,* vol. 252, pp. 5351-5354, May 30 2006.

[138] C. H. Wang, X. F. Chu, and M. W. Wu, "Detection of H2S down to ppb levels at room temperature using sensors based on ZnO nanorods," *Sensors and Actuators B-Chemical,* vol. 113, pp. 320-323, Jan 17 2006.

[139] T. F. Xue, J. F. Hu, H. W. Qin, Y. Zhou, K. An, L. Zhang*, et al.*, "Sensing properties of the ZnO based composite oxide (Al,Sb)/ZnO to C2H5OH gas," *Rare Metal Materials and Engineering,* vol. 33, pp. 1006-1008, Sep 2004.

[140] Z. T. Chen and L. Gao, "A facile route to ZnO nanorod arrays using wet chemical method," *Journal of Crystal Growth,* vol. 293, pp. 522-527, Aug 1 2006.

[141] S. Baruah and J. Dutta, "Hydrothermal growth of ZnO nanostructures," *Science and Technology of Advanced Materials,* vol. 10, Mar 2009.

[142] H. H. Choi, "Synthesis and characterization of tailoered zinc oxide nanostructures and their engineered nanocomposites," PhD, University of Florida, 2004.

[143] N. W. Emanetoglu, C. Gorla, Y. Liu, S. Liang, and Y. Lu, "Epitaxial ZnO piezoelectric thin films for saw filters," *Materials Science in Semiconductor Processing,* vol. 2, pp. 247-252, Oct 1999.

[144] Y. F. Chen, D. Bagnall, and T. F. Yao, "ZnO as a novel photonic material for the UV region," *Materials Science and Engineering B-Solid State Materials for Advanced Technology,* vol. 75, pp. 190-198, Jun 1 2000.

[145] A. K. Sood, Y. R. Puri, C. S. Lao, W. J. Mai, P. X. Gao, S. Xu*, et al.*, "A review of growth and characterization of ZnO nanostructures for optical applications - art. no. 676803," *Nanomaterials Synthesis, Interfacing, and Integrating in Devices, Circuits, and Systems Ii,* vol. 6768, pp. 76803-76803, 2007.

[146] T. Kawano and H. Imai, "Fabrication of ZnO nanoparticles with various aspect ratios through acidic and basic routes," *Crystal Growth & Design,* vol. 6, pp. 1054-1056, Apr 2006.

[147] L. Vayssieres, "Growth of arrayed nanorods and nanowires of ZnO from aqueous solutions," *Advanced Materials,* vol. 15, pp. 464-466, Mar 4 2003.

[148] J. Yahiro, T. Kawano, and H. Imai, "Nanometric morphological variation of zinc oxide crystals using organic molecules with carboxy and sulfonic groups," *Journal of Colloid and Interface Science,* vol. 310, pp. 302-311, Jun 1 2007.

[149] L. DiLeo, D. Romano, L. Schaeffer, B. Gersten, C. Foster, and M. C. Gelabert, "Effect of complexing agent on hydrothermal growth of ZnO crystals," *Journal of Crystal Growth,* vol. 271, pp. 65-73, Oct 15 2004.

[150] A. Sugunan, H. C. Warad, M. Boman, and J. Dutta, "Zinc oxide nanowires in chemical bath on seeded substrates: Role of hexamine," *Journal of Sol-Gel Science and Technology,* vol. 39, pp. 49-56, Jul 2006.

[151] J. J. Richardson and F. F. Lange, "Controlling Low Temperature Aqueous Synthesis of ZnO. 1. Thermodynamic Analysis," *Crystal Growth & Design,* vol. 9, pp. 2570-2575, Jun 2009.

[152] W. J. Li, E. W. Shi, W. Z. Zhong, and Z. W. Yin, "Growth mechanism and growth habit of oxide crystals," *Journal of Crystal Growth,* vol. 203, pp. 186-196, May 1999.

[153] A. S. Shaporev, V. K. Ivanov, A. E. Baranchikov, O. S. Polezhaeva, and Y. D. Tret'yakov, "ZnO formation under hydrothermal conditions from zinc hydroxide compounds with various chemical histories," *Russian Journal of Inorganic Chemistry,* vol. 52, pp. 1811-1816, Dec 2007.

[154] H. R. A. Oswald, R., *Preparation and crystal growth of materials with layered structures*. Dordrecht: D. Reidel Publishing Company, 1977.

[155] X. M. Sun, X. Chen, Z. X. Deng, and Y. D. Li, "A CTAB-assisted hydrothermal orientation growth of ZnO nanorods," *Materials Chemistry and Physics,* vol. 78, pp. 99-104, Feb 3 2003.

[156] S. M. Wang, J. Y. Liu, G. L. Cui, B. B. Yao, and M. Z. Zhang, "Novel ZnO parallel ordered arrays with lamellar structure: Fabrication and characterization," *Materials Letters,* vol. 94, pp. 186-188, Mar 1 2013.

[157] E. M. P. Steinmiller and K. S. Choi, "Anodic construction of lamellar structured ZnO films using basic media via interfacial surfactant templating," *Langmuir,* vol. 23, pp. 12710-12715, Dec 4 2007.

[158] Y. Lin, J. Y. Yang, and Y. M. Meng, "Nanostructured ZnO thin films by SDS-assisted electrodeposition for dye-sensitized solar cell applications," *Ceramics International,* vol. 39, pp. 5049-5052, Jul 2013.

[159] T. Pauporte and J. Rathousky, "Growth mechanism and photocatalytic properties for dye degradation of hydrophobic mesoporous ZnO/SDS films prepared by electrodeposition," *Microporous and Mesoporous Materials,* vol. 117, pp. 380-385, Jan 1 2009.

[160] D. Ramimoghadam, M. Z. Bin Hussein, and Y. H. Taufiq-Yap, "The Effect of Sodium Dodecyl Sulfate (SDS) and Cetyltrimethylammonium Bromide (CTAB) on the Properties of ZnO

Synthesized by Hydrothermal Method," *International Journal of Molecular Sciences,* vol. 13, pp. 13275-13293, Oct 2012.

[161] S. B. Kulkarni, U. M. Patil, R. R. Salunkhe, S. S. Joshi, and C. D. Lokhande, "Temperature impact on morphological evolution of ZnO and its consequent effect on physico-chemical properties," *Journal of Alloys and Compounds,* vol. 509, pp. 3486-3492, Feb 24 2011.

[162] G. B. Sun, M. H. Cao, Y. H. Wang, C. W. Hu, Y. C. Liu, L. Ren*, et al.*, "Anionic surfactant-assisted hydrothermal synthesis of high-aspect-ratio ZnO nanowires and their photoluminescence property," *Materials Letters,* vol. 60, pp. 2777-2782, Sep 2006.

[163] M. Zhao, D. P. Wu, J. L. Chang, Z. Y. Bai, and K. Jiang, "Synthesis of cup-like ZnO microcrystals via a CTAB-assisted hydrothermal route," *Materials Chemistry and Physics,* vol. 117, pp. 422-424, Oct 15 2009.

[164] Y. J. Feng, M. Zhang, M. Guo, and X. D. Wang, "Studies on the PEG-Assisted Hydrothermal Synthesis and Growth Mechanism of ZnO Microrod and Mesoporous Microsphere Arrays on the Substrate," *Crystal Growth & Design,* vol. 10, pp. 1500-1507, Apr 2010.

[165] Z. H. Lim, Z. X. Chia, M. Kevin, A. S. W. Wong, and G. W. Ho, "A facile approach towards ZnO nanorods conductive textile for room temperature multifunctional sensors," *Sensors and Actuators B-Chemical,* vol. 151, pp. 121-126, Nov 26 2010.

[166] M. Kevin, Y. H. Fou, A. S. W. Wong, and G. W. Ho, "A novel maskless approach towards aligned, density modulated and multi-junction ZnO nanowires for enhanced surface area and light trapping solar cells," *Nanotechnology,* vol. 21, Aug 6 2010.

[167] H. C. Greenwell, L. A. Bindley, P. R. Unwin, P. J. Holliman, W. Jones, P. V. Coveney*, et al.*, "In situ monitoring of crystal growth and dissolution of oriented layered double-hydroxide crystals immobilized on silicon," *Journal of Crystal Growth,* vol. 294, pp. 53-59, Aug 15 2006.

[168] H. Zhang, H. B. Li, Y. Guo, G. D. Li, C. Fan, K. J. Wang*, et al.*, "Mild hydrothermal preparation of a layered metal hydroxide salt with microtube/rod morphology," *Particuology,* vol. 8, pp. 192-197, Jun 2010.

[169] J. W. Lee, W. C. Choi, and J. D. Kim, "Size-controlled layered zinc hydroxide intercalated with dodecyl sulfate: effect of alcohol type on dodecyl sulfate template," *Crystengcomm,* vol. 12, pp. 3249-3254, 2010.

[170] K. S. Choi, H. C. Lichtenegger, G. D. Stucky, and E. W. McFarland, "Electrochemical synthesis of nanostructured ZnO films utilizing self-assembly of surfactant molecules at solid-liquid interfaces," *Journal of the American Chemical Society,* vol. 124, pp. 12402-12403, Oct 23 2002.

[171] Y. W. Tan, E. M. P. Steinmiller, and K. S. Choi, "Electrochemical tailoring of lamellar-structured ZnO films by interfacial surfactant templating," *Langmuir,* vol. 21, pp. 9618-9624, Oct 11 2005.

[172] P. C. Tsai and T. H. Fang, "A molecular dynamics study of the nucleation, thermal stability and nanomechanics of carbon nanocones," *Nanotechnology,* vol. 18, Mar 14 2007.

[173] C. H. Liang, Y. Shimizu, M. Masuda, T. Sasaki, and N. Koshizaki, "Preparation of layered zinc hydroxide/surfactant nanocomposite by pulsed-laser ablation in a liquid medium," *Chemistry of Materials,* vol. 16, pp. 963-965, Mar 23 2004.

[174] Y. Sun, D. J. Riley, and M. N. R. Ashfold, "Mechanism of ZnO nanotube growth by hydrothermal methods on ZnO film-coated Si substrates," *Journal of Physical Chemistry B,* vol. 110, pp. 15186-15192, Aug 10 2006.

[175] Y. Chang, "ZnO Nanocones and Nanoplatelets: Synthesis and Characterization," Masters of Science, School of Materials Science and Engineering, Georgia Institute of Technology, 2010.

[176] L. Sun, R. Shao, Z. D. Chen, L. Q. Tang, Y. Dai, and J. F. Ding, "Alkali-dependent synthesis of flower-like ZnO structures with enhanced photocatalytic activity via a facile hydrothermal method," *Applied Surface Science,* vol. 258, pp. 5455-5461, May 1 2012.

[177] H. M. Hu, C. H. Deng, and X. H. Huang, "Hydrothermal growth of center-hollow multigonal star-shaped ZnO architectures assembled by hexagonal conic nanotubes," *Materials Chemistry and Physics,* vol. 121, pp. 364-369, May 15 2010.

[178] L. Wang, Z. H. Dong, Z. G. Wang, F. X. Zhang, and J. Jin, "Layered -Co(OH)2 Nanocones as Electrode Materials for Pseudocapacitors: Understanding the Effect of Interlayer Space on Electrochemical Activity," *Advanced Functional Materials,* vol. 23, pp. 2758-2764, Jun 6 2013.

[179] A. I. Inamdar, A. C. Sonavane, S. K. Sharma, H. Im, and P. S. Patil, "Nanocrystalline zinc oxide thin films by novel double pulse single step electrodeposition," *Journal of Alloys and Compounds,* vol. 495, pp. 76-81, Apr 9 2010.

[180] M. Taibi, S. Ammar, N. Jouini, F. Fievet, P. Molinie, and M. Drillon, "Layered nickel hydroxide salts: synthesis, characterization and magnetic behaviour in relation to the basal spacing," *Journal of Materials Chemistry,* vol. 12, pp. 3238-3244, 2002.

Vita

Refik Ergün was born in Üsküdar, İstanbul in 1987. Refik received his bachelor’s degree in Materials Science and Engineering from Gebze Institute of Technology in 2010. Then he started his graduate studies at Materials Science and Engineering program at Koç University in 2011. He worked in a project on the development of Yttrium Aluminum Garnet (YAG) transparent ceramics supervised by Professor Uğur Ünal.